Morphological instabilities in drying colloids

DISSERTATION ZUR ERLANGUNG DES

MATHEMATISCH-NATURWISSENSCHAFTLICHEN

DOKTORGRADES

"DOCTOR RERUM NATURALIUM"

IM PROMOTIONSPROGRAMM PROPHYS DER

GEORG-AUGUST UNIVERSITY SCHOOL OF SCIENCE

(GAUSS)

VORGELEGT VON:

Pree-cha Kiatkirakajorn

aus Yala, Thailand

Göttingen, 2018

Betreuungsausschuss

Prof. Dr. Stephan Herminghaus, *Department of Dynamics of Complex Fluids, Max Planck Institute for Dynamics and Self-Organization*

Prof. Dr. Marcus Müller, *Institut für Theoretische Physik, Gerorg-August-Universität*

Dr. habil. Lucas Goehring, *department of Dynamics of Complex Fluids, Max Planck Institute for Dynamics and Self-Organization*

Mitglieder der Prüfungskommission

Dr. habil. Lucas Goehring, *Department of Dynamics of Complex Fluids, Max Planck Institute for Dynamics and Self-Organization*

Prof. Dr. Marcus Müller, *Institut für Theoretische Physik, Gerorg-August-Universität*

Weitere Mitglieder der Prüfungskommission

Prof. Dr. Stephan Herminghaus, *Department of Dynamics of Complex Fluids, Max Planck Institute for Dynamics and Self-Organization*

Prof. Dr. Annette Zippelius, *Institut für Theoretische Physik, Georg-August-Universität*

Prof. Dr. Cynthia Volkert, *Institut für Materialphysik, Georg-August-Universität*

Prof. Dr. Peter Sollich, *Institut für Theoretische Physik, Georg-August-Universität*

Tag der mündlichen Prüfung: 10 September 2018

Contents

Chapter 1

Introduction

Charged colloidal dispersions are commonly used in commercial products, industry and physical sciences. For example, such dispersions are used in paints, inks, film coatings, and as model systems of charged-colloidal dispersions. The use of colloidal particles has been popular for decades, since they can imitate phase behaviours of simple atomic liquids and solids in colloidal fluids at the significant short-range correlations between neighbouring particles. And they also are applied to predict phase behaviours of hard-sphere colloidal crystals, which has been intensively studied, at long-range spatial orders [1].

The crystallization of colloids is also one of the popular topics that such a model system (or a dynamic model) allow to be investigated. Both numerical and experimental studies provide insight into the mechanisms of structural phase transitions and interparticle forces in order to answer a simple question what is the favourite structure for colloidal particles that are dispersed in liquid, but only in the case of monodisperse spherical particles that have been satisfied answered [1–5]. For monodisperse colloidal particles (or hard sphere) of PMMA, it was found, both experimentally and computationally, that as the volume fraction of particles increases, the populations in the colloidal particle can evolve from a simple liquid phase, to liquid and crystal phases in coexistence [1]. Under this condition, one could find two types of structures: close-packed and body-center-cubic crystals, which depending on the range of interparticle forces [5–7].

For polydisperse colloidal particle crystallization is more difficult, which will be discussed here in two examples. The first is in case of hard spheres interactions,

a molecular dynamics (MD) simulation predicts that as the polydispersity (the size distribution) exceeds a critical value (6 to 12%), the crystallization of hard spherical colloids is suppressed [4, 8–10]. Even an increasing in size polydispersity of 1% is enough to cause a change in the crystallization kinetics: for example by delaying or enhancing nucleation times by ten-times in hard sphere colloids [10]. A prediction of the equilibrium phases of polydisperse hard spheres also shows the effect of size polydispersity can stabilize multiple phases, when the size polydispersity is increased [11, 12]. These ranges of the equilibrium phases prediction are various from fluid to fluid-solid or fluid-solid-solid or solid-solid-solid-solid phases [11, 12]. This prediction is supported by a observations of the crystallization of binary hard sphere mixtures at various sizes that shows new two stable phases of colloidal crystals (AB_2 and AB_{13}) can exist [13]. Second, in the case of dilute dispersions of a charged colloidal spheres in deionized solution shows that under the long-range interactions allow charged particles to be more tolerant of the size polydispersity resulting in a crystal state that can be maintained at low volume fractions [14]. Even there is a charging in size polydispersities that crystal phases still exist [14].

From both of these two limits (long-range interactions and polydispersity), there is a considerable gap in the phase space where could be studied whether homogeneous or fractionated crystallizations exist. Recently, a carefully prepared experiment in a real space of the intermediate-range interaction of charged polydisperse colloidal silica, with a broad monomodal size distribution, has shown that despite a polydispersity of 14%, which would be a considerable high polydispersity for the crystallization of hard spheres, the fractional crystallization can appear in charged polydisperse colloidal population. As volume fractions are increased, they can crystallize with multiple phases in coexistence (fluids, bcc, and AB_2 crystal structures). This shows their charming property to build a complex structure from polydisperse colloids with the intermediate range of interparticle forces[15]. This experimental result is supported by numerical simulation, the Gibbs ensemble Monte-Carlo method, on this fractional crystallization in monomodal size distribution. The simulation shows that it is the most popular particles (radius close to the mean) that gather to build the first crystal, and that the residual population then resembles the binary mixture and crystallise as such [16]

From hard spheres to charged polydisperse colloids, however, there are other interesting points that could be investigated for charged polydisperse colloids such as how changing of interaction forces (ion concentration in solvent, particle size and polydispersity) impacts crystallizations, or how and when the crystallization takes place in the real space and what the preferred phase, or phases, are. Therefore, in the first part of this thesis, I present small angle x-ray experiments on aqueous colloidal dispersions based on the work in reference [15]. I have expanded the scope of the study by searching for another more massive or more complex crystal structures to build a phase diagram. Moreover, I present the observations of the crystal nucleation of various colloidal dispersions (different sizes and polydispersities) in the real-time which can exhibit the order of a fractional crystallization and the preferred structures.

The effects of the electrostatic interactions of charged colloidal dispersions does not play a role only in the microscopic aspect, but in macroscopic mechanical instabilities as the colloidal dispersions transform from liquid phase to the solid phase [17, 18]. The interesting application of this is that these colloidal dispersions are widely used as an essential ingredient in industrial process such as catalysis, metallurgy, electronics, glass, ceramics manufacturing, paper and pulp technology, inks, paints, optics, elastomers, food and health care [19]. However, when they dry, these dispersions can show an intriguing variety of patterning mechanisms [17, 18, 20–24]. Consider a drying droplet of a colloidal dispersion, and the evaporations take place near its boundaries. This loss of water from the evaporation causes a flow which drags particles towards the solidification front. At the solidification front, a further compression of dispersed particles is caused in the drying film by the drag forces. This compression causes the deformation of the dried film as the strain releases [20–22, 25].

In chapter 4, I will give some examples of instabilities that can arise, alone or coincident, in drying colloidal suspensions. Shear failure is coincident with stress, which occurs when attractive capillary forces overcome electrostatic forces between particles, in the liquid-solid transition [20, 21]. Cracks are also the response to stresses that appear in the film when the stresses exceed the strength of materials. The crack pattern can be manipulated by changing a sample thicknesses, the surface of a substrate, particles size, or evaporation rates [26, 27], to give the final crack pattern as a collections of spirals [26], waves [28], or straight and parallel line [29, 30]. Moreover,

the evaporation can control the dried shape of a colloidal film in various pattern from a coffee-ring [31] to textured surfaces [32, 33].

To understand the physics behind this instabilities, one should begin with a mass and momentum balance for all phases to describe the compression of dispersed colloidal particles [22, 34–37]. The important idea of this system is Kynch's theory of sedimentation which explain the evolution of mixture with liquid-like properties [34] and Biot's theory of poroelasticity which describes flows and deformations in a mixture with solid-like properties [35]. Recently, many general models have been developed in order to smoothly connect between these two behaviours [36–38]. These models focus on mean fields, or continuum, approximations of the behaviours of a large amount of small interacting colloidal particles [22]. Moreover, many observations have shown additional effects with more complexity that go beyond what the model can predict. Examples of such additional effects, as mentioned above, include the formation of crystals with fractionation and multiple-phases in coexistence [15], or crystallization with rate-dependent structures [10]; flow pattern is influenced by crystalline domains with grain boundaries [39]; plasticity during fracture [40]; structural anisotropy and birefringence [41]; shear banding [20, 21]. These effects take place at the liquid to solid transition (or drying front). Therefore, it is necessary to understand what is happening in this region during the drying process.

The second part of the thesis, a model, based on a mass and momentum balance and the PoissonBoltzmann cell model, is presented to predict the osmotic compression of a colloidal dispersion system and demonstrate the anisotropy in the liquid-solid transition during the drying of colloidal dispersions. I also studied two instabilities, shear banding and guiding cracks, which are influenced by the compression and the anisotropy in the transition.

In this thesis, I report two types of experiments dealing with the crystallization of charged polydisperse colloids, and instabilities of directional drying colloids. In the first chapter, I give an idea of interactions in colloids and what have been studied on colloidal dispersions in both microscopic and macroscopic aspects. In chapter 2, It starts with the general theories which describe interparticle forces in between colloidal particles. I explain the osmotic stress method that is used to prepare hundreds of colloidal systems with a broad range of volume fractions, different size, polydispersity

and ionic strength. In chapter 3, small-angle x-ray scattering experiments is reported, which observe phase behaviours of colloidal systems, a phase diagram for each of three types of the colloidal dispersion. In chapter 4, I present experimental results of the directional drying of colloidal dispersions. Finally, I summarize the thesis and discussed the future direction of this work in chapter 5.

Chapter 2

Experimental setup and Methods

In this chapter, it begins with fundamental theories: the DLVO theory and Poisson-Boltzmann cell model to giving an idea how we describe a single colloidal particle and the interaction between colloids. Moreover, the experimental setup and the treatments of data analysis used in this thesis are described. The first section introduces the material and the osmotic stress method which is used to equilibrate given samples at different volume fractions. The second section presents the equation of state (EOS) of Polyethylene glycol (PEG) [42] and EOS of charge-stabilized colloids [22]. If a colloidal system reaches the equilibrium, the calculated value of osmotic pressure from both EOS has to be in the same order or equal. This is how we ensure that which sample good or bad is. The last section in the chapter, I present essential factors that we extract from SAXS experiments also how we index a crystal structure for the SAXS scattering pattern.

2.1 Interactions in colloids

2.1.1 The DLVO theory

The DLVO theory of colloidal stability plays an important role in colloid science. The theory is base on assumptions that colloids are spherical and charge stabilized, therefore they are able to repel from each other. As the colloidal particles disperse in an electrolyte solution, an electric double layer is formed around the surface of colloid causing the repulsive force. On the other hand, the attractive van der Waals force arises due to the colloidal particle core [43]. Both interactions are the core of
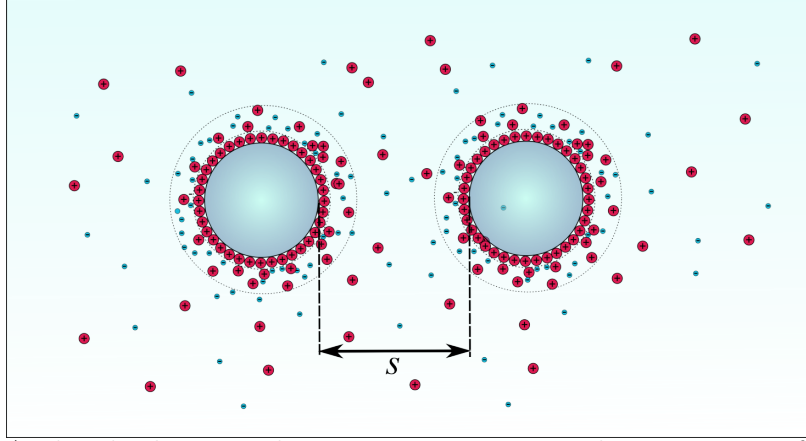
Figure 2.1: A sketch showing the ion concentration, the structure of double layer around a colloidal charged particle with a separation distance S.

the DLVO theory and affect independently on DLVO potential. The forces can be written as the linear combination of forces in colloidal particles between the van der Waals (attractive) and electrical double layer force (repulsive)[43]:

$$F(s) = -\frac{A_H a}{12 s^2} + 32 \pi \varepsilon \varepsilon_0 a \kappa \left(\frac{kT}{e} \right)^2 \tanh^2 \left(\frac{e\psi}{4kT} \right) e^{-\kappa s}, \tag{2.1}$$

or as the potential

$$U(s) = -\frac{A_H a}{12 s} - 32 \pi \varepsilon \varepsilon_0 a \left(\frac{kT}{e} \right)^2 \tanh^2 \left(\frac{e\psi}{4kT} \right) e^{-\kappa s}, \tag{2.2}$$

where the first term is the Van der Waals force; A_H is effective Hamaker constant, a is the radius of particle, s is the distance from the particle's surface, ψ is the electrostatic potential field, e is the fundamental charge, ε_0 is the permittivity of free space, ε is the dielectric constant of the fluid, kT is the thermal energy, and κ^{-1} is the Debye length. The electrostatic force is derived by evaluating the effective pair-potential between neighboring particles and solving the Poisson-Boltzmann equation.

The Poisson-Boltzmann equation[6]:

$$\varepsilon \varepsilon_0 \nabla^2 \psi = -e \sum_i z_i n_{i0} e^{-e z_i \psi / kT}, \tag{2.3}$$

and the Debye length as

$$\kappa^{-1} = \sqrt{\frac{\varepsilon kT}{\sum_i (z_i e)^2 n_{i0}}}, \tag{2.4}$$

where z_i is the relative charge of chemical species i with some background number

density n_{i0} (defined by the electrolyte concentration when $\psi = 0$)[22].

2.1.2 The Poisson-Boltzmann Cell model

Since the interactions in colloids comprise of two forces, the Van der Waals force is a short interaction. Meanwhile, the electrostatic repulsive force has played the important role to create an effective potential barrier providing a mechanism of the stability in colloids: colloidal particles will organize in the way that to keep themselves as far as possible from repulsions. At the thermodynamically equilibrium, one can now partition the total solution into cells, each cell containing one charged-particle, radius of a, amount of counter-ions to make the cell neutral, and salt molecules as well[44]. As a result of the assumed homogeneous distribution of particles, each cell has essentially the same volume (radius of $R > a$), equals the total volume divided by the number of particles. Self-organized behaviors of cells make them being neutral by construction, so there is no strong electrostatic interaction between particles. Hence, colloidal particles are a sphere and exist in the center of the spherical cell. This is an advantage for the numerical work that the model can be considered as a one-dimensional problem.
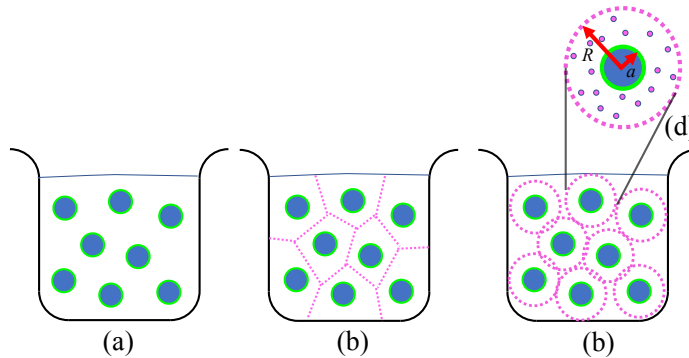
Figure 2.2: A graphic describing the approximation of the cell model. A dispersions of colloids (radius of a) (a) is divided into cells (b) which are comfortably reshaped as symmetric spheres(c). Accordingly, the system is scoped to one cell (radius of R) which the counter-ions distribute around the core of the cell (d).

2.2 Osmotic stress method

The preparation of aqueous dispersions of colloidal silica, the osmotic stress method was used to set the osmotic pressure no samples, as described in ref.[45–48]. Aque-

ous dispersions of colloidal silica (Sigma-Aldrich: Ludox SM30, TM50, HS30 and HS40; AkzoNobel: Levasil30 and Levasil50) were used as received from suppliers as summarized in table 2.1.

First, all types of colloidal dispersions were filtered to 0.8 μm (*Surfactant-free Cellulose Acetate (SFCA)* Syringe Filters, Sartorius™) and cleaned for 2 day by dialysis against aqueous solution of NaCl (concentration between 0.5 and 50 mM), and NaOH (0.1mM for controlling pH at 10) in a dialysis bags with molecular weight cutoffs 14000 g/mole (Spectra/Por4 from Spectrum Laboratories, Inc). Each bag was filled with approximately 10-15 mL of aqueous dispersions of colloidal silica and was carefully inspected during the washing, in case the bag has expanded due to the osmotic pressure inside the bag. If so some aqueous dispersion was immediately removed to reduce pressure inside the bag. The washed silica dispersions were concentrated in a bath by dialysis against aqueous solutions of PEG35000 (Poly(ethylene glycol), Sigma Aldrich)(concentration of 0.5 to 10% (w/w) for 6 days with changing the aqueous solutions in a reservoir every 2 days. At early beginning, the osmotic stress compression to the system of colloidal silica was very fast and is expected to have reached the equilibrium several days later [45, 46]. At a high concentration of PEG (high osmotic pressure), however, the system does not always reach the equilibrium, and some samples form heterogeneous mixtures since the aqueous colloidal silica becomes rigid at the membrane's inner wall [45]. However, these sample could still used for SAXS experiments.

To determine volume fraction of a sample, drops (approximately 1 mL) of dialysed aqueous dispersions were taken out of a container, measured weight mass as wet (or total) mass m_{wet} and dried overnight in an oven at 120 °C. After dispersions dried completely, the solid of dispersions was measured as a dry mass m_{dry}, during the measurement we assume that there is no changing in the density of dried silica (no humidity exchange between a dried sample and the air) [49]. The volume fraction ϕ of a dialysed dispersions is calculated by the equation 2.5:

$$\phi = \frac{\dfrac{m_{dry}}{\rho_{\text{SiO}_2}}}{\dfrac{m_{dry}}{\rho_{\text{SiO}_2}} + \dfrac{m_{wet} - m_{dry}}{\rho_{\text{H}_2\text{O}}}}, \tag{2.5}$$

grade	particle radius (nm)	size polydispersity	supplier
TM50	13.3	11%	Sigma-Aldrich
HS30	7.5	14%	Sigma-Aldrich
HS40	7.9	15%	Sigma-Aldrich
SM30	4.8	19%	Sigma-Aldrich
Levasil30	48	11%	AkzoNobel
Levasil50	49	36%	AkzoNobel

Table 2.1: Colloidal silica that were used in the experiments.

where $\rho_{\mathrm{SiO_2}}$ is the density of silica 2.200 ± 0.050 g/cm^3 [15, 19, 22, 48, 50] and $\rho_{\mathrm{H_2O}}$ is that for water, 1.0 g/cm^3.

2.3 Osmotic pressure of an equilibrated sample

We consider a good dialyzed sample of colloidal dispersions at the equilibrium, the osmotic pressure that arises in a system should have the same value across the system. In other words, the osmotic pressure of the colloidal dispersions (inside the dialysis membrane) and that of the reservoir (PEG) are equal. Thus, we can easily examine whether a sample reaches its equilibrium or not by measuring osmotic pressures from the equation of state (EOS) of PEG and the EOS of colloidal dispersions of a sample.

2.3.1 The equation of state of PEG

In order to convert the osmotic compression data into a usable form, I used the equation of state (EOS) of osmotic pressure for polymer, especially for PEG, which was investigated intensively by Cohen et al.[42]. Briefly, they combined the Van't Hoff equation which describes the osmotic pressure (Π_{vH}) [51] of a diluted solution of polymers (low-concentration of PEG) and the des Cloizeaux (Π_{dCl}) [52] equation which describes a polymer osmotic pressure (higher-concentration of PEG) in the semidilute regimes.

The Van't Hoff equation:

$$\Pi_{vH} = RTc = RT \left(\frac{C}{M_p} \right) = \frac{RT}{M_m} \left(\frac{C}{N} \right), \tag{2.6}$$

where R is the universal gas constant, T is the temperature, c is the polymer molar concentration, C is the polymer mass concentration, M_p is the polymer molecular

weight, M_m is the monomer molecular weight, N is the number of monomer in a polymer chain.

The des Cloizeaux equation:

$$\Pi_{dCl} = \alpha \Pi_{vH} \left(\frac{C}{C^*} \right)^{5/4} = \alpha \frac{RT}{M_m} \left(\frac{C}{N} \right) \left(\frac{C}{C^*} \right)^{5/4}, \qquad (2.7)$$

where the parameter α is determined by an empirical fit to the experimental data of PEG in ref.[42], and C^* is a characteristic polymer concentration associated with the crossover between the dilute and semidilute regimes. C^*, normally, is calculated as a semiquantitatively defined polymer concentration $C^* \sim N^{-4/5}/\overline{V}$, where $\overline{V}$ is the polymer partial specific volume [42]. Through the dilute to the semi dilute regimes, the osmotic pressure is described as $\Pi = (\Pi_{vH} \rightarrow \Pi_{dCl})$, where the right arrow ($\rightarrow$) expresses the dilute - semi dilute transformation. One can introduce an osmotic pressure equation in both regimes as using Equation (2.6) and Equation (2.7) in a form:

$$\Pi N^{9/5} = \frac{RT}{M_m \overline{V}} \left[\left(\frac{C}{C^*} \right) \rightarrow \alpha \left(\frac{C}{C^*} \right)^{9/4} \right]. \qquad (2.8)$$

Equation (2.8) shows that the equation of state is constructed by two parts which $C/C^* < 1$ is leading in $\Pi = \Pi_{vH}$ and $C/C^* > 1$ for $\Pi = \Pi_{cCl}$ regime. At this transition Cohen et al.[42], they tested a linear combination Equation (2.6) and Equation (2.7) by replacing C^* with the precisely defined C_n^*, replacing "$\rightarrow$" with "+", and use α as a single fitting parameter. Then, one can fit for polymer/solvent system by the one-parameter non-virial interpolation function:

$$\Pi N^{9/5} = \frac{RT}{M_m \overline{V}} \left[\left(\frac{C}{C_n^*} \right) + \alpha \left(\frac{C}{C_n^*} \right)^{9/4} \right]. \qquad (2.9)$$

Figure 2.3 presents the fitting of equation 2.9 for PEG in water and PAMS in toluene as reported by Cohen et al. According to their fitting [42], parameters that will be used to calculate the osmotic pressure of PEG solution are $\alpha = 0.49 \pm 0.01$, $\overline{V} = 0.825$ mL/g, and $M_m = 44$ g/mol. These parameters were confirmed by experimental means as reported by Li et al.[46](see Fig.2.4) that the equation 2.9 gives a good agreement of PEG20000 and a fairly good estimation of the osmotic pressures for PEG35000 in the range 0.5-20% (w/w), which corresponds to the range 0.5-10% (w/w) of PEG35000 that was used in our experiments.
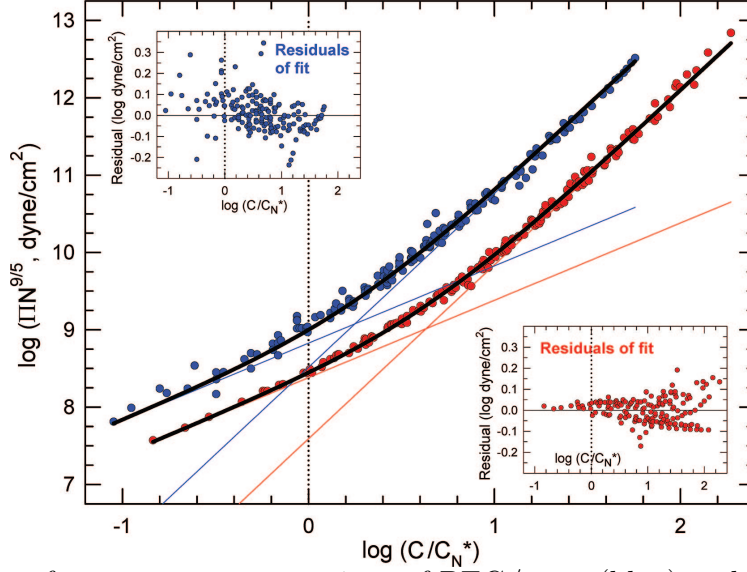
Figure 2.3: Fits of crossover concentrations of PEG/water(blue) and PAMS/toluene. Straight lines are vant Hoff and des Cloizeaux components of the fits. Heavy black lines are logarithmic fits for eq.2.9: fitted values of α are $\alpha_{PEG} = 0.49 \pm 0.01$ ($r^2 = 0.9926$) and $\alpha_{PAMS} = 0.162 \pm 0.002$ ($r^2 = 0.9972$). Panels show residuals are small with no systematic deviations. (Reproduced from [42])

.
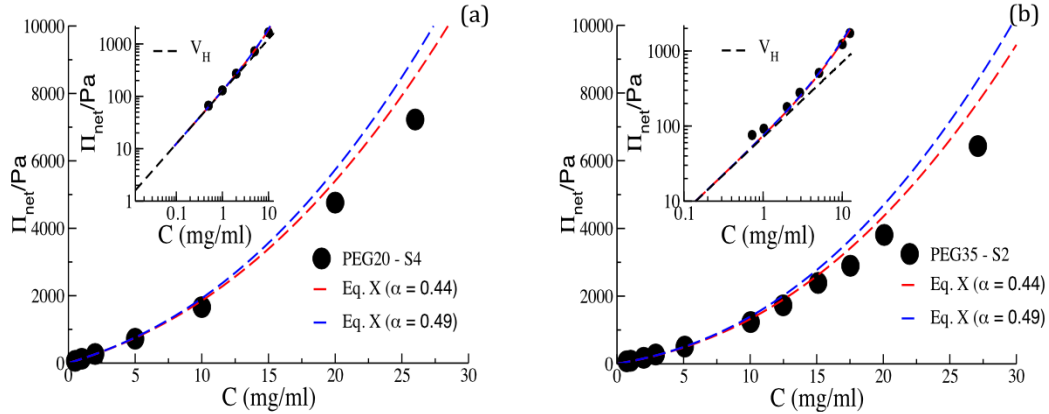
Figure 2.4: The total osmotic pressure in Pascal as a function of concentration in mg/ml for experimentally obtained pressure (black dot) and predicted pressure from EOS by Cohen et al. using $\alpha = 0.44$ (red dash line) and 0.49 (blue dash line) for (a) PEG20000 and (b) PEG35000, respectively. The insert panel shows a magnification of the lower concentration regime, where the black dash line corresponds to the ideal pressure. (Reproduced from [46])

2.3.2 The equation of state of charge-stabilized colloids

To approximate an equation of state (EOS) of the osmotic pressure of charged dispersions (Π_c), the osmotic pressure can be considered as contributions from the hard sphere interactions of particles (Π_q), and from the electrostatic interactions due to the clouds of ions around particles (Π_s). The EOS of the osmotic pressure of charge-

stabilized colloids is given by

$$\Pi_c = \Pi_q + \Pi_s = nkT(Z_q + Z_s).$$ (2.10)

The EOS of the entropic term is well estimated by the Carnahan-Starling equation[53],

$$\Pi_s = nkT\left(\frac{1 + \phi + \phi^2 - \phi^3}{(1 + \phi^3)}\right) = nkTZ_s(\phi)$$ (2.11)

where $Z_s(\phi)$ is the compressibility factor, n is the number density of particles and ϕ is the volume fraction up to 0.55[22, 37]. On the other hand, the electrostatic term can be evaluated by using the Poisson-Boltzmann cell (PBC) model (radius R) of a particle (radius a) dialyzed against a monovalent salt solutions (concentration of n_0): with the cell, the distributions of positive ions and negative ions are giving by $n_{\pm} = n_0 e^{\mp\varphi}$, surface charge density of particle σ. One then can simplify the equation 2.3 to

$$\nabla^2\varphi = \kappa^2 \sinh\varphi, \quad \text{for } a < r < R,$$ (2.12)

with a boundary condition:

$$\frac{\partial\varphi}{\partial r} = -4\pi L_B\sigma, \qquad\qquad \text{at } r = 0,$$
$$\frac{\partial\varphi}{\partial r} = 0, \qquad\qquad \text{at } r = R,$$

where

$$\varphi = \frac{e\psi}{kT},$$ (2.13)

is the reduce electrostatic potential, L_B is the Bjerrum length (0.7 nm in water at room temperature) and the Debye length is defined as

$$\kappa^2 = \frac{2e^2 n_0}{\varepsilon\varepsilon_0 kT}.$$ (2.14)

At the equilibrium, the osmotic pressure of dispersions can be determined by considering the osmotic pressure in the cell. This pressure must be constant throughout the cell: from the surface of the particle ($r = a$) to the surface of the cell ($r = R$). The osmotic pressure is then approximated as the difference between the chemical potential of the ions in the cell and the ions at concentration n_0 of the reservoir[22,

54, 55]:

$$\frac{\Pi_q}{kT} = (n_+(R) - n0) + (n_-(R) - n0) = n_0 \left(e^{-\varphi(R)} + e^{\varphi(R)} - 2 \right). \qquad (2.15)$$

The PBC model will be used to simulate the osmotic pressure of the dispersions in various conditions. We calculated the PBC model in Matlab. The osmotic pressure obtaining from this model will be compared with the osmotic pressure of PEG to check that a dialyzed sample has reached the equilibrium or not.

2.4   Small Angle X-ray Scattering (SAXS)

In this part, I introduce the small angle X-ray scattering (SAXS) technique, which is a powerful structural characterizing technique and has been widely used in various fields of study. This technique is able to explore materials in real time and shows a result as scattering patterns. These scattering patterns are treated and analyzed giving in return, for example, a series of peak ratios of a crystal and properties of a liquid phase. Here, I focus on using small angle X-ray scattering to investigate a given system of colloidal dispersions at different osmotic pressures. I provide a foundation of X-ray scattering, defining the form factor, and the scattering factor, as well as the treatments that are used to determine particle sizes, polydispersity (particle size distribution), and packing of particles.

2.4.1   Scattering theory

We consider an electromagnetic wave (photon) which is plane-polarized propagating in a direction $\boldsymbol{k}$ towards a material. When the X-ray photon hits the material, it may be scattered by electrons. To simplify the scattering model, the scattering is defined in the principle elastic: there is no changing of wavelength (classical physics) or no exchange of energy hν (quantum mechanics). Figure 2.5 (a) shows the scattering angle between incoming beam $\boldsymbol{k_{in}}$ and outgoing beam $\boldsymbol{k_{out}}$ is differing by 2θ. The scattered electric field is a superposition of all secondary waves that are generated from the material. Consider the scattering angle (see Fig.2.5(a)), one can find the vector $\boldsymbol{q} = \boldsymbol{k_{out}} - \boldsymbol{k_{in}}$. Due to not changing the wavelength $|\boldsymbol{k_{in}}| = |\boldsymbol{k_{out}}| = k = $
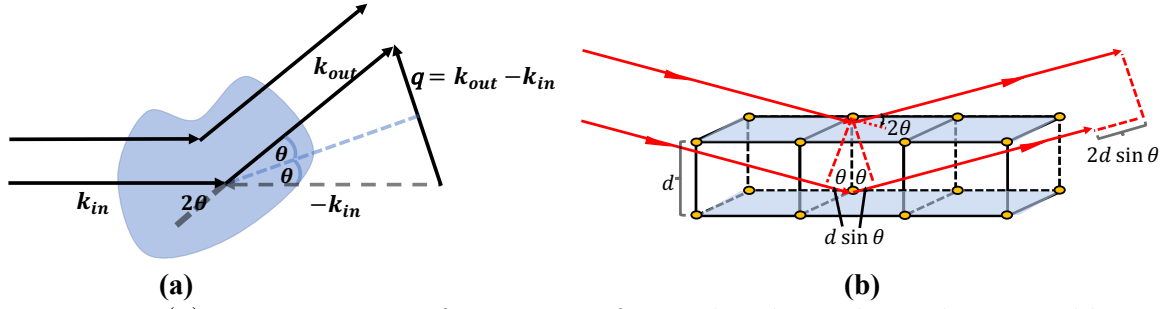
Figure 2.5: (a) Demonstration of scattering of a incident beam k_{in} and scattered beam k_{out}. The scattering vector is defined as $q = k_{out} - k_{in}$. (b) A sketch of the scattering of x-ray beam by an colloidal crystal. The path difference corresponds to the Bragg's law of diffraction: $2d\sin(\theta) = \lambda$, where d is the spacing between two colloidal planes, θ is the scattering angle, and λ is the wave length of the x-ray.

$2\pi/\lambda$, so one can define q as:

$$|\boldsymbol{q}| = q = 2k\sin\theta = \frac{4\pi}{\lambda}\sin\theta. \tag{2.16}$$

Lattice system	14 Bravais Lattices			
	Primitive	Base-centered	Body-centered	Face-centered
Cubic				
Teragonal				
Orthorhombic				
Monoclinic				
Triclinic				
Hexagonal				
Trigonal (Rhombohedral)				

Table 2.2: The seven crystal systems and 14 Bravis lattices in three dimension (adapted from source wikipedia.org)

The vector $\boldsymbol{q}$ is called the scattering vector or wave vector which is related to wave length, λ $(k = 2\pi/\lambda)$. Figure 2.5(b) showing, the scattering vector $\boldsymbol{q}$ is associated to the X-ray diffraction that originating from the colloidal particle which can be described by the Bragg's law of X-ray diffraction: $2d\sin\theta = \lambda$. The interplanar spacing d in the Bragg's law gives the detail how long the distance between particles is. So one can rewrite from above relations and on that in the equation 2.16 as:

$$|\boldsymbol{q}| = q = \frac{4\pi}{\lambda}\sin\theta = \frac{2\pi}{d}. \tag{2.17}$$

The equation 2.17 shows the scattering vector q is a inverse proportion of interplanar spacing which means at a small value of q is governed by a large interparticle distance, and **vise versa**. To expand scattering theory into a scattering of a crystallite, several scattering planes are involved. These specific planes that are hit by the incident X-ray are described by the *Miller indices* (hkl) which are a set of integers calculated from the reciprocal $(1/a, 1/b, 1/c)$ of plane-intercepts of the crystal axis system at points (a, b, c) (here, the detail how to construct the Miller indices will not be discussed). The *Bravais lattices* is introduced to classify crystal structures (see Table 2.2).

2.4.2 Scattering function of monodisperse particles

The scattered intensities of a colloidal dispersion depends on sizes, shapes, and relative positions of its particles. Here, only the spherical particle will be discussed since the interested colloidal particles are assumed having a spherical shape. The scattered intensity consists of a form factor $P(q)$ of the system, which describes the interference between scattering rays from different atoms inside a particle, and the second part is a structure factor $S(q)$ that describes the interactions between particles [48]:

$$I(q) = h\phi_s V_p \left(\rho_{solute} - \rho_{solvent}\right)^2 P(q)S(q). \tag{2.18}$$

Where $I(q)$ is the scattering intensity, h is the thickness of a sample, containing colloidal dispersions , ϕ_s is the volume fraction of colloidal dispersions, and ρ_{solute} and $\rho_{solvent}$ are the densities of scattering length of solute and solvent (in the work, the solvent is water and the solute is silica). For a spherical particle, radius of R_p, the

form factor $P(q)$ is given [15]:

$$P(q) = 9 \left[\frac{\sin(qR_p) - qR_p \cos(qR_p)}{(qR_p)^3} \right]^2. \qquad (2.19)$$

At high value of q, the form factor $P(q)$ is proportional to:

$$\lim_{q \to \infty} \left[\frac{3\sin(qR_p) - qR_p \cos(qR_p)}{(qR_p)^3} \right]^2 \propto \frac{1}{q^4}. \qquad (2.20)$$

The equation 2.20 is called the Porod's limit. The structure factor $S(q)$ is related to the radial distribution function, (or pair correlation function) $g(r)$ at interparticle distances r away from the origin by

$$S(q) = 1 + \frac{\phi_s}{V_p} \int_0^\infty (g(r) - 1) \frac{\sin(q_r)}{q_r} 4\pi r^2 \mathrm{d}r. \qquad (2.21)$$

At high q, the structure factor $\lim_{q \to \infty} S(q) \to 1$. According to Cabane et al [15], the liquid dispersion of monodisperse particles obeys the *Verlet-Hansen* criterion [56] (sometimes called *Verlet-Hansen* freezing rule) which is strict for hard spheres. It states that hard spheres in the liquid phase crystallizes when the first maximum structure factor $S_{max}(q)$ exceeds 2.85.

2.4.3 SAXS data acquisition

SAXS experiments were conducted using instruments of ID02 beam-line at the European Synchrotron Radiation Facility (ESRF) in Grenoble, France. The ID02 beam-line was equipped with a two dimensional area (2D) moving detector, a CCD camera (FReLoN 4M) with 2048 × 2048 pixels and 10 × 10 cm area [48]. The beam size was 200 μm in the vertical direction and 400 μm in the horizontal direction. The moving detector can be placed at 0.8 m and 10m away from the sample. The wavelength of the X-ray was 0.1 nm (12.4keV), giving q-range from 0.01 to 9 nm^{-1} [57].

Generally in SAXS measurement, the procedures starts with:

- Measuring background that arises from beam-line optics, the air, sample container, and the water signal which has high contributions at high $q-$value .

- Measuring form factors of all colloidal types from very diluted dispersions, e.g. 0.1% by volume (See next section).
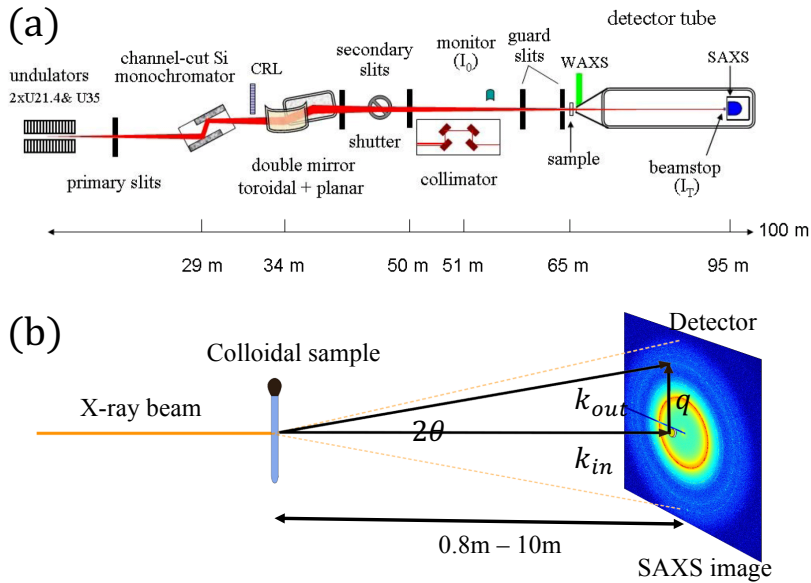
Figure 2.6: (a) Schematic of the SAXS equipments at the ESRF-ID02 beam-line in Grenoble, France. (b) schematic representation of data acquisition of silica TM50 in 5mM of NaCl, X-ray beam is scattered by sample and collected on a 2D detector (Figure(a) adapted from [57]).

- Exploring a sample by scanning across a sample (vertical scanning with the moving interval of 5 mm for the equilibrium sample, and horizontal scanning with moving interval of 0.5 mm for the interdiffusion samples) and interpreting SAXS 2D-images (see Fig. 2.7).
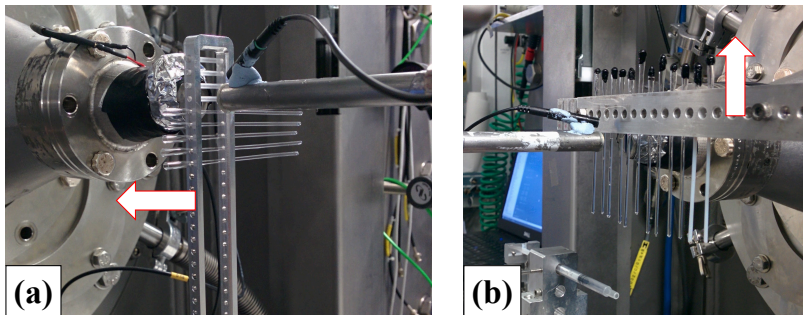
Figure 2.7: There are two ways to align a sample during SAXS scan: (a) A horizontal scan, the sample holder is moving to the left, while a sample is horizontally scanned from the left to the right. (b) A vertical scan, the sample holder is moving up, while a sample is vertically scanned from the top to the bottom. White arrows show the direction of moving sample holders.

During the measurement, scattering photons, which are elastically scattered by the sample, were collected on a movable 2D detector as the scattering signal and turned into a SAXS image (see Fig.2.6). The position of each pixel on the SAXS image was applied by a mask to remove faulty regions of image, normally caused by
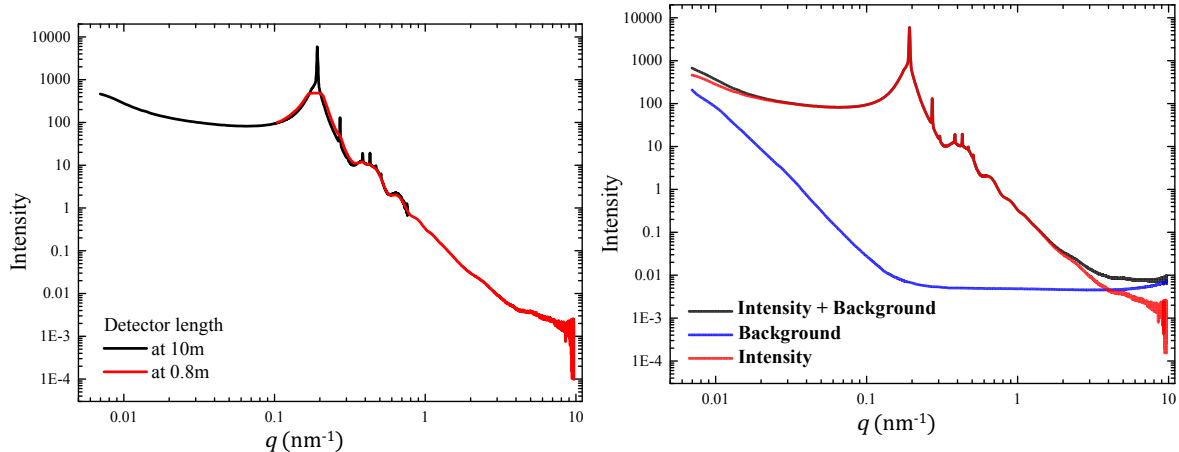
(a) Merging: Intensities of a sample at detector length of 0.8 m (black) and 10 m (red).

(b) Background Subtraction: the background intensity (blue), the merged intensity (black), and the subtracted intensity (red)
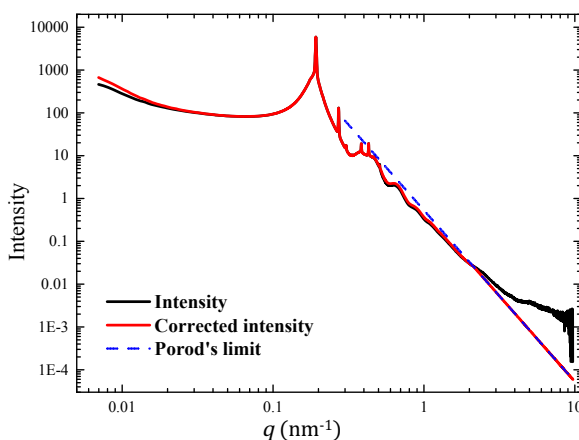
(c) Porod's limit correction: at high q, the
subtracted intensity is corrected according to
the Porod's limit $I(q) \propto q^{-4}$

Figure 2.8: Example of data treatment of a colloidal system, TM50 $\phi = 0.2044$.

the CCD and the beam stop, and were then collapsed by azimuthal averaging to give a one-dimensional (1D) scattering curve $I(q)$. All processes, as described above, was automatically analyzed by a software of ID02 beamline. Each sample was collected its scattering data $I(q)$ at the detector positions of 0.8 m and 10.0 m. These $I(q)$ were then merged together so that the scattering intensity covered the resolution, q range, of 0.01 to 9.0 nm^{-1} (see Fig.2.8(a)). The merged scattering data $I(q)$ still contained a background signal. These backgrounds were removed by subtracting the scattering intensity of the water in the container, which were measured earlier (see Fig.2.8(b)). The background-subtracted intensity $I(q)$ was then corrected by applying Porod's limit ($I(q) \propto q^{-4}$) at the high q, where the intensity was blurred out due to the azimuthal averaging in the first step. The final intensity contained only the

informations of a particle which consist of the form factor $P(q)$ and the structure factor $S(q)$
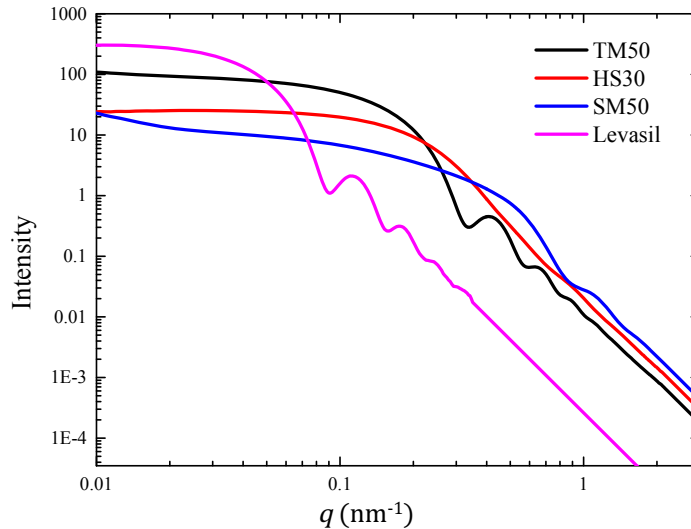
Figure 2.9: Form factors of different colloidal in the experiments: TM50(red), HS30(red), SM50(blue), and Levasil30(pink).
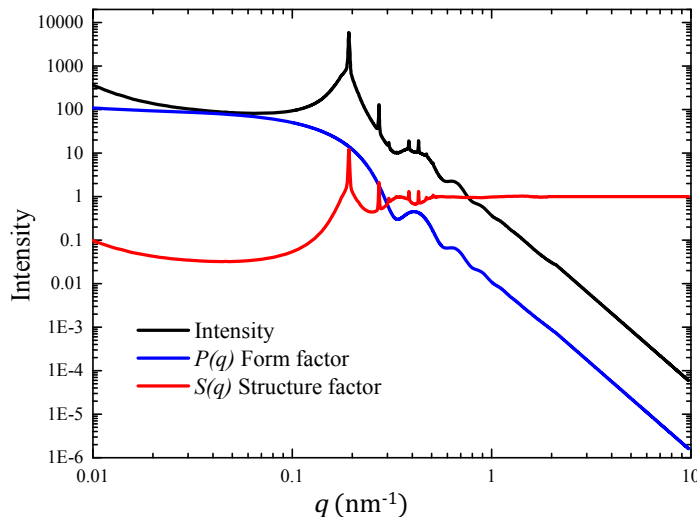
Figure 2.10: Analysis of silica dispersions, TM50 $\phi = 0.2044$: the scattering intensity (black), the form factor (blue), and the structure factor (red).

2.4.4 Form factor $P(q)$ and structure factor $S(q)$ analysis

Colloidal nanoparticles that are synthesized in the lab or are naturally occurring have either different or identical shapes and a finite size distribution. It is necessary to know information about the particle, here is colloidal silica, at the single particle level.

In this work, I used the traditional treatment of the SAXS analysis. First, the SAXS analysis of a sample begins with a form factor analysis to understand the

native physical properties of the particles in the sample. To do this, all types of colloidal dispersions in experiments were diluted to a very dilute dispersions (silica volume fraction $\phi_s \approx 0.1\%$) and extracted their scattering spectra. After that, the spectra were merged, background-subtracted, and tail-corrected (Porod's limit). The final scattering spectra were defined as the form factors $P(q)$ of each kind, example structure factors are giving in Fig.2.9. Following this, the subtracted form factor is fitting with the $SasView$ software [58] to obtain the radius of a particle and its polydispersity. Meanwhiles, the information of the interactions between particles of the system was expressed by the effective structure factor $S(q)$ which was calculated from the ratios of the scattering intensity $I(q)$ to the form factor $P(q)$ under the condition that $S(q) \to 1$ at large q. Example structure factors are giving in Fig.2.10.

2.4.5 Crystal structure analysis

For the 2D SAXS images that contain sharp diffraction spots (Fig.2.11(a)), superimposed on the liquid-like scattering pattern. These spots are the powder-diffraction pattern of small crystallites and will show a series of a powder spectrum (Fig.2.11(b)) on a one-dimensional (1D) scattering curve $I(q)$.
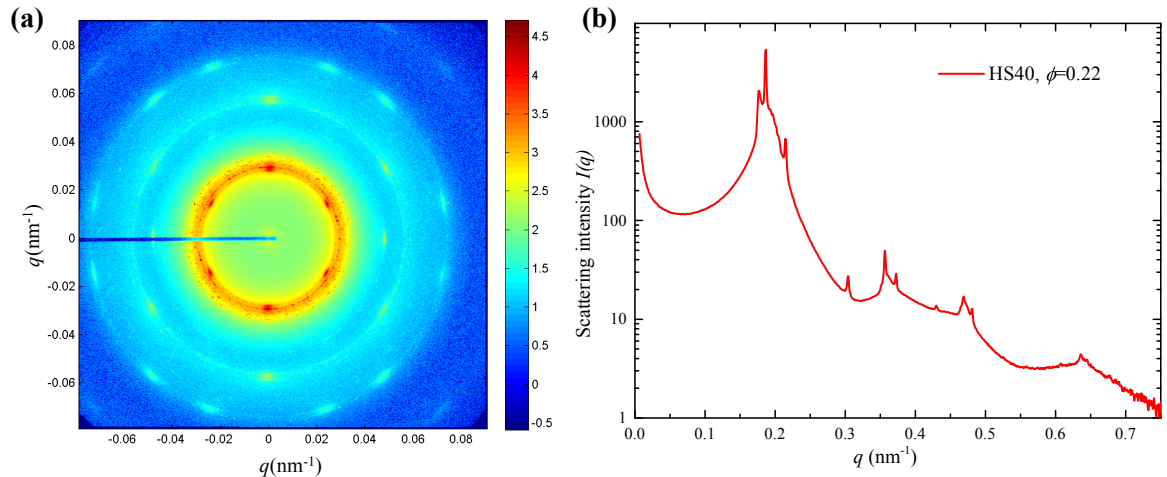
Figure 2.11: Example of a SAXS pattern of HS40, $\phi = 0.22$: (a) The 2D-SAXS pattern is superimposed by diffraction patterns of crystals (showed as spots in red (inner circle) and light blue (outer circles). The color scale shows the intensity of scattering x-ray beam on the detector (also see Fig.2.6(b)). (b) The 1D-spectrum of the scattering intensity $I(q)$.

In order to not decompose the intensity $I(q)$ in to form factor and the effective structure factor. However, here, the colloidal dispersions consist of two phases (liquid

and crystal states), one can no long assume that all sites are occupied by equivalent particles (see eq.2.18 and eq. 2.19). Therefore, the complex structure factor $S(q)$ is approximated as $S(q) \sim I(q)q^2$ for identifying (indexing) a structure of crystal in a colloidal system.

Lattice	$1/d_{hkl}^2$	Unit volume V
Cubic	$\dfrac{1}{a^2}\left(h^2 + k^2 + l^2\right)$	a^3
Orthorhombic	$\dfrac{h^2}{a^2} + \dfrac{k^2}{b^2} + \dfrac{l^2}{c^2}$	abc
Tetragonal	$\dfrac{h^2 + k^2}{a^2} + \dfrac{l^2}{c^2}$	a^2c
Hexagonal	$\dfrac{4}{3}\left(\dfrac{h^2 + hk + k^2}{a^2}\right) + \dfrac{l^2}{c^2}$	$\frac{\sqrt{3}}{2}a^2c$

Table 2.3: Perpendicular distance, d, between neighboring lattice planes {hkl} which used in this work, for different Bravais lattices (see Fig.2.2), and lattice constants a, b, c.

The following, I present an example of a real experiment to give an idea of how to identify the size and shape or packing of a crystallite from the X-ray diffraction scattering peaks. We will call this procedure "indexing". The interplanar spacing d_{hkl}, the shortest distance between neighboring lattice planes, of different Bravais lattices that are used in this work are shown in table 2.3. From the relationship between the interplanar spacing d_{hkl} and Miller indices hkl, the equation 2.17 can be derived as:

$$q^2 = \frac{4\pi^2}{d_{hkl}^2},\tag{2.22}$$

In case of a cubic lattice, $1/d_{hkl}^2 = (h^2 + k^2 + l^2)/a^2$ (see table 2.3), then

$$q^2 = \frac{4\pi^2}{a^2}\left(h^2 + k^2 + l^2\right),\tag{2.23}$$

where a is the edge length of cubic unit cell such that $\dfrac{4\pi^2}{a^2}$ is a constant, where a is the lattice constant. So the scattering vector q is proportion to the square root of the Miller indices ($N = \sqrt{h^2 + k^2 + l^2}$).

The complex structure factor contains informations of the amplitude and the phase of a scattering beam, is derived by [59]

(hkl)	$N = \sqrt{h^2 + k^2 + l^2}$	primitive	body-centered	face-centered
100	$\sqrt{1}$	✓	✗	✗
110	$\sqrt{2}$	✓	✓	✗
111	$\sqrt{3}$	✓	✗	✓
200	$\sqrt{4}$	✓	✓	✓
210	$\sqrt{5}$	✓	✗	✗
211	$\sqrt{6}$	✓	✓	✗
220	$\sqrt{8}$	✓	✓	✓
300, 221	$\sqrt{9}$	✓	✗	✗
310	$\sqrt{10}$	✓	✓	✗
311	$\sqrt{11}$	✓	✗	✓
222	$\sqrt{12}$	✓	✓	✓

Table 2.4: An example of selected Miller indices for reflections in cubic crystals

$$S_{hkl} = \sum_{i}^{n} f_i e^{-2\pi(hx_i + ky_i + lz_i)} = S_{000} + \sum_{i,(hkl)\neq(000)}^{n} f_i e^{-2\pi(hx_i + ky_i + lz_i)}, \qquad (2.24)$$

where S_{hkl} is the complex structure factor, S_{000} is the structure factor at (000) or the form factor of a particle, f_i is the form factor of ith atom, x_i, y_i, z_i are coordinates of ith atom, and h, k, l are the Miller indices. Consider the equation 2.24, there is a set of the Miller indices that canceling the contribution of scattering x-ray due to the non-coherence in phases (destructive interferences). Therefore, when indexing a powder spectrum, there is a specific set of Miller indices (hkl) that corresponds fo each crystal structure. Powder spectra of basic crystal structures (e.g. bcc, fcc, and hcp) were able to be indexing by Matlab software, but for a very complex powder spectra, they were send to a crystallographer to index them.

Table 2.4 shows a rule of reflections for cubic systems. According to $q \propto N$, one can predict arbitrary scattering-peak positions of a crystal structure by using a relationship:

$$q_{pre} = q_0 \frac{N}{N_0}, \qquad (2.25)$$

where q_{pre} is a predicted scattering-peak positions, q_0 is the primary peak position appears in the spectrum, N_0 and N are the square root of Miller indices at the first and the predicted position. Table 2.5 presents a set of the Miller index ratios $((N/N_0)^2)$ that was used in this experiments.

Figure 2.12 and table 2.6 show an indexing of a crystal of a colloidal sample, TM50

Structure	Ratio $(N/N_0)^2$
Cubic: BCC	$1:2:3:4:5:6:7:8:9:10:11:12:13:14:...$
Cubic: FCC	$3:4:8:11:12:16:19:20:24:27:32:35:36:...$
Hexagonal: primitive structure $(c = \sqrt{(8/3)}a)$	$9:32:36:41:68:81:96:105:113:128:132:137:$ $144:164:176:177:209:224:...$

Table 2.5: A Miller index ratios N/N_0 of bcc, fcc, and hcp with $c/a = \sqrt{(8/3)}$. These crystal structures are observed in this experiments.
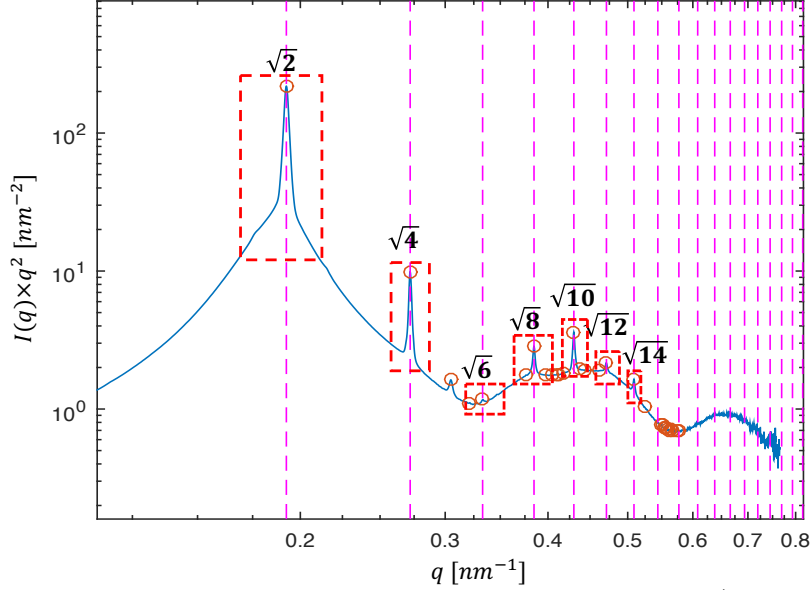
Figure 2.12: A result of the peak detection software of a sample (TM50 $\phi = 0.2044$): the predicted peak positions are labeled with dotted lines (pink). The dominant peaks are marked by red cycles. The peak positions of a crystal appear at $q = 0.1923, 0.2720, 0.3334, 0.3847, 0.4300, 0.4709$, and 0.5088 which correspond to $N = \sqrt{2}, \sqrt{4}, \sqrt{6}, \sqrt{8}, \sqrt{10}, \sqrt{12}$, and $\sqrt{14}$.

$\phi = 0.2044$. The complex structure factor $(I(q) \times q^2)$ is detected to have powder spectrum with at least seven peaks coexistent. By taking every q peak positions (see Fig. 2.12) and divided them by the primary peak $q_0 = 0.1923$, one can obtain that each q/q_0 ratios agrees with the N/N_0 ratios of a body-centered cubic structure (see table 2.6).

The superimposing powder spectrum are separated from the liquid phase by a Matlab code. All subtracted peaks are collected as power spectrum of a crystal phase in colloidal dispersions. The residual spectrum is then interpolated in order to fill holes from the subtraction process. Finally, the filled residual is used as a liquid phase spectrum of a colloidal dispersion (see Fig. 2.13).

h	k	l	q_{exp}	q_{pre}	N	$[q_{exp_n}/q_{exp_0}]^2$	$(N/N_0)^2$
1	1	0	0.1923	0.1923	$\sqrt{2}$	1.000	1
2	0	0	0.2720	0.2720	$\sqrt{4}$	1.999	2
2	1	1	0.3334	0.3331	$\sqrt{6}$	3.004	3
2	2	0	0.3847	0.3847	$\sqrt{8}$	4.000	4
3	1	0	0.4300	0.4301	$\sqrt{10}$	4.998	5
2	2	2	0.4709	0.4711	$\sqrt{12}$	5.994	6
3	2	1	0.5088	0.5089	$\sqrt{14}$	6.998	7

Table 2.6: Peak positions of the experiment and prediction of the body centered cubic. q_{exp} are the peak position obtained from the experiment, while q_{pre} are the predicted peak positions calculated by eq. 2.25, $q_0 = 0.1923$.
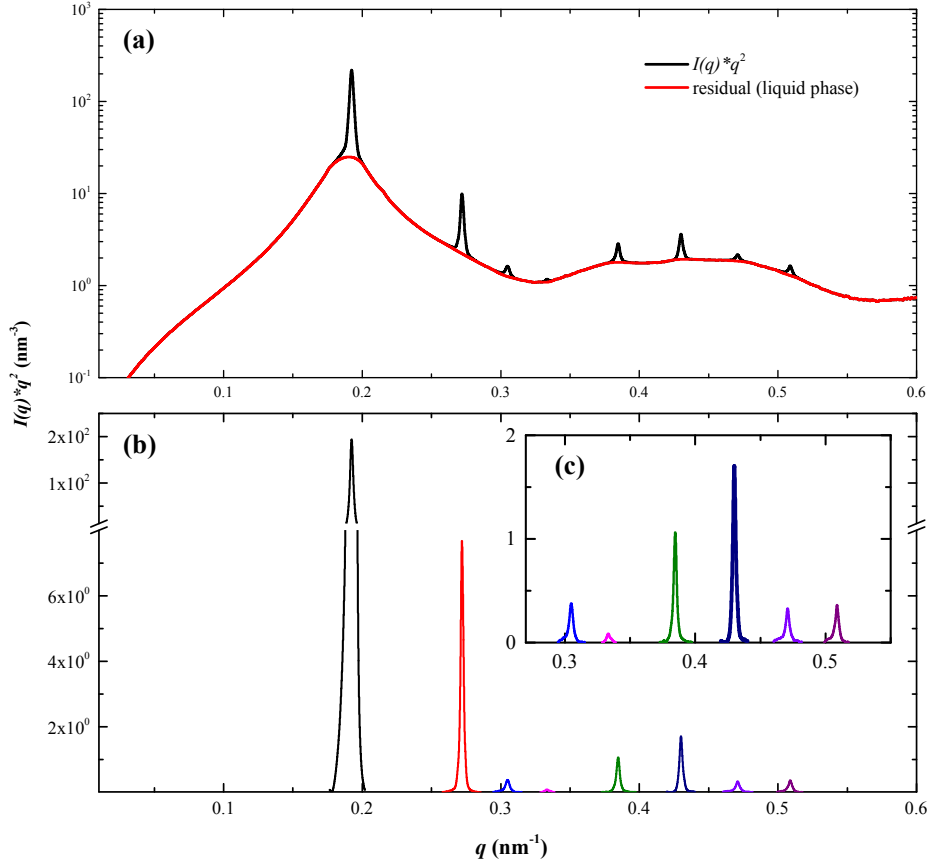

Figure 2.13: The subtraction of a powder spectrum of TM50, $\phi = 0.2044$: (a) The original complex structure factor $s(q)$) (black) and the residual or the liquid phase (red). (b) and (c) Subtracted peaks are powder spectrum of colloidal dispersions.

Chapter 3

Colloidal Crystals

Previous theoretical works [11, 12, 14, 60, 61] have predicted that polydisperse hard sphere are able to build crystalline structures, and with the coexistence of different complex phases, although a small changing in polydispersity can interrupt the crystalline order. Recently, there are both experimental and simulation works of a colloidal system [15, 16, 48]: the experiment showed that an aqueous dispersions of colloidal silica with a broad monomodal size distribution (Ludox HS40 equilibrated against NaCl solution, 5mM, pH 9-10) has a capability of fractionated crystallization with different structures (bcc, Laves AB_2, liquid) coexisting. Meanwhile the simulation showed a monomodal polydisperse populations, charge-stabilized, can build complex colloidal crystals by fractional crystallization due to interact through a soft potential increasing their tolerant to crystallize even at a high polydispersity .

The interesting questions that still need to be answered:

(1) Are there another possible structures could be discovered? Are they large or small?

(2) How do the changing of interaction forces, the particle size, and the volume fraction have the effect on phases of a colloidal structure.

(3) How and when does the colloidal-crystal nucleation take place, and are the colloidal crystals stable?

In this chapter, I report small-angle x-ray experiments on several osmotically compressed systems of colloidal silica with a broad monomodal size distribution (see table 2.1). These colloidal particles were equilibrated under different osmotic pressures giv-

ing various volume fractions of final aqueous samples. Moreover, I also observed the nucleation and growth of crystals in a sample, and the appearance of crystals in the diffusion of two different volume fraction samples.

3.1 Ludox TM50 colloidal silica

3.1.1 Osmotic pressure curve

Aqueous dispersions of colloidal silica (Ludox TM50) were used as received. Ludox TM50 of 80 samples were dialyzed against aqueous solution of PEG (0.5 - 5 mg/ml) and NaCl (0.5 - 50 mM). After a dialysis was complete, most of the samples behaved rheologically as fluids and were preserved in a tube with a closure preventing them from the deterioration when stored for a long period of time. Volume fractions ϕ were measured by the dry extract method of section 2 and the osmotic pressures were computed by equation 2.9. The results of volume fractions and osmotic pressures measurement are presented in the Fig.3.1. The volume fraction increases with the increasing of PEG concentration.
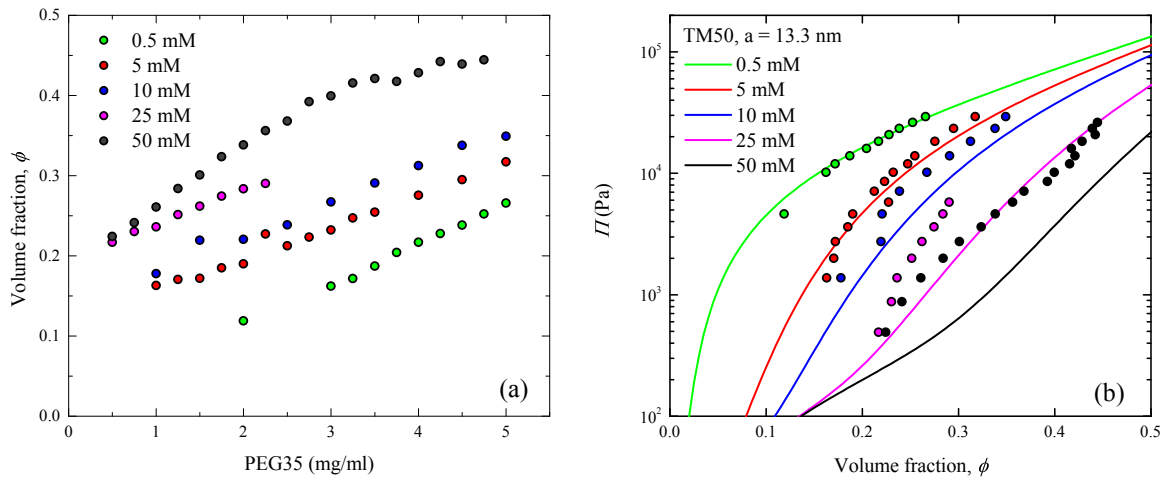
Figure 3.1: (a) Volume fractions of dialyzed silica dispersions, Ludox TM50, as a function of concentration of PEG. (b) Evolution of osmotic pressures in silica dispersions as a function of the colloidal volume fraction. The symbols shows results for the different concentrations of NaCl solution between 0.5 - 50 mM.

The SAXS experiments have been performed in order to quantitative study the phase diagram and the dynamics of nucleation. As mention earlier, the form factor was quantified by a scattered intensity of a diluted dispersions, $\phi = 0.1\%$. The best
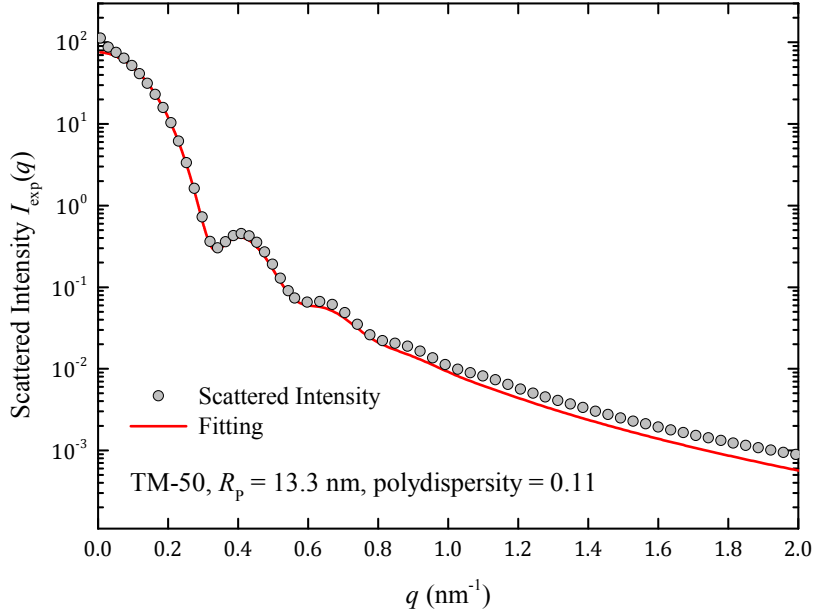
Figure 3.2: The form factor of Ludox TM50 is a scattered intensity of a diluted dispersion of Ludox TM50 (circles), $\phi_s = 0.1\%$ and a theoretical fitting line (red) by *Sasview* software.

theoretical scattered intensity were fitted by using a small angle scattering analysis software - *SasView* [58] using the polydispersity of $11.1 \pm 0.3\%$ and the radius of colloidal spheres $R_p = 13.3 \pm 0.6$ nm. Robert Botet, a collaboration in France, also calculated the particle size of TM50 by using his own developed inversion formula for SAXS of polydisperse spheres [62]. His result is shown in fig.3.3 with the article radius of 13.75 nm and polydispersity of 10%. The particle size from this method agreed with the fitting from *SasView*. Goertz et al. [63] have also measured particle sizes of TM50 and HS40 by other different means (They used analytical ultracentrifuge (AUC), small angle x-ray scattering (SAXS), transmission electron microscopy (TEM)). The averaged particle size and polydispersity of TM50 from their measurements were a diameter of 25-28 nm and polydispersity of 12-15% as shown in fig.3.4, with in good agreement with that from *SasView*.

28
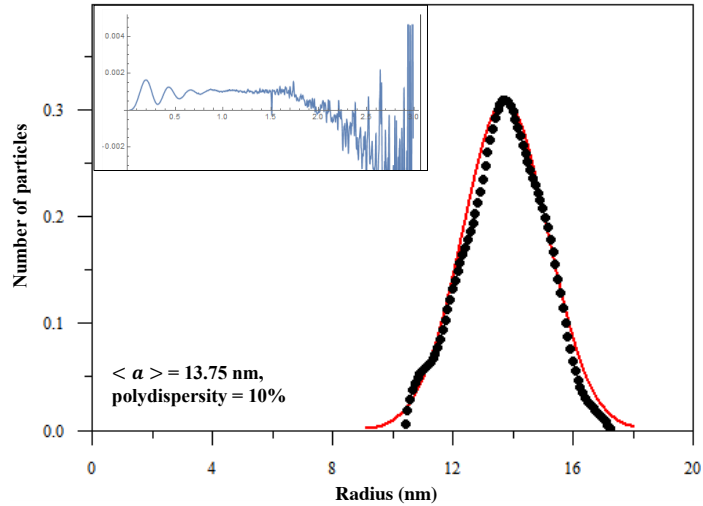
Figure 3.3: The size of Ludox TM50 is fitted by using the inversion formula for SAXS of polydisperse spheres [62]. The fitting size particle of TM50 by Gaussian distribution is 13.75 nm, and polydispersity of 10%. The top left panel is the inversed radius distribution of TM50. (Reproduce with permission from Robert Botet)

.

Method		TM50 mean diameter (polydispersity)	HS40 mean diameter (polydispersity)
TEM		28.1 nm (12.1 %)	16.3 nm (14 %)
SAXS	Gauss	26.3 nm (12.9 %)	14.4 nm (18.3 %)
	Log Normal	27.0 nm (12.8 %)	15.2 nm (17.2 %)
	MEM	27.1 nm (15.5 %)	12.1 nm (43.9 %)
AUC		25.3 nm (14.8 %)	14.9 nm (14.4 %)
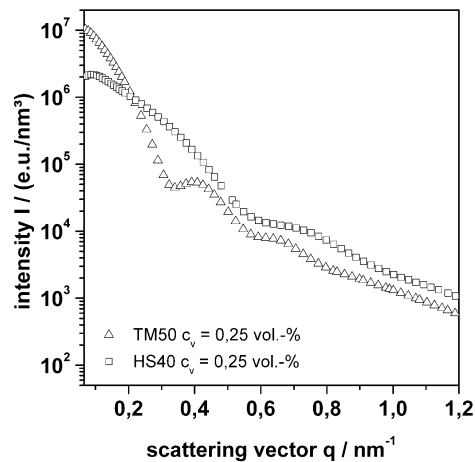
Figure 3.4: (top): A mean diameter and polydispersity obtained from TEM, SAXS and AUC for TM50 and HS40. (bottom): The SAXS intensities of TM50 and HS40 according Goertz et al. (Reproduced from [63])

.

3.1.2 Phase diagram

In order to investigate the electrostatic effect on the crystal populations, five sets of Ludox TM50 samples were dialyzed by changing the concentration of salt, NaCl, in the buffer solutions as described in the previous section. A crystal structure of colloidal particles in dispersions can be evaluated by detecting a pattern of sharp diffraction peaks which superimposed on the liquid phase intensity.
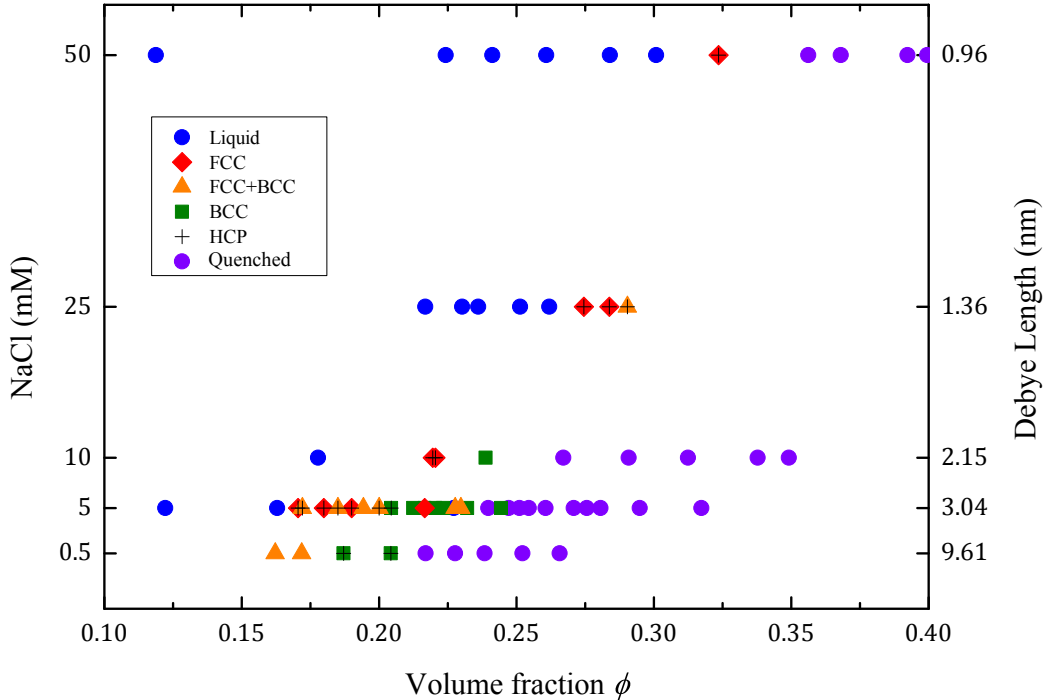
Figure 3.5: A phase diagram of colloidal dispersions Ludox TM50 (radius of 13.3 nm and polydispersity of 11%) equilibrated at NaCl concentrations of 0.5, 5, 10, 25, and 50mM. The symbols represent phases of colloidal at different volume fractions and salt concentration; liquid (blue circle), fcc (red diamond), fcc+bcc (orange triangle), bcc (green square), hcp (plus sign), and quenched (purple circle).

Figure 3.5 shows a phase diagram of Ludox TM50 with salt concentration and Debye length as a function of ϕ. At salt concentration of 5.0 mM shows results with multiple crystals coexistence. For instance, in the Fig. 3.7 shows a structure analysis by peak-position indexing of samples in 5 mM NaCl solution: below $\phi = 0.16$, particles behaves as colloidal liquid, then at $\phi = 0.19$, the liquid phase appeared together with the first sharp peak pattern indexing as a face centered cubic (fcc) structure. At $\phi = 0.20$, liquid phase superimposed by two crystal structures which were indexed as fcc and body centered cubic (bcc) structure. At higher volume fraction $\phi = 0.22$, fcc disappeared and only liquid phase and bcc were observed. At higher ϕ, eventually,

30

the colloidal crystal quenched.
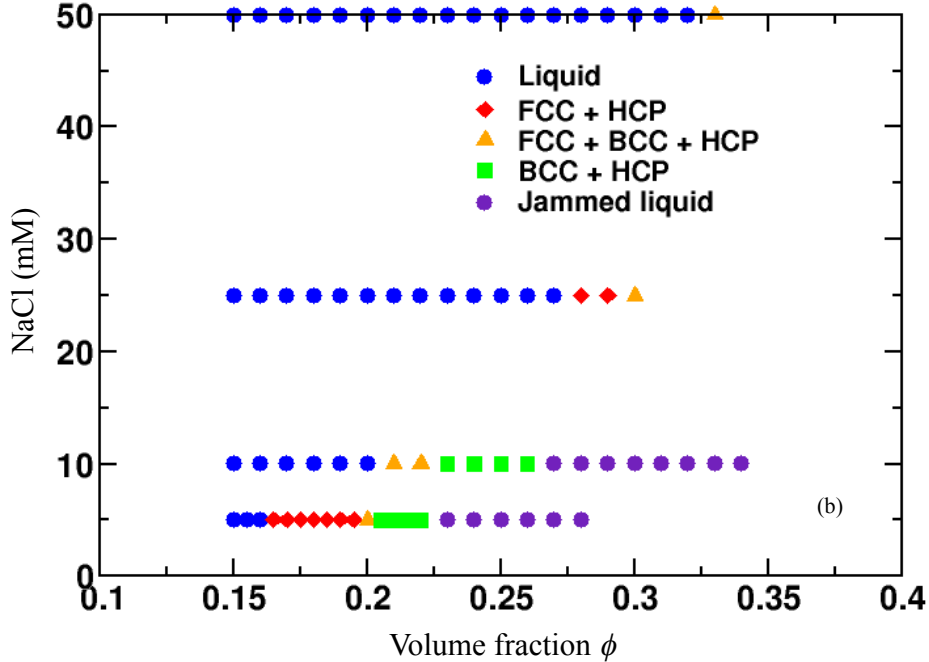
Figure 3.6: A predicted phase diagram obtained from simulation of Ludox TM50, radius of 13.75 nm and polydipersity of 10% equilibrated at NaCl concentrations of 5, 10, 25, and 50mM (Reproduced with permission from Guillaume Bareigts and Christophe Labbez).

In order to compare to the results found in this study, the fractionation of Ludox TM50 was investigated through Monte Carlo numerical simulations by Guillaume Bareigts and Christophe Labbez, our collaborative researchers from Dijon, France. The polydisperse cell model [64] and the charged regulation model [65] were used for numerical simulations of identification between the fcc,bcc, and hcp phases . Figure 3.6 presents simulation results of Ludox TM50 equilibrated at NaCL of 5, 10 ,25 and 50mM. The simulations are in very good quantitative agreement with the experimental data. The simulation was able to predict all crystal structures which found in the experiments, the initial volume fraction where each crystal phases appeared in every salt concentrations (5 to 5o mM, NaCl). It also predicted the coexistence of hcp structure which was not noticed or dis not appear in a spectrum.

After the simulation results came out, all spectra were re-indexed, and a small bump was found to be a possible scattering peak contributed by the hcp structure. This small peak appeared in samples, in which contained a fcc phase, with a relative ratio $0.94 \approx \sqrt{32/36}$ to the primary peak of fcc (111) (see fig.3.7), but it disappeared when fcc was absent or at higher ϕ. The origin of the additional peak is unknown,
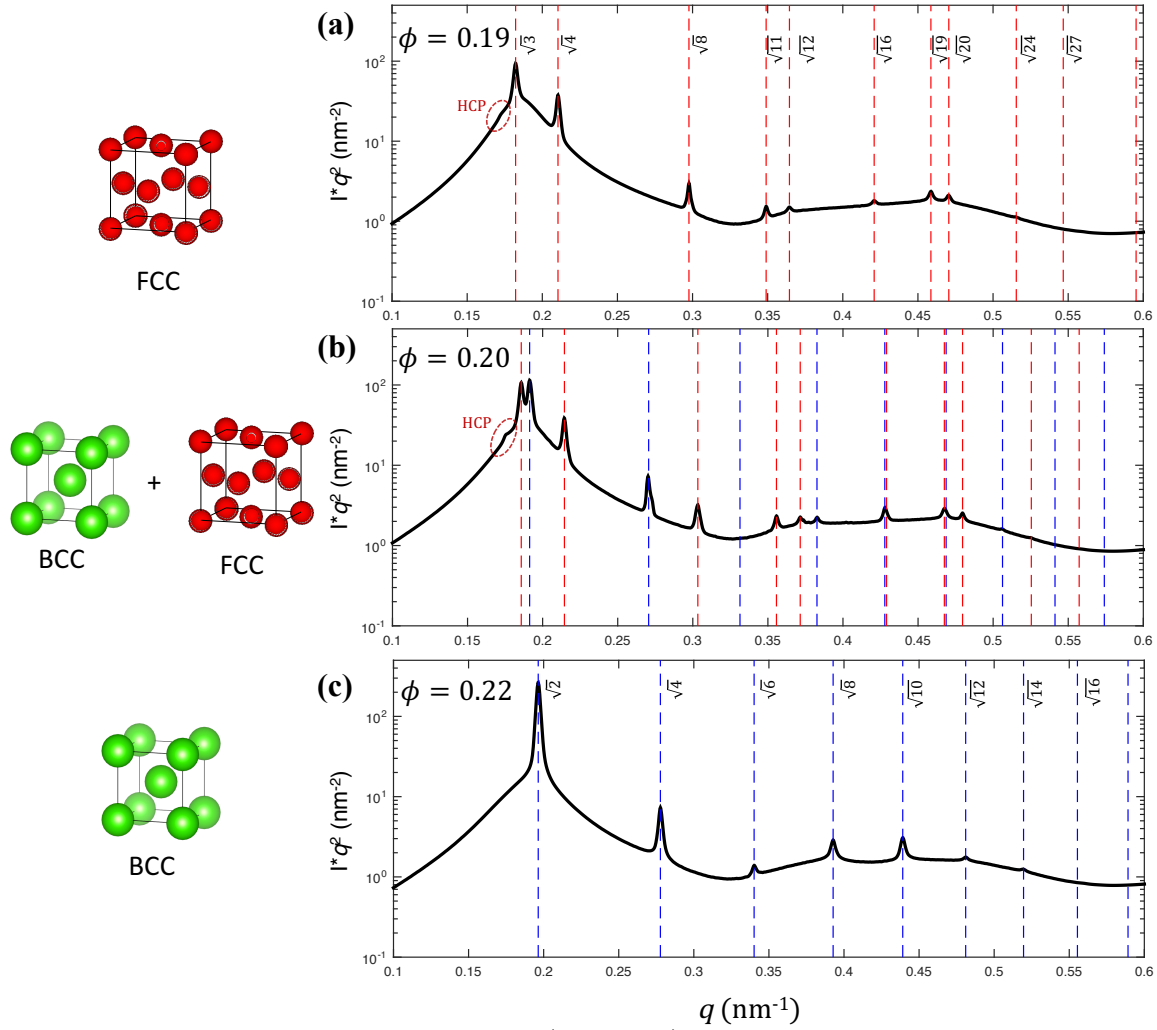
Figure 3.7: Example of peak detection (indexing) of Ludox TM50 and the evolution of colloidal crystals: (a) at $\phi = 0.19$, particles were in the liquid phase, fcc, and hcp. (b) at $\phi = 0.20$, coexisting of liquid phase and crystals (bcc, fcc, hcp). (c) at $\phi = 0.22$, fcc and hcp were disappear, only the liquid and bcc phase existed.

but suggested to come from a local disorder of fcc structure causing the size or the range order related to the hcp peak (100) at the additional peak. This can happen in the case of high quality data of micelles or colloids because the energy difference between fcc and hcp is not so large [66]. According the packing configurations of fcc and hcp are close packed structures with possible layers denoted by A, B and C; the fcc structure has layer sequences A-B-C-B-A-B, while hcp structure has that of A-B-A-B-A-B. If there is a changing in fcc layer from C to A, the hcp then exists. This wrong alignment of a layer in the fcc structure may be the origin of the bump. This bump was also found in the spectra of the bcc structure but very small.
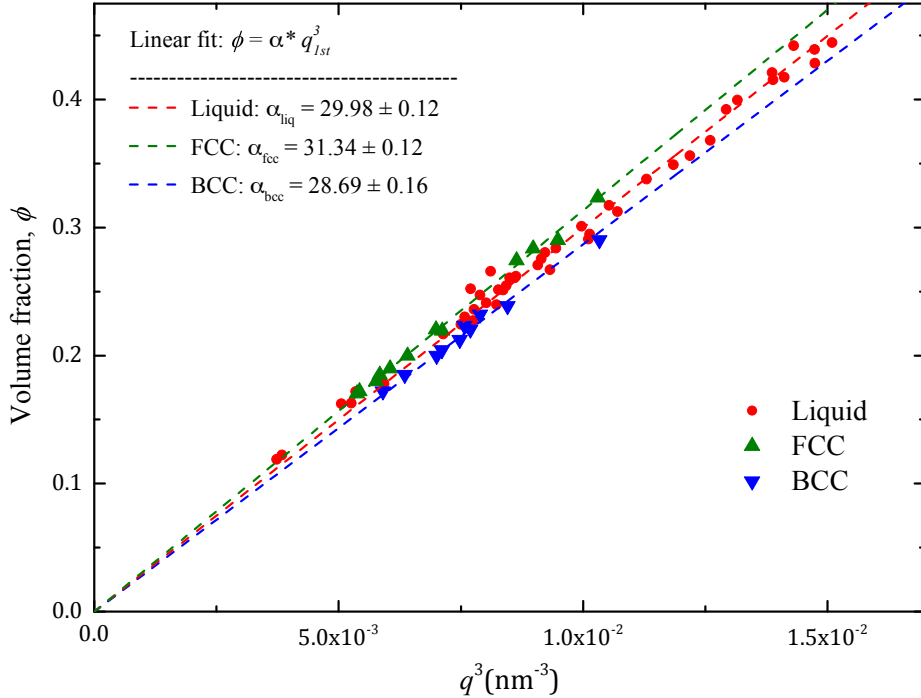
Figure 3.8: Ludox TM50; a calibration curve of volume fraction, ϕ as a function of q_{1st}^3 (nm^{-3}) for liquid phase (red dot), fcc phase (green triangle), and bcc phase (blue inverted triangle).

Since the primary peak of structure factors, q_{1st} or q_0, is related to the local volume fraction of colloidal dispersions: when volume fraction of a colloidal dispersion is increased, the primary peak q_{1st} and its following q peak were shifted to the right (larger q-value). One can plot a relationship between the primary peak of structure factors q_{1st} of each phase in a colloidal dispersion and its local volume fraction to obtain a calibration curve for each phase by using a relationship from [48]:

$$(q_{1st})^3 = \frac{36\pi^2\sqrt{3}}{(2R_p)^3}\phi. \tag{3.1}$$

Figure 3.8 shows calibration curves of liquid, bcc, and fcc phases for TM50 corresponding to equation 3.1. The calibration curve also show the relationship of the relative density (V/ϕ) or compare a unit cell size $(\alpha \propto R_p^3)$ of each crystal structure by only compare the α of each phase, where α is a slope of a calibration curve. These calibration curves will be used to study, by observing a changing of volume fraction, the interdiffusion of colloidal mixtures, the nucleation and growth of a crystal or liquid phase, as well as its drying in a Hele-Shaw cell.

33

3.1.3 Interdiffusion experiments

Theoretical prediction for the diffusion of non-homogeneous dispersions

In this part, we consider the diffusion process of colloidal particles in a sample, length of l, which has different initial concentrations (ϕ_1 and ϕ_2) at both ends but do not mix at the beginning (Fig.3.9 (b)). For a single sphere in liquid medium, the movement of particles is caused by a thermal fluctuations the so-called Brownian motion. The self-diffusion coefficient or diffusivity (known as Stokes-Einstein relation) is given by

$$D_0 = \frac{kT}{6\pi\mu a},$$
(3.2)

where kT is thermal energy, μ is the viscosity of the fluid medium, and a is the radius of the sphere. Since our colloidal system consists of a large number of charged spheres, the calculation of mass transport, diffusion, of particles is to consider the collective process, the relaxation of a concentration gradient due to potential (thermodynamic and osmotic pressure) and hydrodynamic interaction. From previous works [22, 67–70], the collective diffusivity D_c of particles was corrected as the Stokes-Einstein diffusivity with respect to the volume fraction ϕ of the particles:

$$D_c = D_0\tilde{D}(\phi).$$
(3.3)

Here, $\tilde{D}(\phi)$ is the dimensionless diffusivity which can be calculate from the experiment. Applying the Fick's law of diffusion with the collective diffusivity to build a model for the interdiffusion experiment, one can predict the volume fraction $\phi(x,t)$ as a function of time t and position x from the diffusion equation:

$$\frac{\partial \phi}{\partial t} = D_c\frac{\partial^2 \phi}{\partial x^2},$$
(3.4)

with initial conditions

$$\phi(x,0) = \begin{cases} \phi_1, & \text{for } -l/2 < x < 0 \\ \phi_2, & \text{for } 0 < x < l/2, \text{ where } \phi_2 > \phi_1. \end{cases}$$

The analytic solution of equation 3.4 is calculated by the separation of variables

method combined with Fourier series, the solution:

$$\phi(x,t) = \frac{\phi_2 + \phi_1}{2} + \frac{\phi_2 - \phi_1}{2} \sum_{n=1}^{\infty} \frac{4}{(2n-1)\pi} \sin\left(\frac{(2n-1)\pi x}{l}\right) e^{-\frac{(2n-1)^2 \pi^2}{l^2} D_c t}. \quad (3.5)$$

Note that, here D_c was assumed to be constant, rather than $D_c = D_0 \tilde{D}(\phi)$, otherwise the diffusion equation will be written as:

$$\frac{\partial \phi}{\partial t} = \frac{\partial}{\partial x}\left(D_0 \tilde{D}(\phi) \frac{\partial \phi}{\partial x}\right). \quad (3.6)$$

Therefore, the equation 3.4 is a simplified of equation 3.6.
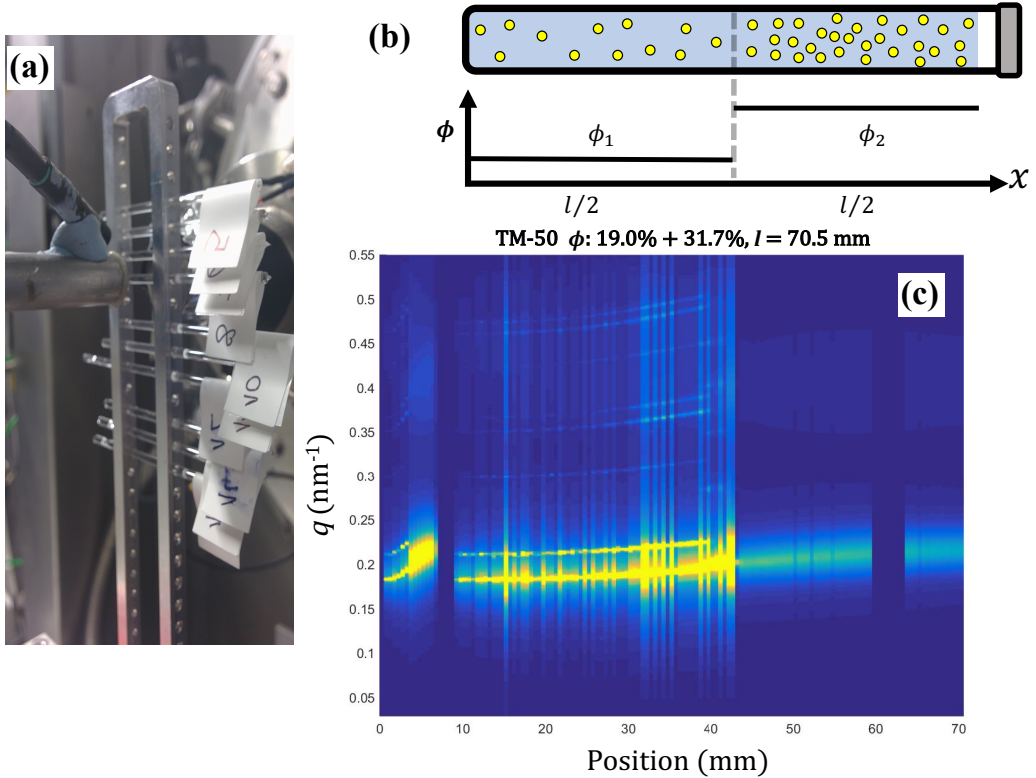
Figure 3.9: (a) Small angle X-ray scatterng (SAXS) setup of interdiffusion samples. (b) The interdiffusion sample geometry showing the initial condition with two different volume fraction dispersions, filled in a capillary with the same length $l/2$ (in the experiments $l \approx 30$-35 mm). The (c) The SAXS image of a interdiffusion sample of Ludox TM50 prepared by using initial volume fractions ϕ 0.190 and 0.317. Interpreting of scattering stripe patterns of the sample; at position 0-38mm is the fcc structure, 38 - 42 mm is bcc structure ,and from 42 mm is liquid phase. At 60-65 mm, the beam hit the sample holder resulting in no spectrum is detected.

Experiments

Four interdiffusion samples of Ludox TM50 (equilibrated at NaCl solutions of 5mM, pH 10) were prepared by equally injecting two dispersions, with volume frac-

tions ϕ of 0.190 and 0.317, in a capillary and allowed both dispersions to inter-diffuse over time. On the day of the experiment, samples were 5, 8, 15 and 23 days old. Each sample was investigated through SAXS and extracted scattered intensity of liquid phase and the primary peak of crystals were extracted if they appeared. Figure 3.9 shows a schematic of experimental setup and scanning SAXS-image over an interdiffusion sample. The primary peak position of fcc, bcc and liquid phases were converted into a volume fraction by fitting with the calibration curve in the Fig. 3.8.
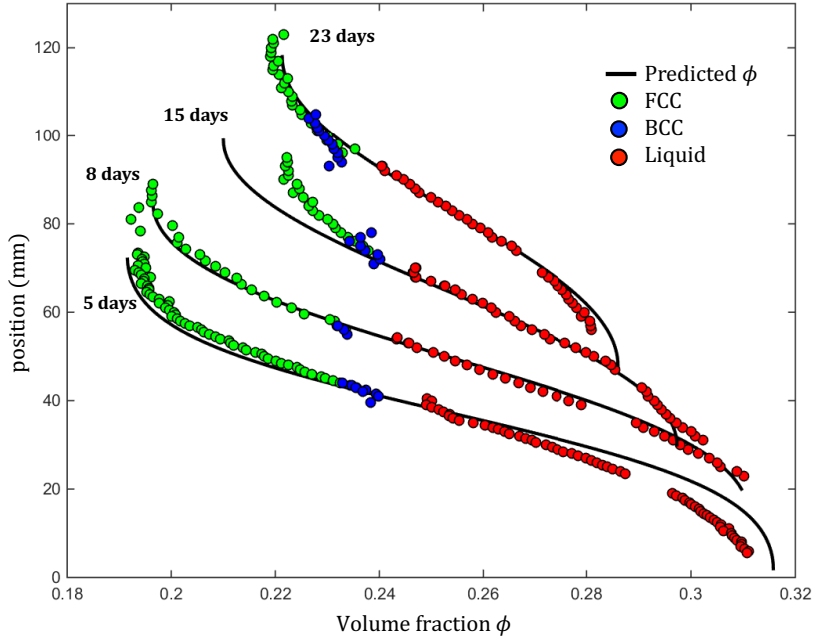
Figure 3.10: Interdiffusion experiments on colloidal dispersions Ludox TM50 (particle size 13.3 nm, the initial volume fraction ϕ of 0.190 and 0.317) shows time-evolution of the diffusion process building the bcc structure at the boundary of two dispersions. The solid lines give a predictions from the diffusion model (equation 3.5) with the average dimensionless diffusivity $\tilde{D} = 15$.

Figure 3.10 presents the results of these experiments with the corresponding model predictions. For particle volume fraction $\phi = 0.190$, the particles form the fcc structure and liquid phase, meanwhiles $\phi = 0.317$ particles are in liquid phase. After few days of the diffusion of two particle volume fractions, the bcc structure is build at the volume fraction between ϕ 0.22 to 0.24 which agree well with the phase diagram (Fig. 3.5). The numerical model, we quantify the dimensionless diffusivity $\tilde{D} = D_c/D_0 = 15$ for Ludox TM50 by best-fitting to the experiment data, only for volume fraction ranges of 0.19 to 0.32. Indeed, the collective diffusion D_c depends strongly on the volume fraction ϕ which will be discussed with experimental results in the next chapter.

The gaps in the middle of each spectrum were approximately a position of a sample holder that hinders the x-ray scattering. Meanwhile in the equilibrium samples of TM50, the bcc structure appeared at $\phi = 0.17$ to 0.25 and at $\phi = 0.17$ to 0.22 for the fcc structure. If the diffusion process is end, the final volume fraction of TM50 mixtures will be $\phi = 0.25$. At this volume fraction, liquid and bcc phase should be accommodated by particles in the TM50 mixtures according to the phase diagram. This corresponds to the phase space in capillaries that particles trend to behaviors in order to stay in the liquid phase and the bcc phase rather than being in the fcc phase and expressed on a decreasing of the length of position where fcc phase was detected.

3.1.4 Crystal nucleation and growth

In this part, we studied a real-time kinetics of crystals growth and nucleation by the population of particles in the Ludox TM50 over about 24 hours. The experiments was conducted after we have known the equilibrium phase behaviour of Ludox TM50. We prepare a new set of samples as fresh by diluting a very concentrated dispersions (quench liquid of Ludox TM50 equilibrated at 5mM of NaCl, pH =10) to the volume fraction ϕ of 0.19, 0.20 and 0.22, since within this range showed the presence of crystals, samples were analyzing immediately after the dilution. The q-value of the liquid and crystal peaks were obtained from SAXS and converted to their volume fraction ϕ. After 13 and 17 hours, samples were remeasured in order to observe the evolution of phases.

TM50, $\phi = 0.19$: From the phase diagram (see Fig.3.5) at $\phi = 0.19$ is the middle range where the fcc structure existed without coexistence of the bcc. In the kinetics experiment, the system developed slowly with a small increasing of the liquid peak height and on crystal structures was detected at this period. After 13 hours, the first signal of a weak fcc structure appeared and grew up gradually (see Fig.3.11).

Figure 3.12 shows indirectly of creasing of the amount of a crystal phase and changing of volume fractions over time. Here, the nucleation was slow, especially at this volume fraction $\phi = 0.19$, where the phase boundary is. A shift of the area $I(q) \cdot q^2$ may be a result of the electron filling in the beamline which does not effect on the volume fractions.
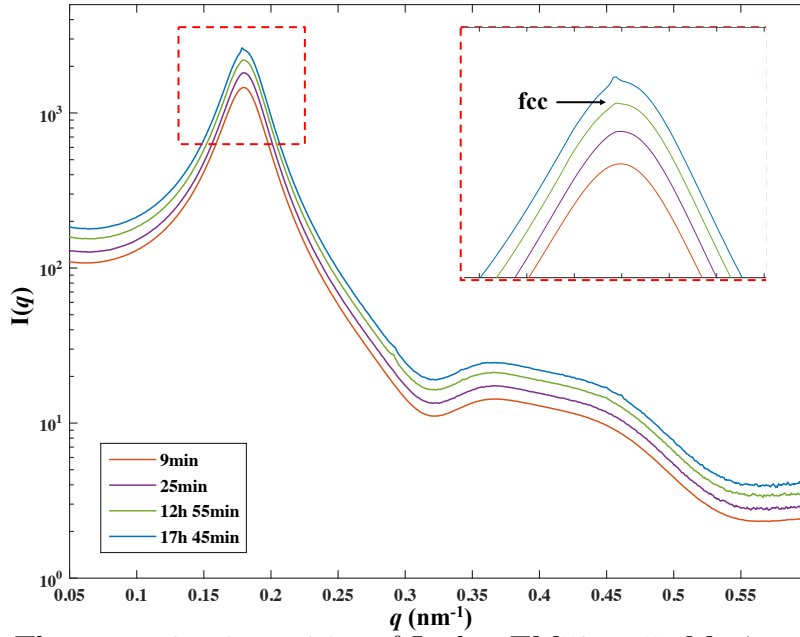
Figure 3.11: The scattering intensities of Ludox TM50 at 5mM, $\phi = 0.19$. The fcc structure peak appear superimposing on the liquid phase after 13 hours of nucleation.

Figure 3.12: The nucleation analysis of TM50 $\phi = 0.19$: (top) The area under the $Iq^2 \cdot q (nm^{-3})$ curve which relate to the occupancy of particles in liquid and fcc phases. (bottom) The evolution of volume fraction over time.

TM50, $\phi = 0.20$: From the phase diagram (see Fig.3.5) at $\phi = 0.20$, one expects the liquid phase together with two crystal structures (bcc and fcc). In the kinetics experiment, the fcc structure evolved rapidly with 10 minutes after dilution and continued growing in term of the number of the fcc crystals. After 12 hours, all crystal peaks developed completely and were indexed to be an fcc structure (see Fig.3.13).

Figure 3.13: The scattering intensities of Ludox TM50 at 5mM, $\phi = 0.20$. A symbol * expresses the fcc structure peak appear superimposing on the liquid phase after 11 minutes of nucleation. After 18 hours, the fcc peaks continued growing without the bcc structure peak coexisted.

Meanwhiles, the q-value of fcc did not change over time. Although at this volume fraction the bcc structure can exist according the phase diagram, it was not detected at this volume fraction. This is also true at $\phi = 0.20$ in the interdiffusion samples, the fcc structure existed without the bcc structure. However, the bcc structure may take long time to nucleate or there could be a phase transformation from fcc to bcc that also costs time longer than 18 hours.

Figure 3.14 shows the gradually increasing of a number of the fcc structure at $\phi = 0.20$, the growth was stop after 12 hours in resulting no changing in volume fraction over time. Meanwhile the changing of liquid phase after 12 hours was high. This may cause by a wrong estimation of the liquid peak due to a subtraction of a very sharp power spectrum from the liquid peak. A jumping of volume fractions of the liquid phase in Fig.3.14 was a result of the misleading interpolation of liquid phase curve after a peak subtraction; If the primary peak of a crystal was so high and the crystal-peak base occupied most of the peak area of liquid phase. After the peak subtraction, the liquid phase will lose all of its peak area to the crystal phase. This caused a difficulty to estimate the peak position $q-$value of the liquid phase after the peak subtraction. These jumping volume fractions can be seen also in other results.
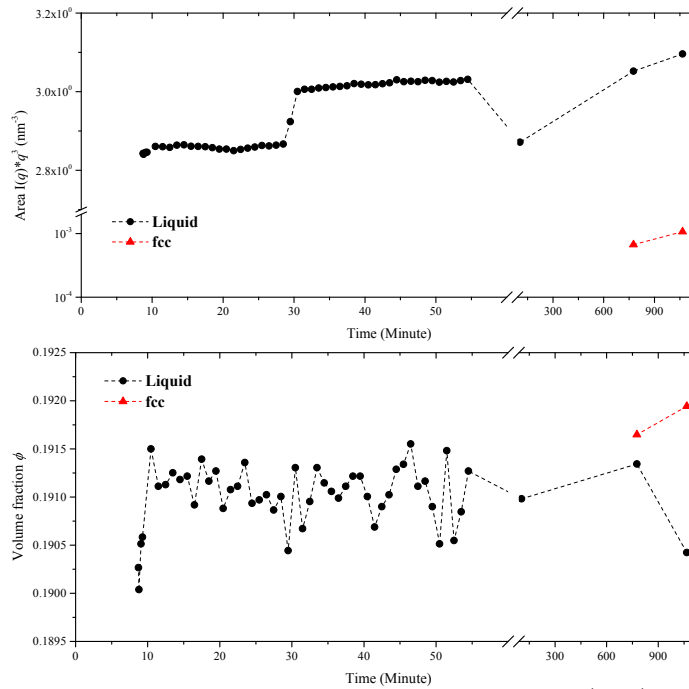
Figure 3.14: The nucleation analysis of TM50 $\phi = 0.20$:(top) The area under the $Iq^2 \cdot q (nm^{-3})$ curve which related to the occupancy of particles in liquid and fcc phases. A number of the fcc structure was increased over time and appeared to stop after 12 hours. (bottom) The evolution of volume fraction over time.

TM50, $\phi = 0.22$: From the phase diagram (see Fig.3.5) at $\phi = 0.22$ is the phase boundary of fcc (ϕ from 0.17 to 0.23) and is the middle of the bcc's favorite place (from $\phi = 0.20$ to 0.25) so that one expects bcc structure rather than the fcc structure. In the kinetics experiment, the bcc structure has appeared since the first observation and continued to grow rapidly. Until by the 25th minute there was no increase in the number of bcc population. Meanwhiles, the fcc structure showed up after 11 hours later in a relatively small amount compared to the bcc structure. At the same volume fraction in interdiffusion samples, only the fcc phase existed with the liquid phase at the beginning, after few weeks of diffusion process the bcc structure has invaded in to this volume fraction.
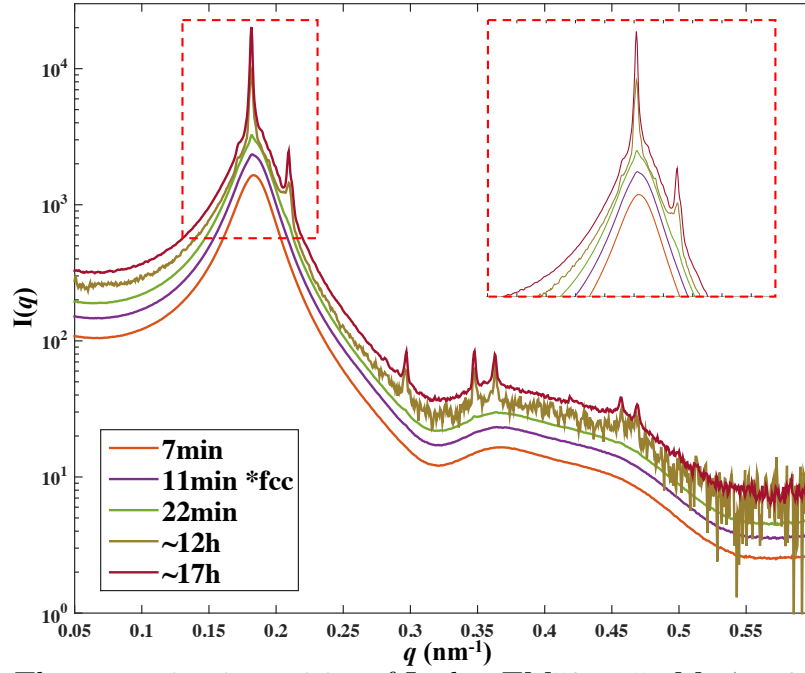
40
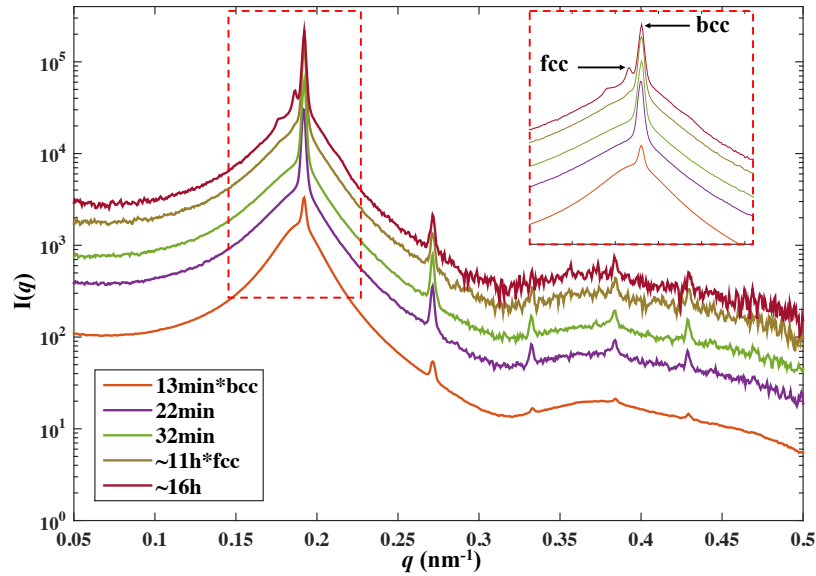
Figure 3.15: The scattering intensities of Ludox TM50 at 5mM, $\phi = 0.22$. The fcc structure peak appear superimposing on the liquid phase after 11 minutes of nucleation.
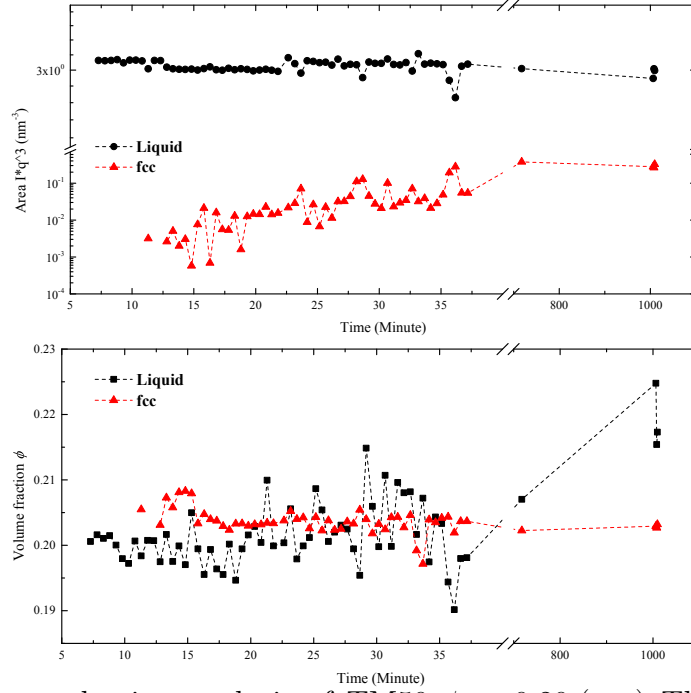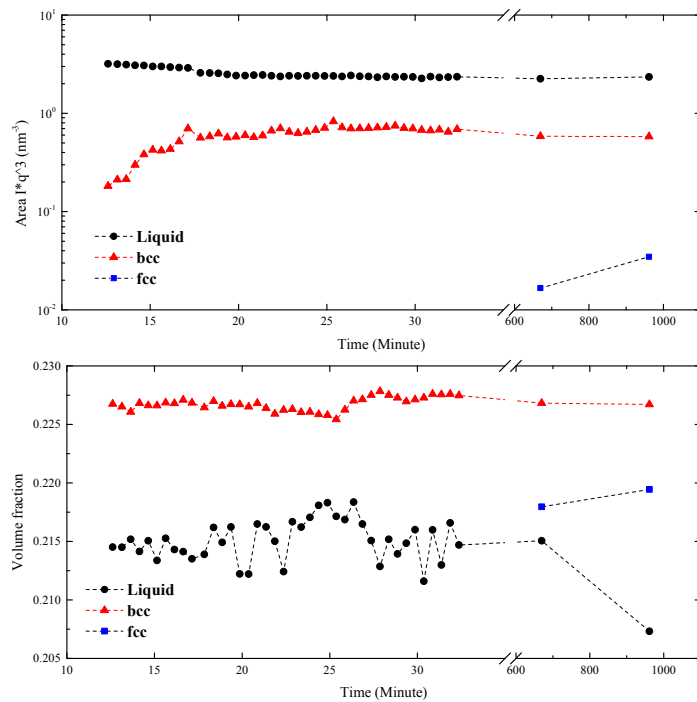

Figure 3.16: The nucleation analysis of TM50 $\phi = 0.22$:(top) The area under the $Iq^2 \cdot q(nm^{-3})$ curve which relate to the occupancy of particles in liquid and fcc phases. (bottom) The evolution of volume fraction over time.

3.2 Ludox HS30 and HS40 colloidal silica

3.2.1 Osmotic pressure curve

Ludox HS30 and HS40 were used as received. They were dialyzed against aqueous solution of PEG (4-8 mg/ml) at NaCl (0.5-50 mM). The volume fraction ϕ and the
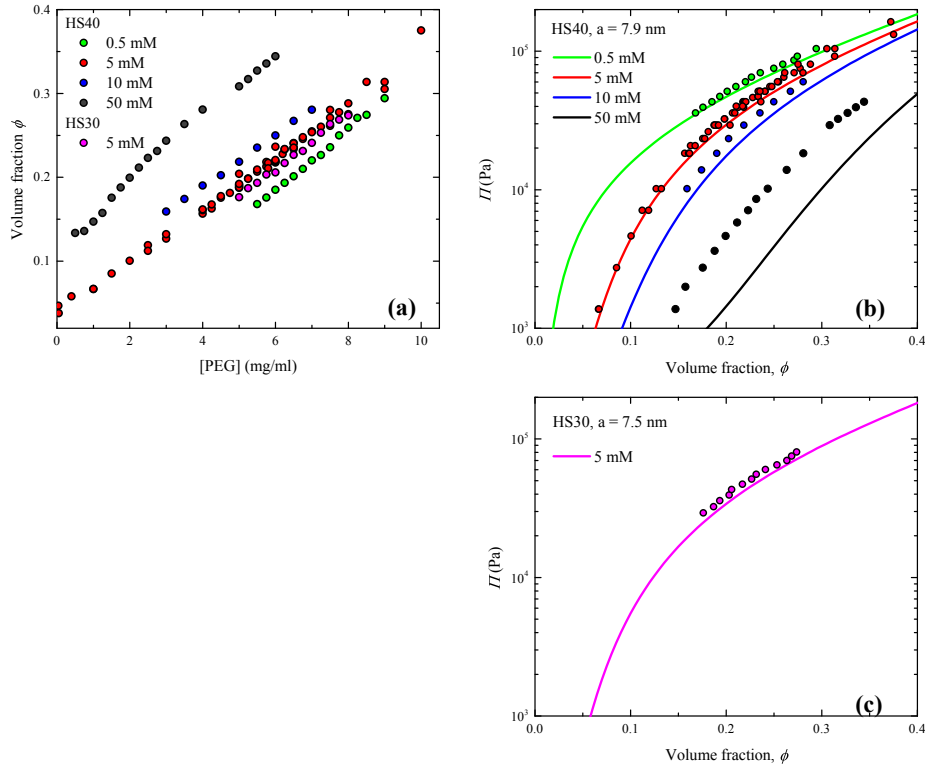
Figure 3.17: Results of dry-extracted volume fractions and the osmotic pressure of dialyzed silica dispersions, Ludox HS30 and HS40 at different concentration of NaCl (0.5-50 mM): (a) Volume fraction of colloidal silica as a function of PEG concentration. (b) Evolution of the osmotic pressure in silica dispersions as a function of the colloidal volume fraction.
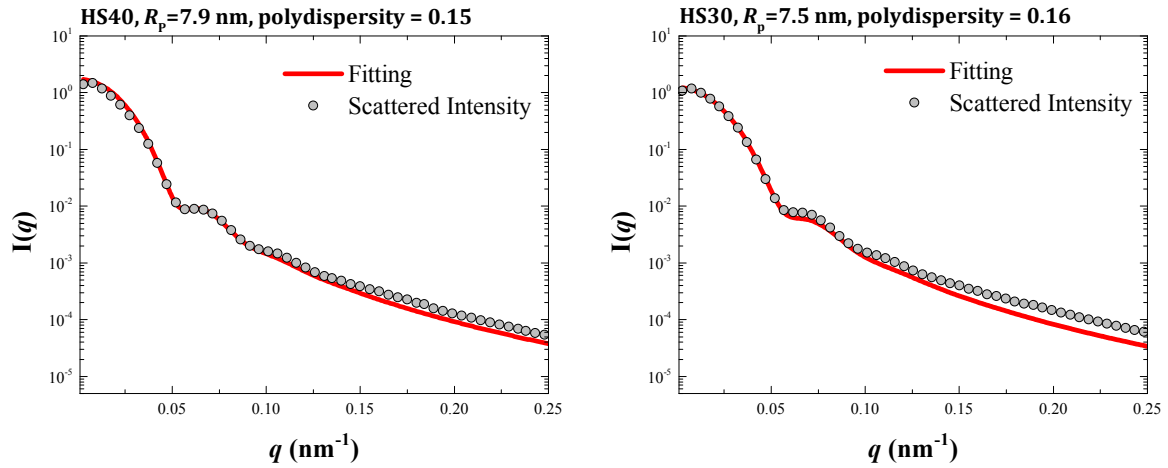
Figure 3.18: Form factors of (a) HS40 ($R_p = 7.9 \pm 0.4\%$ nm, polydispersity $= 15.0 \pm 0.3\%$), and (b) HS30 ($R_p = 7.5 \pm 0.5\%$ nm, polydispersity $= 16.0 \pm 0.2\%$) were estimated by scattered intensity of diluted dispersions, $\phi = 0.001$ (circle) and the theoretical fitting line (red) by $SasView$ software.

osmotic pressure (Π) were measured as described in section 3.1. The volume fraction and the osmotic pressure of Ludox HS30 and HS40 are presented in the Fig. 3.17.

The form factors of Ludox HS30 and HS40 were analyzed through a sample of very
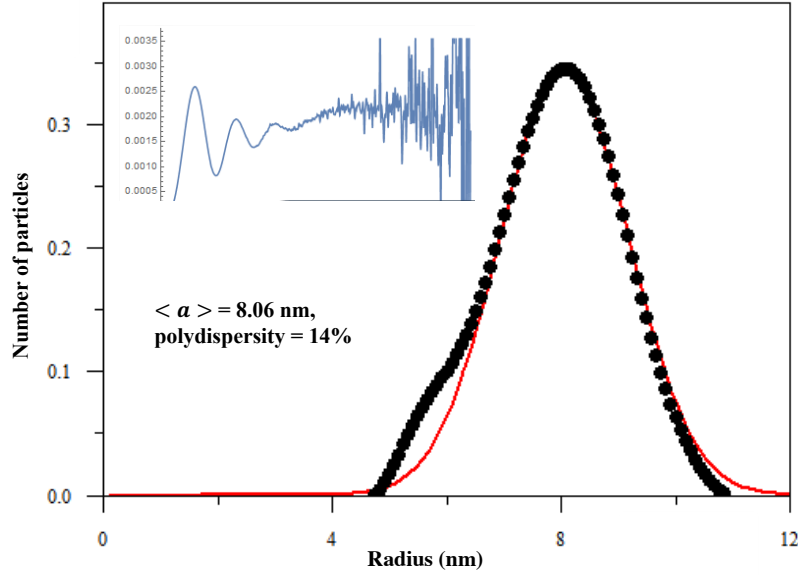
Figure 3.19: The size of Ludox HS40 is fitted by using the inversion formula for SAXS of polydisperse spheres [62]. The fitting size particle of HS40 by Gaussian distribution is 8.06 nm, and polydispersity of 14%. The top left panel is the inversed radius distribution of HS40. (Reproduced with permission from Robert Botet).

diluted dispersions by SAXS experiments. The best-fitted intensity were calculated by $SasView$ [58] using the polydispersity of $15.0 \pm 0.3\%$ and radius of colloidal sphere $R_p = 7.9 \pm 0.4$ nm for HS40 and for HS30 using the polydispersity of $16.0 \pm 0.2\%$ and $R_p = 7.5 \pm 0.5$ nm (see Fig.3.18). Compare the particle size and the polydispersity of HS40, measured by the inversion formula by Botet [62], HS40 had a radius of 8.06 nm and a polydispersity of 14%. Meanwhile, Goerzt et al. [63] reported that HS40 had a diameter of 12-16 nm and polydispersity of 14-18%. Both results of sizes and polydispersity are in good agreement with the measurement from $SasView$. Meanwhile, Ludox HS30 has smaller average size and more polydisperse than Ludox HS40.

3.2.2 Phase diagram

Ludox HS40

The same method as in TM50 (given in section 3.1) is used to identify structures of colloidal crystals in dialyzed samples. For Ludox HS40 (polydispersity of 15%, R_p=7.9 nm) various complex crystal structures were detected and superimposed with the liquid phase. Such complex crystal systems were carefully analyzed by our collaborator, Dr. Franck Artzner, a crystallographer from the University of Rennes. At low
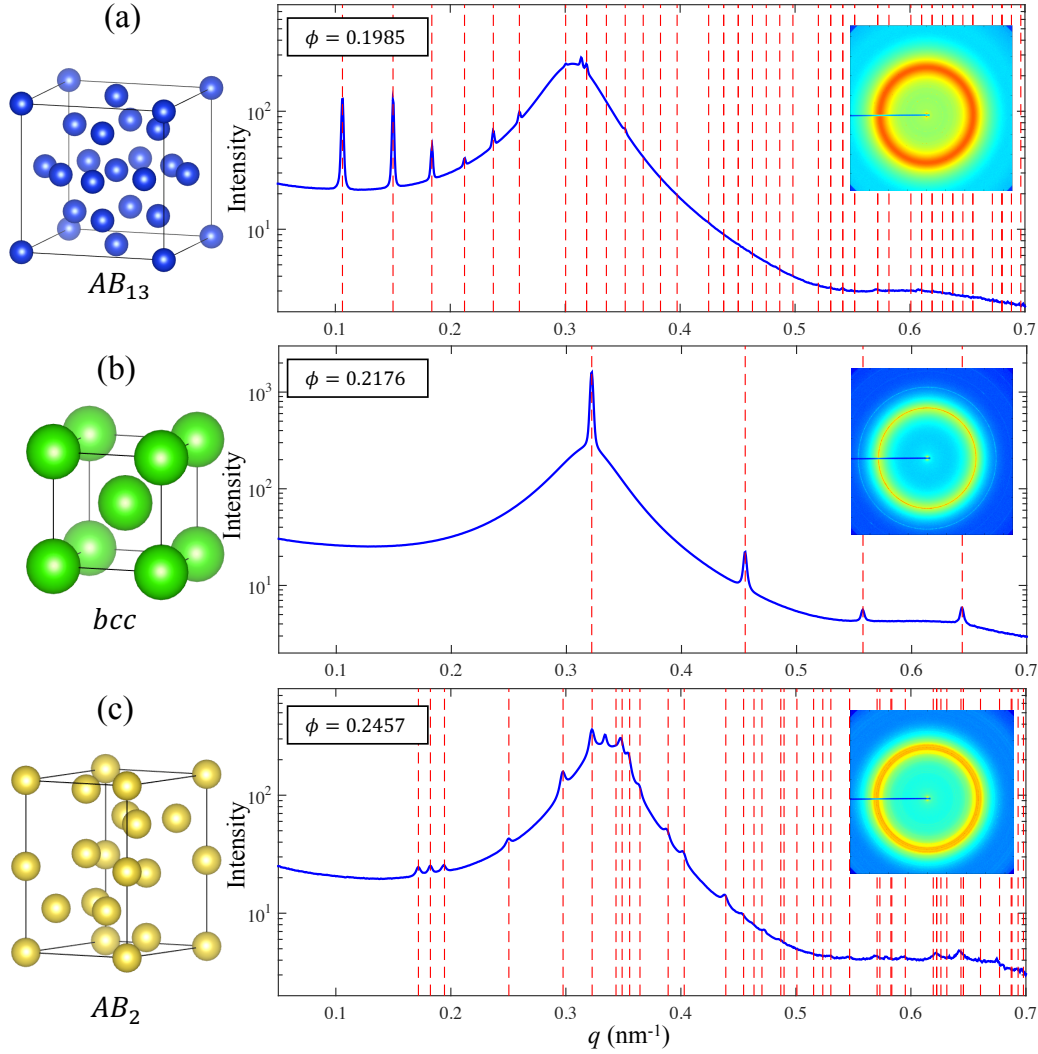
Figure 3.20: Scattering intensities of HS40 samples (blue) and predicted peak positions (q-value) of colloidal crystal structures (red line). (a) At $\phi = 0.1985$, the silica particles form a AB_{13} colloidal crystal with cubic unit cell along with the liquid phase. (b) At $\phi = 0.2176$, the scattering spectra shows peaks of the bcc structure and liquid phase. (c) At higher volume fraction, $\phi = 0.2457$, many shape peaks of a Laves AB_2 appears along with a small peak of the bcc (the middle peak between two red lines) and liquid phase. In all case there is coexisting with a colloidal liquid phase

volume fractions, ϕ, HS40 dispersions has a liquid phase. At higher ϕ, the colloidal particles starts to form a large unit cell crystal of AB_{13} structure, as well as crystals with a body-centered cubic structure (bcc), and Laves AB_2 structure respectively. The scattering spectra of these crystal structures are shown in the Fig. 3.20. Previous work by Cabane et al. [15] also reported of a coexistence of multiple complex crystals (especially bcc and Laves AB_2) in Ludox HS40 (polydispersity of 14%; R_p = 8 nm), but there was no report of AB_{13} structure on their work, and that study focused on identifying colloidal crystals at asingle salt concentration of 5mM NaCl.
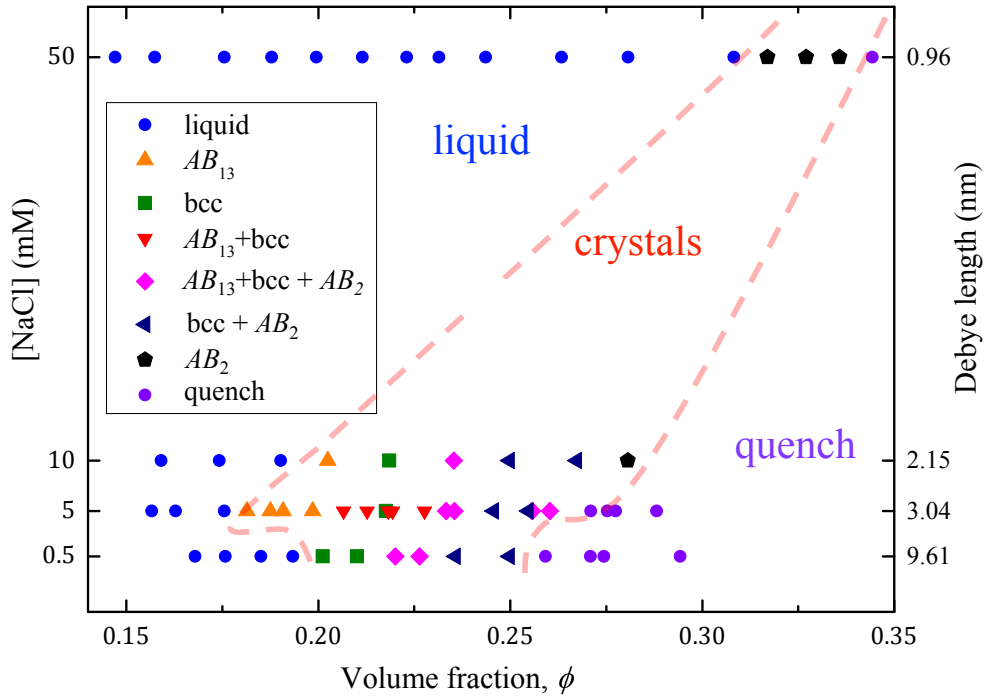
Figure 3.21: A phase diagram of colloidal dispersions Ludox HS40 (polydispersity, 15% ; radius, 7.9 nm) equilibrated at NaCl concentration of 0.5, 5, 10, and 50 mM. The vertical axis presents the salt concentration in mM (on the l.h.s) and the Debye length in nm (on the r.h.s) Symbols express different phases in the phase diagram of HS40. Red dash lines present the estimated phase boundary of crystals

Figure 3.21 presents a phase diagram of Ludox HS40 (polydispersity of 15%, R_p=7.9 nm) at NaCl concentrations of 0.5, 5, 10, and 50 mM. At 5 mM, the populations of silica particles have shown an interesting capability to form complex crystals in the broad range of the volume fraction (typically liquid→AB_{13}→bcc→Laves AB_2→ glass), therefore these samples were repeatedly investigated three times over the periods of 2015-2017, in order to monitor their evolution and stability, and confirm that they presented equilibrium phases . Figure 3.22 shows an evolution of the HS40 phase diagrams at 5 mM from 2015 to 2017.

The first investigation of HS40 samples at 5mM was performed in 2015, the results showed that at volume fraction $\phi = 0.18$ to 0.28 were an appropriate environment which allowed a AB_{13} crystal structure to be formed. The bcc phase and Laves AB_2 structure were arranged from $\phi = 0.20$ to 0.28 and $\phi = 0.23$ to 0.28 respectively. In 2016 these set of samples were sent for investigating with SAXS by our collaborator Michael Stzucki at ESRF, France. The results showed that the bcc phase was forming at slightly lower ϕ. This could be a result of a settling of a large unit cell crystal at
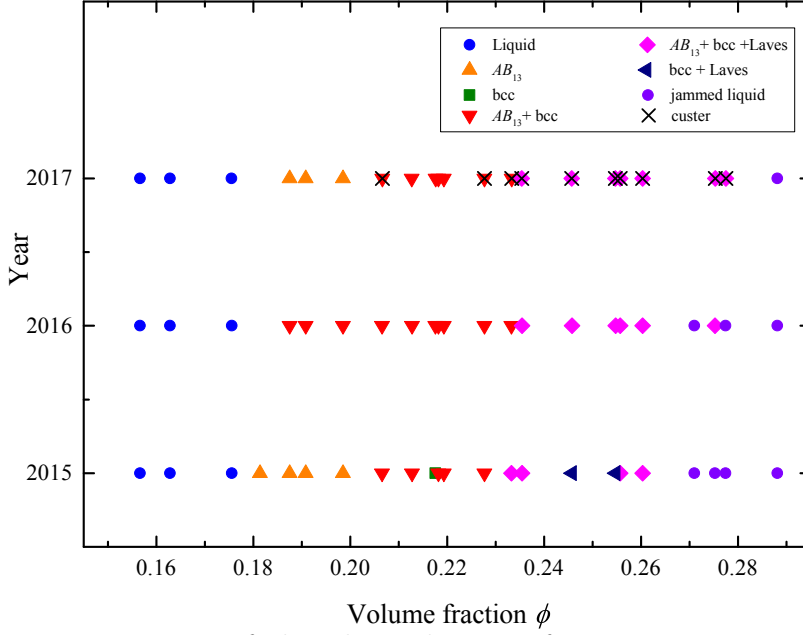
Figure 3.22: Measurements of the phase diagram from 2015 - 2017, showing only relatively minor difference in structure, seen, in HS40 equilibrated at 5mM NaCl.

the bottom of capillary after being kept for a long time, causing an inhomogeneous of volume fraction in a capillary. This allow particles, which are in liquid phase, to form a smaller structure (bcc) at the top of dispersions. Two samples were damaged during the transport (seen as missing points on the phase diagram in the Fig. 3.22). The third investigation was performed by me. Since crystals of HS40 are different in sizes and densities, when samples are aligned vertically for a SAXS scanning, the settling of large crystals at the bottom of samples may cause an nucleation of a small crystal structure. To avoid this, we aligned samples in horizontal and scanned across them from the left to the right and averaging the scattered intensities of each sample. Indeed, we found a large unit cell of AB_{13} structure at the same volume fraction range as in the first investigation. Moreover a new large structure was observed at a low q-value of 0.074 - 0.082 and an preliminary analysis by Dr. Artzner suggested that it is a colloidal crystal with the structure of carbon cluster C_{24}. However, the structure of the new crystal is not conclusive at this time (see Fig. 3.23).

The volume fraction ϕ - q^3 calibration curve of Ludox HS30 is showed in the Fig.3.24. One can compare unit cell size of crystal phases in HS40 due to $\alpha \propto R_p^3$, so that one obtains that Ab_{13} and AB_2 structures are five and two times the size of the bcc structure respectively.
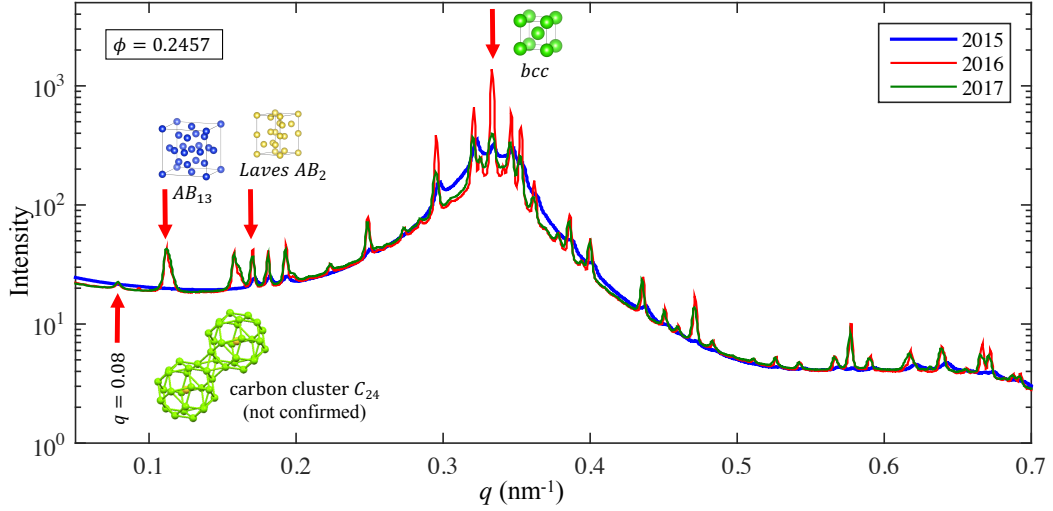
Figure 3.23: Evolution during 2015-2017 of the scattered intensity of HS40 at 5mM, $\phi = 0.2475$. In 2015, the sample contained the crystal structure of Laves AB_2 and bcc. In 2016, the larger structure AB_{13} structure has been formed and indexed. The primary peak position of each crystal phase was labeled with a red arrow; at a very low q-value $= 0.08$, small peaks were also seen which can be indexed as a large carbon cluster C_{24}. Other primary peak positions were indexed at $q = 0.11$, 0.17, 0.33 for the AB_{13}, the Laves AB_2, and the bcc structure respectively.
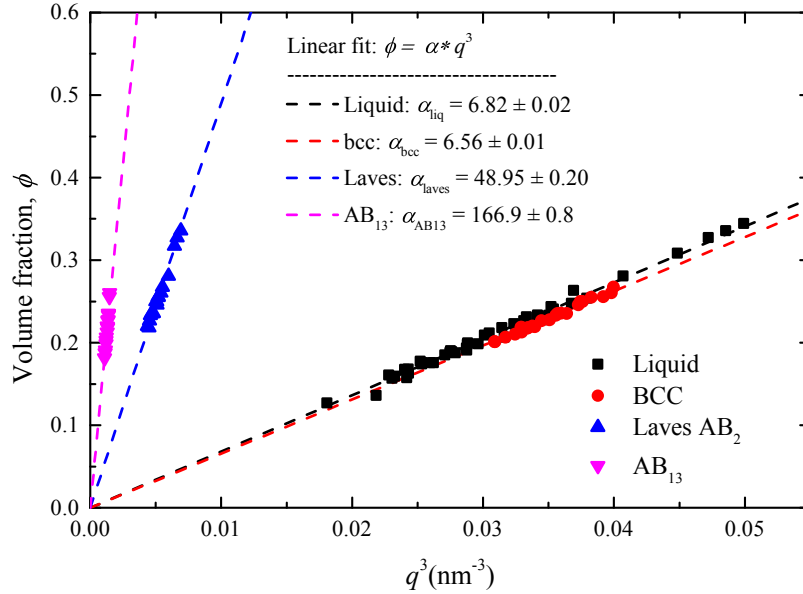
Figure 3.24: A calibration curve of q_{1st}^3 in nm^{-3} vs volume fraction ϕ for Ludox HS40.

Ludox HS30

There are two grades HS Ludox samples, classified by silica concentration 40% (HS40) and 30% (HS30). In this part, I prepared a set of dialyzed samples of Ludox HS30 ($R_p = 7.5 \pm 0.5$ nm, polydispersity; $15.0 \pm 0.3\%$) in order to compare a phase diagram from HS30 and HS40. Results of the form factor analysis shows that the
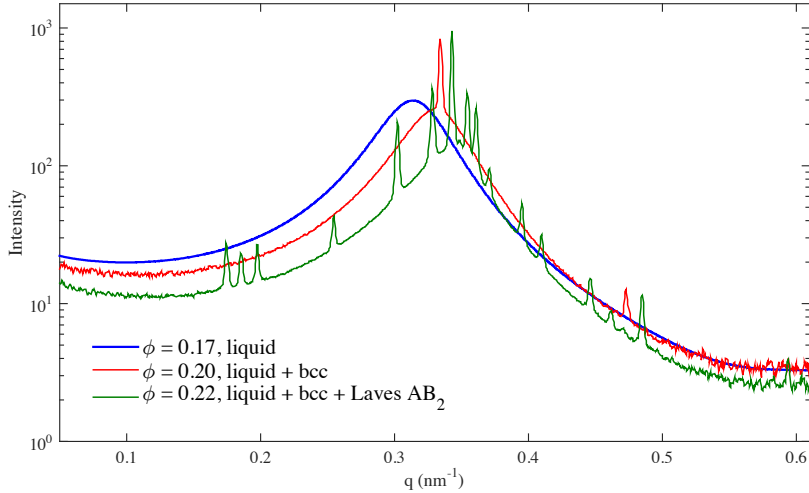
Figure 3.25: Scattering intensities of HS30 samples; at $\phi = 0.17$, colloidal particles were in liquid phase (blue). At $\phi = 0.20$, the bcc structure appeared together with the liquid phase (red). At $\phi = 0.22$, the Laves AB_2 also appeared along with the liquid and the bcc structure (green).

Ludox HS30 and HS40 have slightly different in size and polydispersity (see Fig.3.18). Therefore, HS30 samples were dialyzed against NaCl solution at 5mM as a comparative sample set of HS40. A set of Ludox HS30 samples was concentrated with volume fraction ϕ between 0.17 to 0.28 depending on the concentration of PEG. The scattering pattern of the liquid phase and crystal structures were extracted to create a phase diagram of HS30. The preliminary analysis of a phase diagram of Ludox HS30 showed that at low volume fraction the population of colloidal silica had a liquid phase as expected. When the volume fraction was increased, the scattering pattern of crystals appeared and were indexed as bcc and Laves AB_2 structures, without the AB_{13} structure (see Fig. 3.25). Figure 3.26 represented the evolution of Ludox HS30 phase diagram at 5mM NaCl which was analyzed by SAXS data. Due to access limitations of the synchrotron radiation facility, the dialyzed HS30 samples were only re-investigated in 2017 by SAXS. The results of crystal phase investigations after a period of time showed that HS30 particles also started to form a large complex structure. This structure was indexed as a AB_{13} structure and had a sequence of scattering peaks similar to AB_{13} structure that appeared in Ludox HS40. However, the larger and more complex C_{24} phase was not found in Ludox HS30 samples.
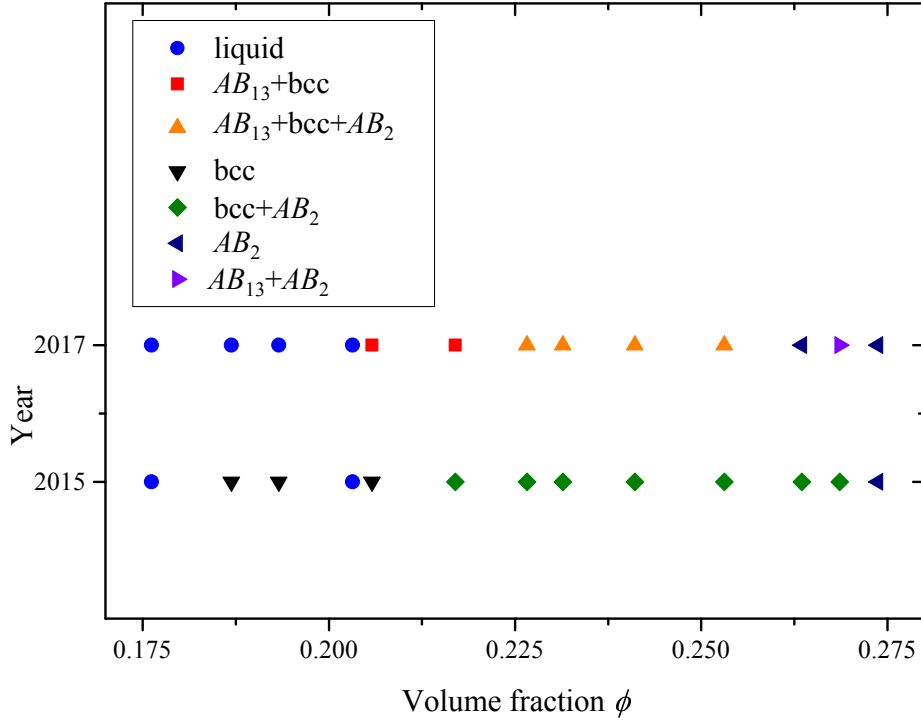
Figure 3.26: A phase diagram of Ludox HS30 showing development between 2015 to 2017.

3.2.3 Interdiffusion experiments

Three interdiffusion samples were prepared as described in section 3.1.3 using two different volume fractions of Ludox HS40 at 5 mM NaCl which the lower one was in the liquid phase ($\phi = 0.17$) and the higher one was in a glass phase ($\phi = 0.29$). Two samples thus inter-diffused spend 12, 19, and 26 days forming crystals, volume fractions were characterized through SAXS scattering intensities, q-value of liquid phase and peaks of crystals were then converted into a volume fraction ϕ using a calibration curve of Ludox HS40 (see Fig. 3.24). The diffusion of particles in a capillary were predicted by equation 3.5. Each sample were scanned with the interval of 0.5 mm along its length. In the volume fraction range of 0.17 to 0.29 of HS40 at 5mM, one expects to see all crystal types in the HS40 phase diagram: the bcc structure at $\phi =$0.21 to 0.26, the AB_2 structure at $\phi = 0.23$ to 0.26, and the AB_{13} structure at $\phi = 0.18$ to 0.27. As the diffusion process ends, the final volume fraction should be $\phi = 0.23$ where all types of crystals in the HS40 phase diagram can be appear.

49
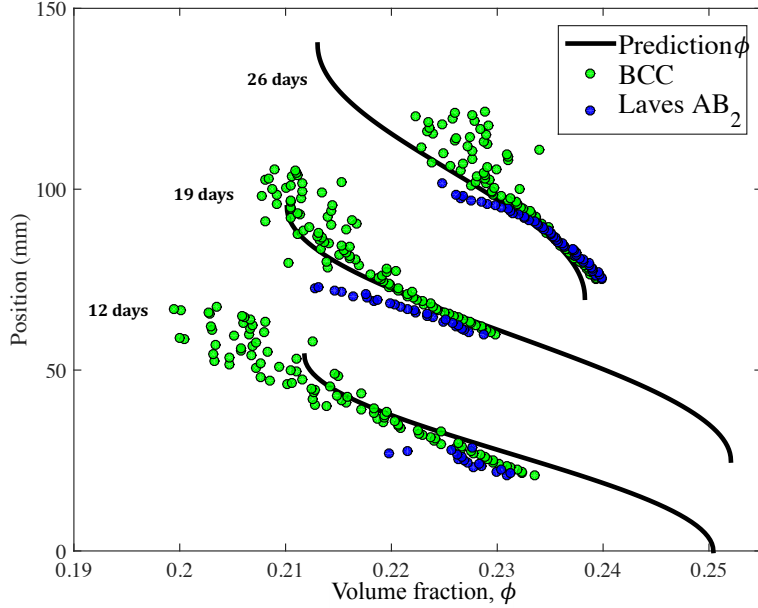
Figure 3.27: Interdiffusion experiment on colloidal dispersions Ludox HS40 (initial volume fraction ϕ of 0.17 and 0.29). The vertical axis is the length in mm. The volume fraction of dispersions in the capillary are converted from bcc peaks (green) and Laves AB_2 peaks (blue). The volume fraction (solid line) is predicted by the interdiffusion model (equation 3.5) with the dimensionless diffusivity $\tilde{D} = 15$.

Figure 3.27 shows the results of the interdiffusion experiment with the corresponding predictions of volume fractions. Due to a limitation of a sample alignment based on the sample holder design, we were unable to explore samples in an entire length. However, we attempted to collect SAXS data as much as possible from each sample. After few days of diffusion, the HS40 colloidal particles in capillaries stared to form a bcc structure at the lower ϕ and a Laves AB_2 at the higher ϕ. The bcc structure was detected at every scanning positions in the capillaries, as expected. The Laves AB_2 began to appear at $\phi = 0.21$, where the volume fraction is lower than that appears in the HS40 phase diagram. There was no signal of AB_{13} structure in all three samples, although the AB_{13} structure is found in a broad range of Ludox HS40 colloidal systems. The AB_{13} may take a longer time to form or after the diffusion is finish. (see HS40 phase diagram in Fig.3.21). After 26 days, particles were still in the bcc and AB_2.

3.2.4 Crystal nucleation and growth

In this part, we investigated the kinetics of crystal nucleation and growth of Ludox HS40 by direct observation (as described in Ludox TM50) over about 24 hours. Since the phase diagram of Ludox HS40 showed that at 5mM NaCl the crystal structures appeared over the volume fraction $\phi = 0.19$ to 0.27 (see Fig.3.21). Therefore, we prepared four samples as fresh by diluting a concentrated solution of Ludox HS40, $\phi = 0.29$, to the volume fractions of 0.19, 0.21, 0.23, and 0.24. All sample were immediately analyzed through SAXS after dilution and scanned repeatedly over the 24 hours following their nucleation. The q-value of the liquid and crystal peaks were obtained from radial grouping of SAXS 2D-image and converted to a volume fraction by the calibration curve in Fig. 3.24. According to the phase diagram of HS40 at 5mM NaCl, the bcc structure phase appears at $\phi = 0.21$ to 0.26, the AB_2 at $\phi = 0.23$ to 0.26, and the AB_{13} at $\phi = 0.18$ to 0.27, one expects to see at least one crystal structure in all samples.

HS40, $\phi = 0.19$: From Ludox HS40 phase diagram at 5 mM NaCl (see Fig.3.21), at $\phi = 0.19$ the particles in dispersions should organize in the liquid and AB_{13} phases. In the kinetics experiments, a sample volume fraction $\phi = 0.19$, particles remained in the liquid phase; although even ten hours after the preparation the nucleation was still not seen (see Fig.3.28). The AB_{13} structure may take more time to crystallize at this volume fraction.

Figure 3.29 shows a coverted volume fraction from the q value of the liquid phase without the existence of a crystal structure. Although the average volume fraction liquid phase is $\phi = 0.187$, where expected AB_{13} to appear, no crystal nucleation is seen.

HS40, $\phi = 0.21$: From the phase diagram of Ludox HS40 at 5 mM NaCl (see Fig.3.21), at $\phi = 0.21$ the particles in dispersions should organize into the liquid, the AB_{13}, or the bcc phases. The kinetics experiment at $\phi = 21$ (see Fig.3.30), a nucleation of the bcc structure was observed and continued growing rapidly. About 40 minutes after the preparation the nucleation was stop, and remained in the bcc phase without coexistence of the AB_{13} structure. This suggests that AB_{13} is slow to appear at this volume fraction. The average converted volume fraction was measured as $\phi = 0.205$ (see Fig3.31).
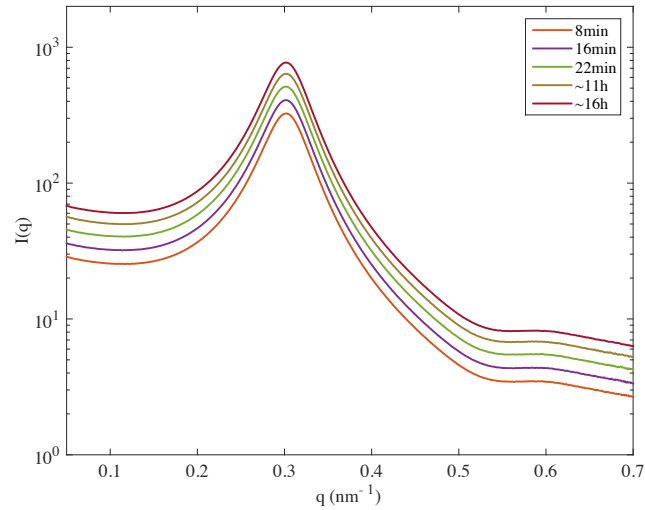
Figure 3.28: The scattering intensities of Ludox HS40 at 5 mM NaCl, $\phi = 0.19$. The particles maintained in the liquid phase. Note that curves are shifted up along y-axis for clarity
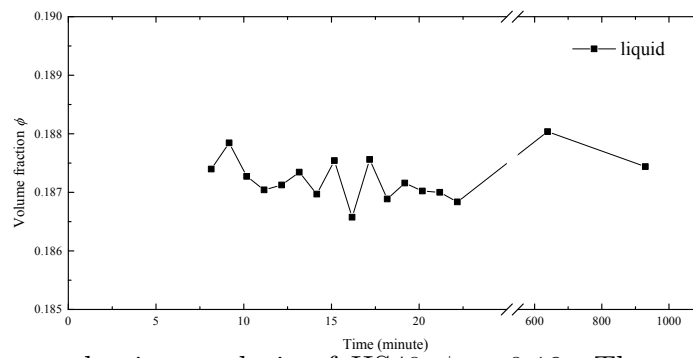
Figure 3.29: The nucleation analysis of HS40 $\phi = 0.19$: The evolution of volume fraction over time.

Figure 3.30: The scattering intensities of Ludox HS40 at 5 mM NaCl, $\phi = 0.21$. The bcc structure peaks appeared superimposing on the liquid peak.

52

Figure 3.31: The nucleation analysis of HS40 $\phi = 0.21$: (top) The area under the $Iq^2 \cdot q(nm^{-3})$ curve which relate to the occupancy of particles in the liquid and the bcc phase. (bottom) The evolution of volume fraction over time.

HS40, $\phi = 0.23$: From the phase diagram of Ludox HS40 phase diagram at 5 mM NaCl (see Fig.3.21), at $\phi = 0.23$ is expected to see particles in all phases. The kinetics experiment at $\phi = 0.23$ (see Fig.3.32), the bcc structure appeared with sharp peaks and, eventually, it remained in the bcc phase. The average converted volume fraction remained at $\phi \approx 0.228$ (see Fig.3.33). The AB_{13} and AB_2 may be slow to crystallize at this volume fraction, they may crystallize after 15 hours.

HS40, $\phi = 0.24$: From the Ludox HS40 phase diagram at 5 mM NaCl (see Fig.3.21), at $\phi = 0.24$, the liquid, AB_{13}, bcc, and Laves AB_2 phase are expected to crystallize at this volume fraction. Also, this volume fraction is the phase boundary of AB_2 structure to appear. The kinetic experiment at $\phi = 0.24$, only the bcc structure is observed to grow rapidly. After eight hours, the disperse particles still remained in liquid and bcc phase. Meanwhile the AB_{13} and AB_2 structures still did not appear. The time scale of AB_{13} and AB_2 of HS40 populations to crystallize may take longer time than that used in this experiments. However, they are good evidences of fractional crystallization among the polydisperse population of HS40.

53
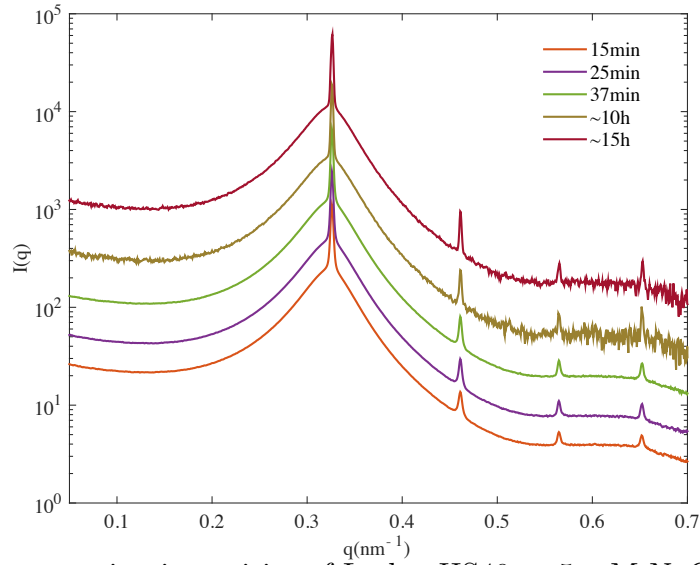
Figure 3.32: The scattering intensities of Ludox HS40 at 5 mM NaCl, $\phi = 0.23$. The bcc structure peaks appeared superimposing on the liquid peak.
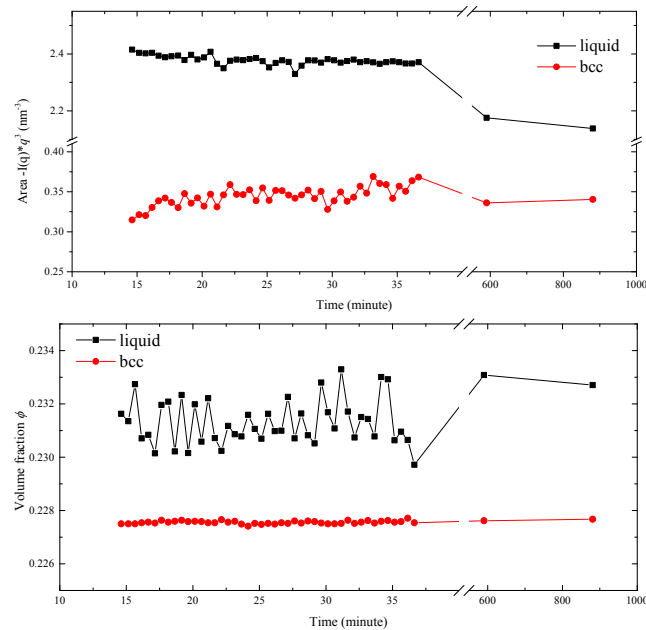
Figure 3.33: The nucleation analysis of HS40 $\phi = 0.23$: (top) The area under the $Iq^2 \cdot q(nm^{-3})$ curve which relate to the occupancy of particles in liquid and bcc phase. (bottom) The evolution of volume fraction over time.
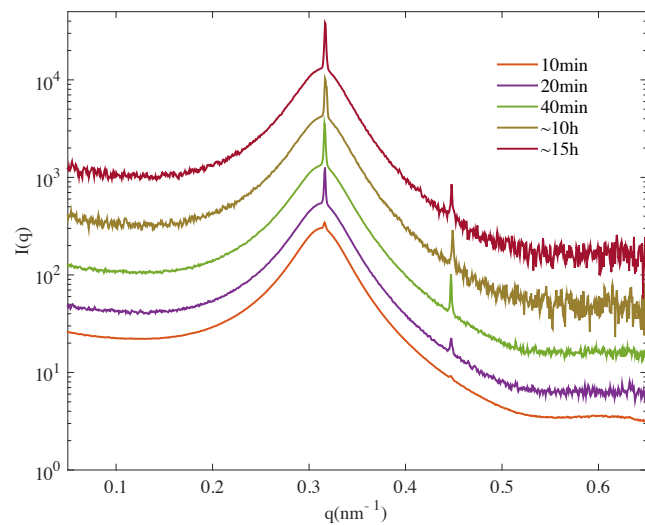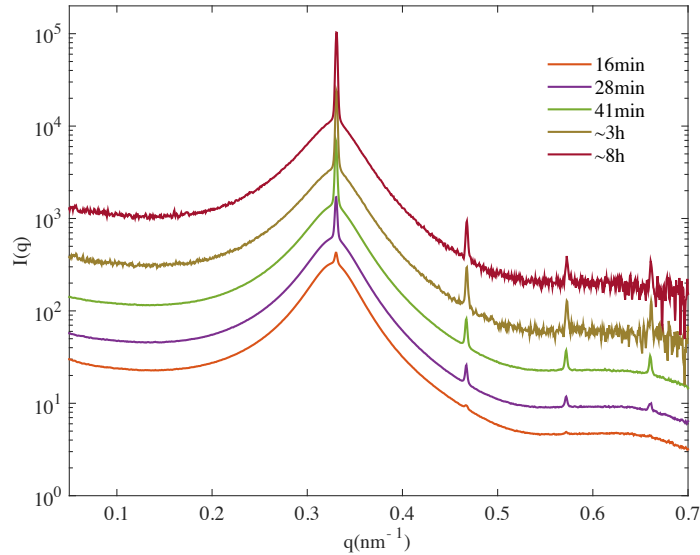
Figure 3.34: The scattering intensities of Ludox HS40 at 5 mM NaCl, $\phi = 0.24$. The bcc structure peaks appeared superimposing on the liquid peak.
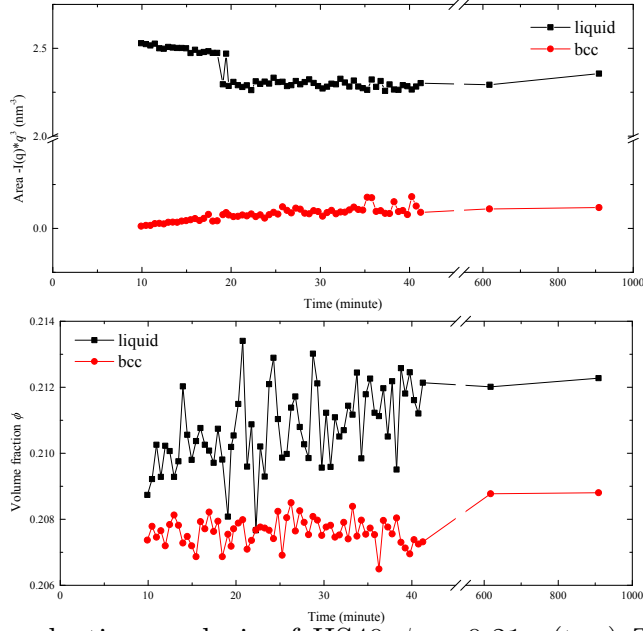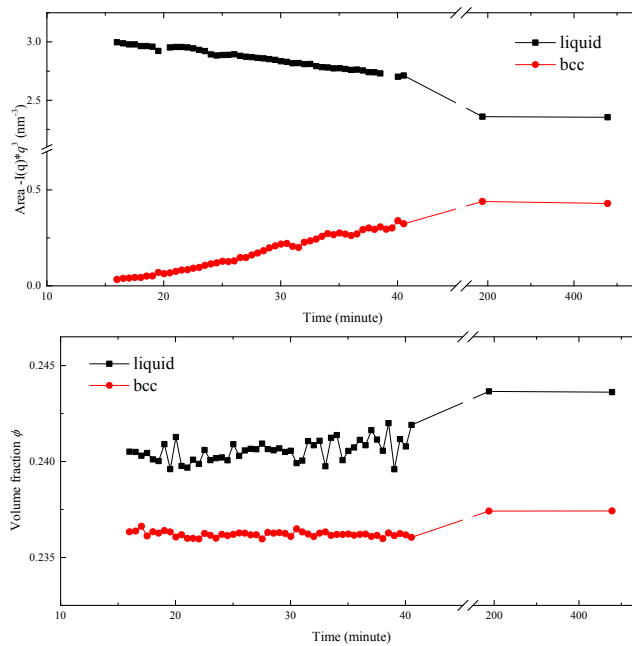

Figure 3.35: The nucleation analysis of HS40 $\phi = 0.24$: (top) The area under the $Iq^2 \cdot q(nm^{-3})$ curve which relate to the occupancy of particles in liquid and bcc phases. (bottom) The evolution of volume fraction over time.

3.3 Ludox SM colloidal silica

The same method, as described in TM50 is giving in section 3.1, were used to identify structures of colloidal crystals in dialyzed samples. The Ludox SM30 (polydispersity of $19.2 \pm 0.5\%$, and $R_p = 4.8 \pm 0.3$ nm) was used as received. Dialyzed samples
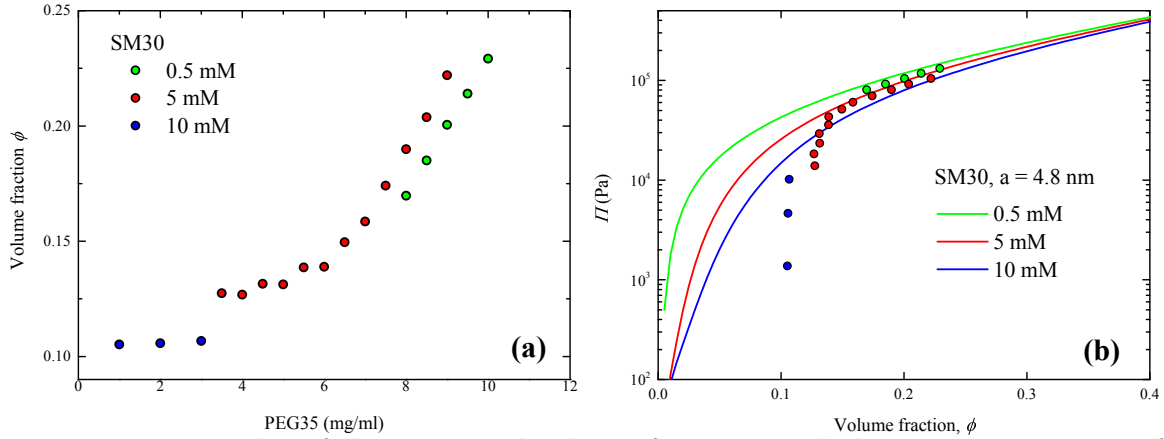
Figure 3.36: Results of dry-extracted volume fractions and the osmotic pressure of dialyzed silica dispersions (Ludox SM30) at 0.5 to 10 mM Nacl: (a) Volume fraction of colloidal silica as a function of PEG concentration. (b) The evolution of the osmotic pressure in silica dispersion as a function of the colloidal volume fraction

were prepared by dialyzing against aqueous solution of PEG at NaCl (pH= 9-10). According to the particle size of Ludox SM30, they were the smallest particle size in this work, we found a difficulty during the dialysis process. At high concentrations of PEG (5 to 6 mg/ml), some dialyzed samples were inhomogeneous; the dispersions aggregated on the inner wall of the dialysis bag resulting the dispersions were a high viscous liquid and inhomogeneous in density and the volume fraction. Therefore, only the inner part of these samples was taken and measured its volume fraction. The volume fraction and the osmotic pressure (Π) of Ludox SM30 samples were measured and calculated as described in section 3.1.

Figure 3.36 presented the measured volume fractions and the osmotic pressure of dialyzed samples of SM30. At high salt concentration, 10 mM, the samples may not reach the equilibrium due to the aggregation occurred during the dialysis. At 5mM, some sample at low volume fraction showed obviously that they did not reach the equilibrium. In fact, these samples were prepared hastily due to the limitation of time. These may a reason why samples did not reach the equilibrium when harvesting. Meanwhile at higher volume fraction samples, which was prepared earlier, agreed well with the osmotic pressure curve.

The form factor of SM30 was analyzed through a sample of very diluted dispersions by SAXS (see figure 3.37). The a best-fitting form factor of Ludox SM30 was simulated by *SasView* software. The result shows that silica particles of SM30 had a small radius and a high polydispersity (radius 4.8 ± 0.3 nm, polydispersity of $19.2 \pm 0.5\%$).
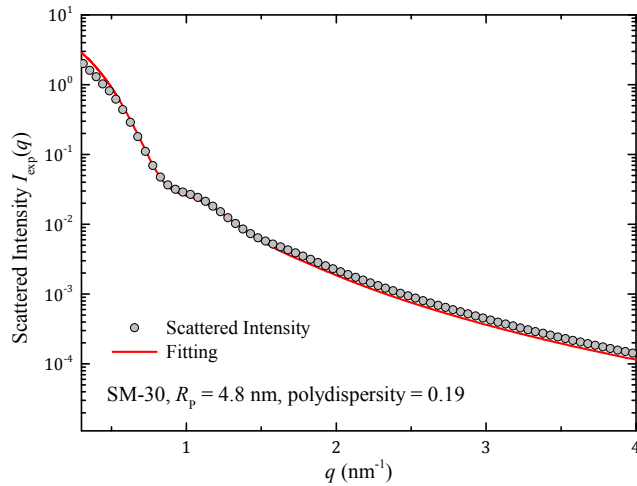
Figure 3.37: The form factor of SM30 was estimated by the scattered intensity of a diluted dispersions, $\phi = 0.1$ (grey circles) and the theoretical fitting line (red) by *SasView* software. The results shows Ludox SM30 has a particle radius of 4.8 ± 0.3 nm and polydispersity of $19.2 \pm 0.5\%$
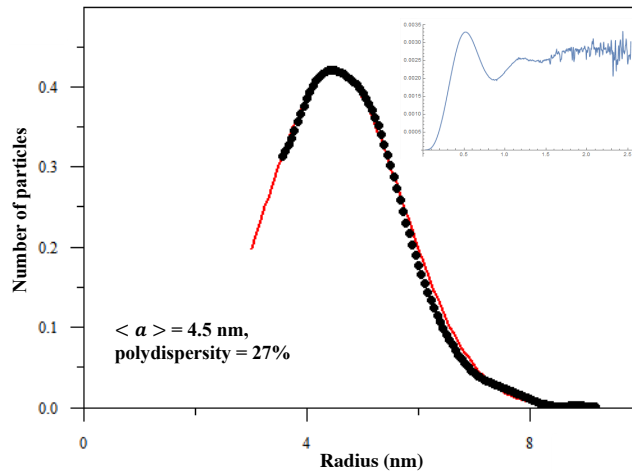
Figure 3.38: The size distribution of Ludox SM30 is fitted by using the inversion formula for SAXS of polydisperse sphere [62]. The fitting size particle of SM30 by Guassian distribution is 4.5 nm and polydispersity of 27%. The top panel if the inversed radius distribution of SM30 (Reproduced with permission from Robert Botet).

Meanwhile the particle size measured by the inversion formula for SAXS obtained the particle radius of 4.5 nm and the polydispersity of 27%. The polydispersity of SM30 is quite high. After the dialysis, samples that were equilibrated at high PEG concentration became hard solids such that they were not able to be injected in a capillary. Therefore, only aqueous samples were investigated thought SAXS. The scattering intensities of all Ludox SM30 samples behaved as liquid phase (see Fig.3.39).

Sine all samples of SM30 did not crystallize, their phase diagram was not studied. However, some dialyzed samples of Ludox SM30 were used for the drying colloids in
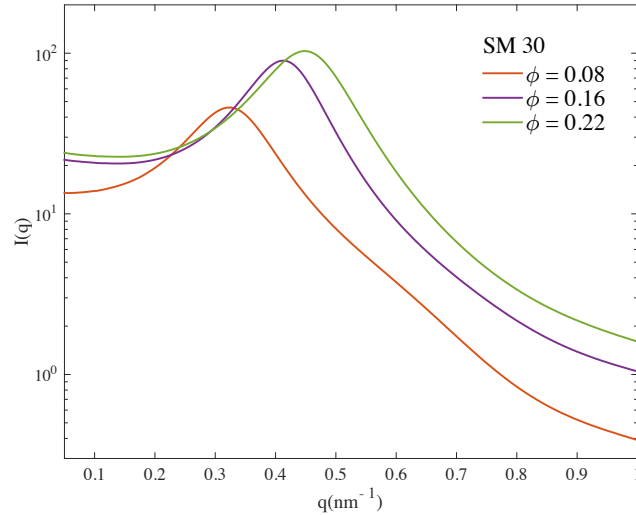
Figure 3.39: Scattering intensities of SM30 at different volume fractions shows that particles are in the liquid phase.

Hele-Shaw cell experiment which is presented in the chapter 4.

3.4 Levasil colloidal silica

3.4.1 Osmotic pressure curve

Levasil collodial sillica (AkzoNobel) were used as sources for the dialysis. There were two grades Levasil samples: classified by silica concentration Levasil30 (30 wt%) and Levasil50 (50 wt%). A set of Levasil30 and Levasil50 colloidal dispersions were dialyzed against aqueous solution of PEG (0.5 to 1.5 mg/ml) at NaCl 0.5 mM to obtain the volume fraction range of 0.15 to 0.45%. Since the received Levasil colloidal silica were high concentrated, a set of diluted Levasil (1:1 dilution) were prepared and dialyzed with the same procedure as non-diluted samples. The volume fraction ϕ and the osmotic pressure were measured as described above in section 3.1. The volume fraction and the osmotic pressure of Levasil30 and Levasil50 were presented in Fig.3.40. The predicted osmotic pressure are lower than the experimental data in all case. However, colloidal particles of Levasil30 crystallized and due to their size are quite large, considered as a good light reflector, they were used in the drying and cracking experiments.
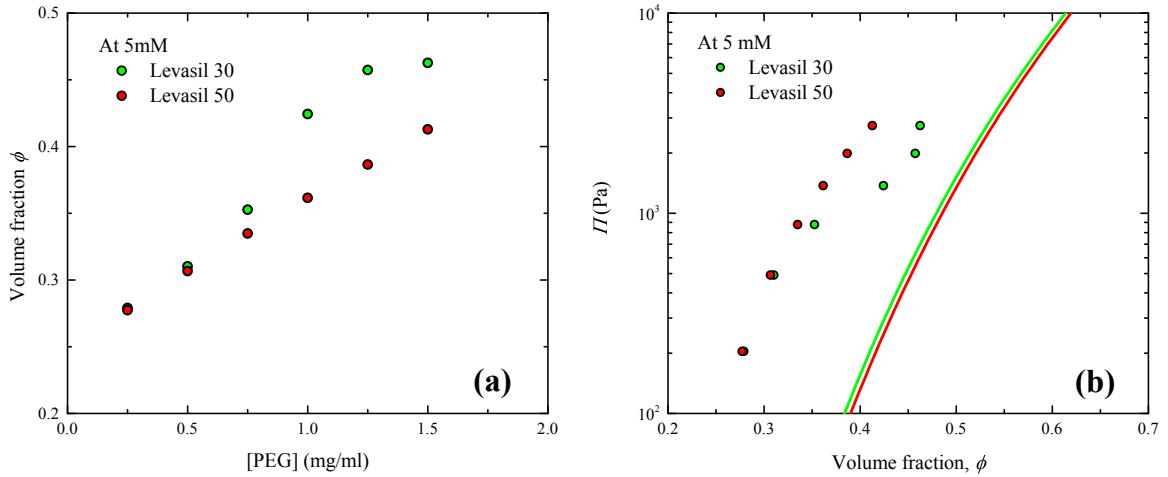
Figure 3.40: Results of dry-extracted volume fraction and the osmotic pressure of dialyzed silica dispersions, Levasil30 and Levasil50, at 0.5 NaCl: (a) Volume fraction ϕ of Levasil silica as a function of PEG concentration. (b) Evolution of the osmotic pressure in equilibrated silica dispersions as a function of the volume fraction.

Form factors of Levasil30 and Levasil50 were quantified through SAXS by a very diluted dispersions (ϕ =0.1) and their best fitting form factors were obtained by *SasView* software [58]. Figure 3.41, the form factor of Levasil30 showed a perfect shape of a sphere with a radius of 48 ± 2 nm and polydispersity $11 \pm 3\%$, meanwhile the form factor of Levasil50 was effected by a high polydispersity of $36 \pm 4\%$ and a radius of 49 ± 3 nm.
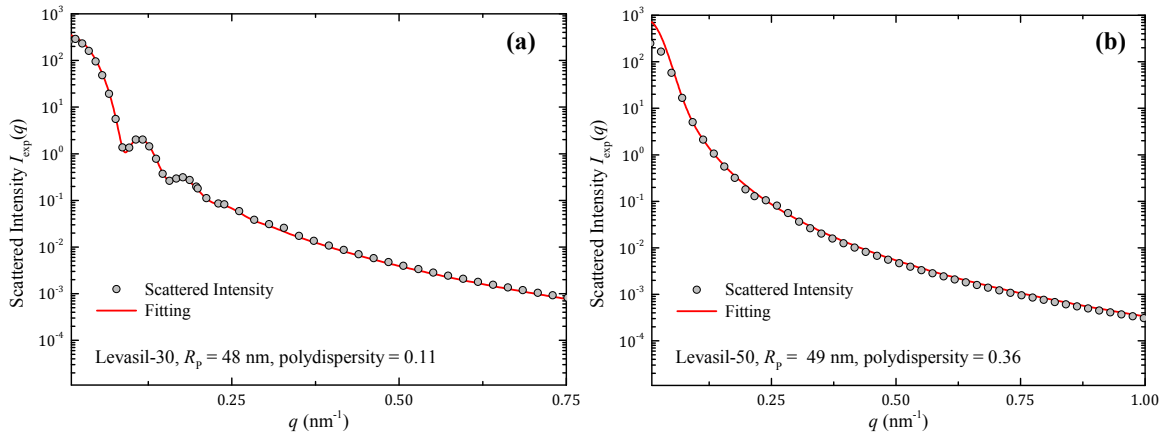
Figure 3.41: Form factors of Levasil colloidal dispersions: (a) Levasil30, $R_p = 48 \pm 2$nm and polydispersity $11 \pm 3\%$, and (b) Levasil50, $R_p = 49 \pm 3$ nm and polydispersity $36 \pm 4\%$, were estimated from a diluted dispersions, ϕ =0.1 (circle), and(red) and measured by *SasView* [58]

.

3.4.2   Phase diagram

Levasil30

We used the same method as in TM50 (giving in section 3.1) to identify structure of colloidal crystals dialyzed samples. A set of dialyzed Levasil30 samples at 5.0 mM Nacl (ϕ of 0.15 to 0.47) were analyzed through SAXS technique. Samples were analyzed in 2015 and were re-analyzed as a follow-up experiments in 2016. The first SAXS experiment, an fcc crystal structure was observed in on sample at $\phi = 0.31$ (at this volume fraction was determined for the growth and nucleation study for Levasil30). The second SAXS experiment showed a interesting results, at $\phi = 0.31$ the crystal collapse into the liquid phase without a changing shape and q-peak position. Levasil30 particles formed an fcc crystal structure at $\phi = 0.35$ where they managed to be in the liquid phase on the first investigation (see Fig.3.42). We measured the primary q-values of both the liquid and the fcc crystal phases creating a phase diagram of Levasil30 (see Fig.3.43) and a calibration curve for Levasil30 (see Fig.3.44).
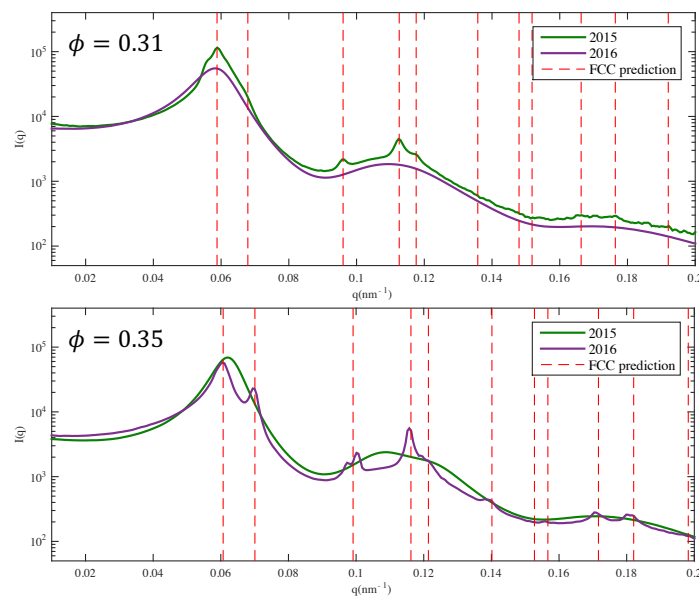
Figure 3.42: SAXS results of dialyzed colloidal samples of Levasil30 in 2015(green) compares with in 2016 (purple). Levasil30 samples were indexed a fcc structure at $\phi =$ 0.31 of 2015 and at $\phi =$ 0.35 of 2016.
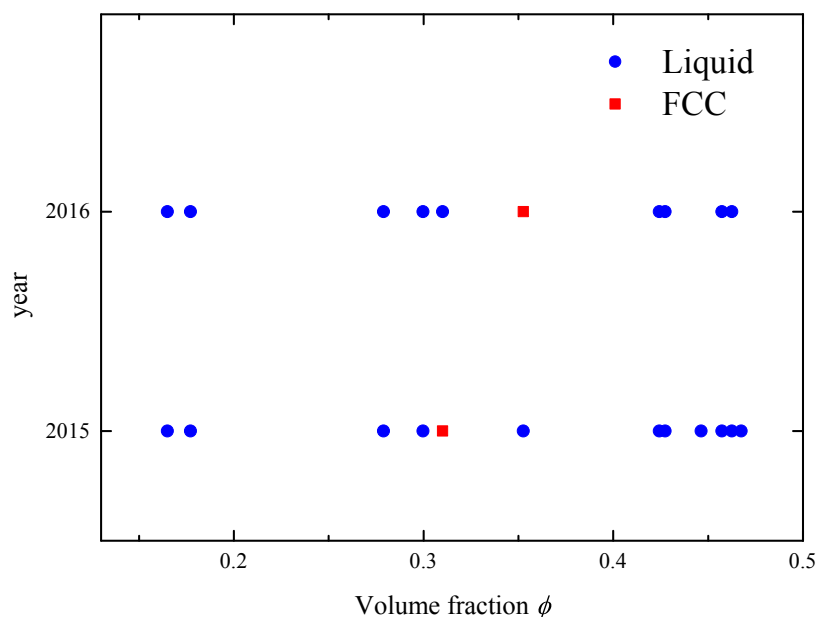
Figure 3.43: A phase diagram of Levasil30 developing between 2015 to 2016. The fcc structure(red) appears at higher volume fraction over time.
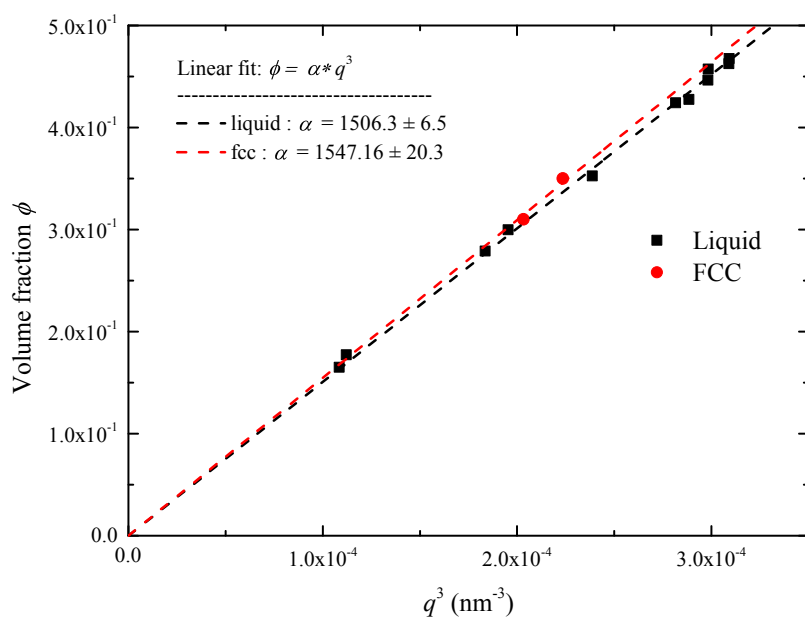
Figure 3.44: A calibration curve of q_{1st}^3 in nm^{-3} vs the volume fraction ϕ for Levasil30 with a constant α=1547.16.

Levasil50

Form factors of Levasil50 showed a high polydisperse property poisoning the shape of the form factor of hard-sphere (see Fig.3.45). For dialysized samples of Levasil50, they did not crystallized. Therefore, all dialyzed samples of Levasil50 were not interesting for further investigation in this study.
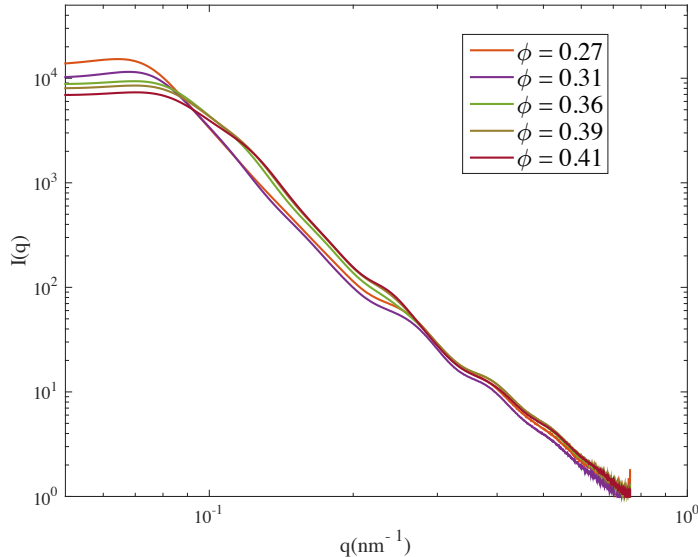
Figure 3.45: Form factors of Lesavil50 samples ($\phi = 0.27$ to 0.41%) were distorted according to the high polydispersity in the population.

3.4.3 Crystal nucleation and growth

The 2015 SAXS experiment results revealed that the population of Levasil30 were able to form a crystal (fcc structure) at $\phi = 0.31$. Therefore, we decided to observe a crystal nucleation and its growth in Levasil30. We prepare three fresh dialyzed samples at 5mM NaCl on the site by diluting a high volume fraction sample into $\phi = 0.31, 0.32$, and 0.33. After the dilution, three samples were immediately investigated by SAXS.

Levasil30, $\phi = 0.31$: From the year 2015 phase diagram of Levasil30 (Fig. 3.43), at $\phi = 0.31$ particles in dispersions behaved in liquid phase and formed the fcc structure. Figure 3.46 shows the kinetics experiment at $\phi = 0.31$ that levasil30 particles behaved in a liquid phase and an fcc structure was detected to be growing all times during the observation. And its volume fraction after ten hours of preparation was measured as $\phi = 0.308$ by fitting with a calibration curve of Levasil30 (see Fig. 3.47).

Levasil30, $\phi = 0.32$: From the year 2015 phase diagram of Levasil30 (Fig. 3.43), at $\phi = 0.32$ we had no information about the particles phase. The kinetics experiment at $\phi = 0.32$ (Fig. 3.48) showed levasil30 particles behaved in a liquid phase and an fcc structure was detected to be growing all times during the observation. This observation can also fill a missing point in the Levasil30 phase diagram. The volume

fraction after ten hours of preparation was measured as $\phi = 0.32$ by fitting with a calibration curve of Levasil30 (see Fig. 3.49). The kinetics experiment at $\phi = 0.31$ was agreed well with the phase diagram.

Levasil30, $\phi = 0.33$: From the year 2015 phase diagram of Levasil30 (Fig. 3.43), at $\phi = 0.33$ we had no information about the particles phase. Figure 3.50 showed interesting results of the kinetics experiment at $\phi = 0.33$. A few minute after the dilution, particles still behaved in the liquid phase without a signal of the nucleation of a crystal. An fcc structure was detected about four hours later. According to this late nucleation, at volume fraction above 0.33 colloidal population of Levasil30 may take a longer time for a nucleation of a crystal. These could be explanation why the fcc structure was formed in the sample of $\phi = 0.35$ in the 2016 observation, a year later after the preparation. The volume fraction after ten hours of preparation was measured as $\phi = 0.334$ by fitting with a calibration curve of Levasil30 (see Fig. 3.51).

Figure 3.46: The scattering intensities of Levasil30 at 5 mM NaCl, $\phi = 0.31$. The fcc stricture was observed to be growing and superimposing on the liquid peak.

Figure 3.47: The nucleation analysis of Levasil30 $\phi = 0.31$: (top) The area under the $Iq^2 \cdot q$ (nm^{-3}) curve which relate to the occupancy of particles in the liquid phase. (bottom) The evolution of volume fractions over time.
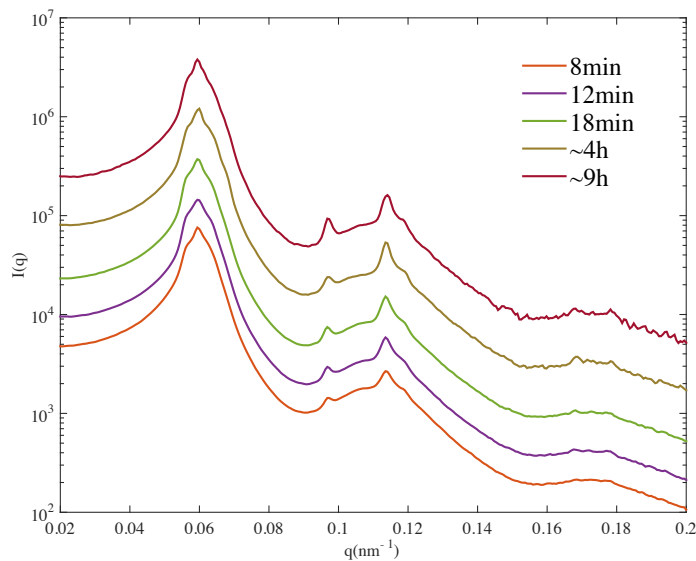
Figure 3.48: The scattering intensities of Levasil30 at 5 mM NaCl, $\phi = 0.32$. The fcc stricture was observed to be growing and superimposing on the liquid peak.
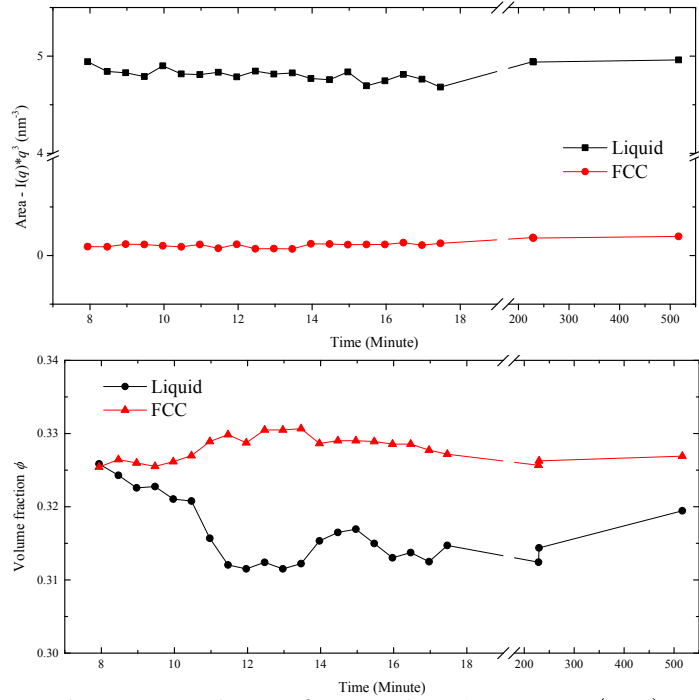
Figure 3.49: The nucleation analysis of Levasil30 $\phi = 0.32$: (top) The area under the $Iq^2 \cdot q$ (nm^{-3}) curve which relate to the occupancy of particles in the liquid phase. (bottom) The evolution of volume fractions over time.
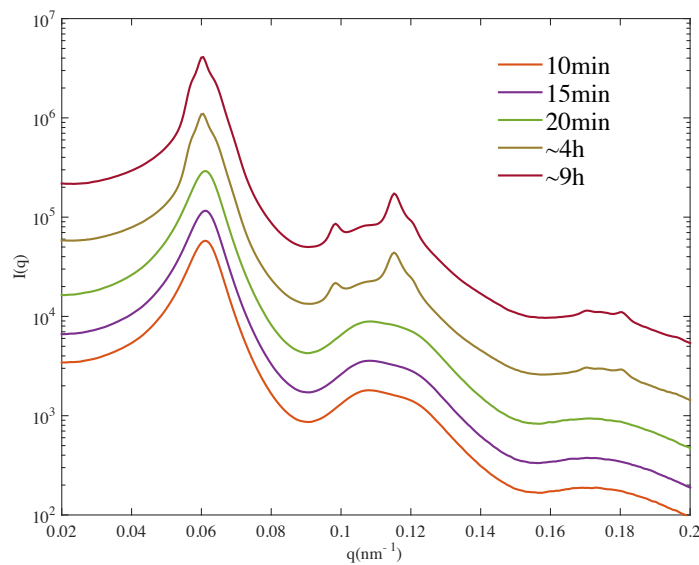
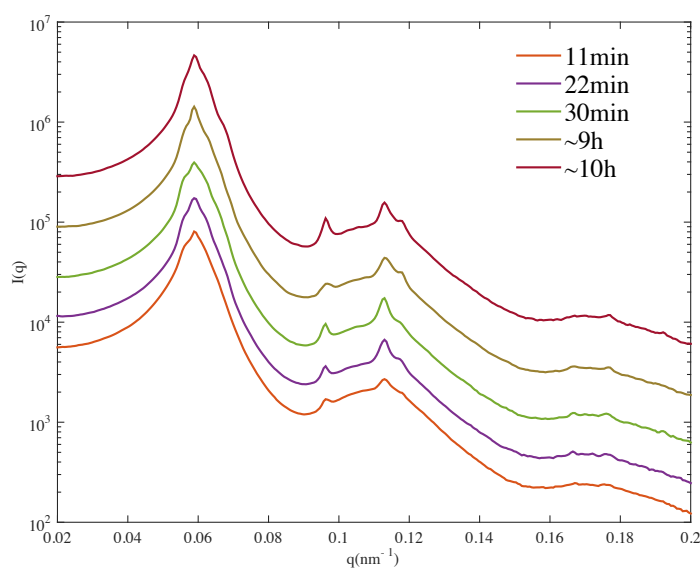Figure 3.50: The scattering intensities of Levasil30 at 5 mM NaCl, $\phi = 0.33$. The fcc stricture was observed to be growing and superimposing on the liquid peak.

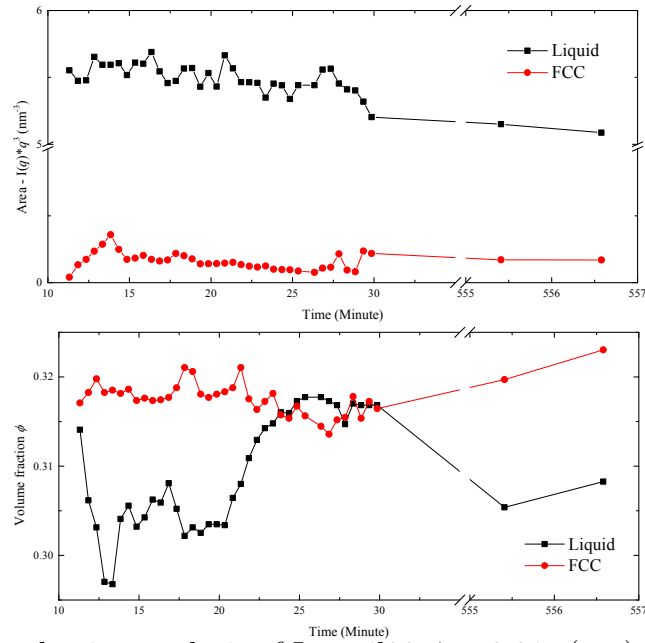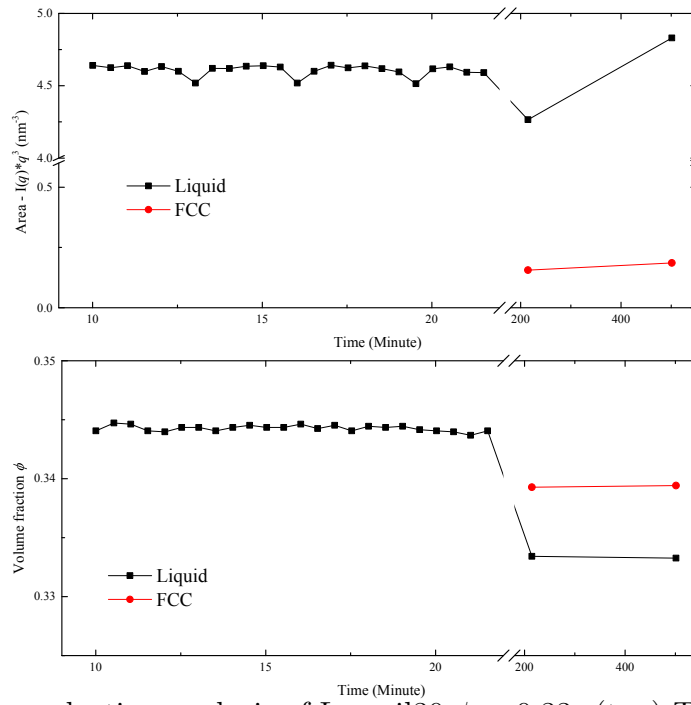Figure 3.51: The nucleation analysis of Levasil30 $\phi = 0.33$: (top) The area under the $Iq^2 \cdot q$ (nm^{-3}) curve which relate to the occupancy of particles in the liquid phase. (bottom) The evolution of volume fractions over time.

3.5   Summary and discussion

Here I conclude results of three year follow-up of the fractional crystallization of polydisperse silica nanoparticles and some part of our early published results which have been impacted to the field of study. About hundred samples were prepared by dialysis against standard solutions of PEG. This method allowed us to prepared samples with different range of particles size, salt concentrations, and broad range of solid volume fraction. The osmotic pressure was obtained from the equation of state in [15, 46]. The SAXS experiments allow to identify properties of each nanoparticles and the phase behaviors of population in dispersions (see table 3.1).

Type	Particle size (nm)	Polydispersity (%)	Phase	The primary crystal (Kinetics experiment)
TM50	13.3 ± 0.6	11.1 ± 0.3	liquid, hcp, fcc, bcc	fcc
				bcc ($\phi > 0.2$)
HS30	7.5 ± 0.5	16.0 ± 0.2	liquid, AB_{13}, bcc, Laves	bcc
HS40	7.9 ± 0.4	15.0 ± 0.3	liquid, AB_{13}, bcc, Laves	bcc
SM30	4.8 ± 0.3	19.2 ± 0.5	liquid	Not observe
Levasil30	48 ± 2	11 ± 3	liquid, fcc	fcc
Levasil50	49 ± 3	36 ± 4	liquid	Not observe

Table 3.1: Sample summary, showing the particle type, the particle size, the polydispersity, and observed phases.

To understand how population of polydisperse nanoparticles organize themselves in which crystal phase, we compare HS40 results to the previous work of Cabane et al.[15] which was using the same particle type of HS40. For HS40, we observed crystal structures of the bcc+AB_2 Laves+AB_{13} system, meanwhile Canabe and coworkers[15] observed crystal structures of the bcc+AB_2 Laves system. Botet et al. [16] reported the numerical simulation results which was comprehension of Canabe et al.[15]. First, they show that at the thermodynamic equilibrium of bcc + fcc system: when the polydispersity is increased, particles more likely to build the bcc crystal than the fcc since the bcc structure is more efficiently in term of the energy than the fcc structure. Second, it is the average-size particles $\langle a \rangle$ (the most popular size) in particle distribution to build the first set of crystal structure (bcc) with the lowest energy. The rest of population then consist of bi-disperse mixtures and start to build another crystals (AB_2 Laves) (see Fig.3.53). This agree well with our kinetics experiment (crystals nucleation and growth) result of HS40 that we always observe sharp peaks

67
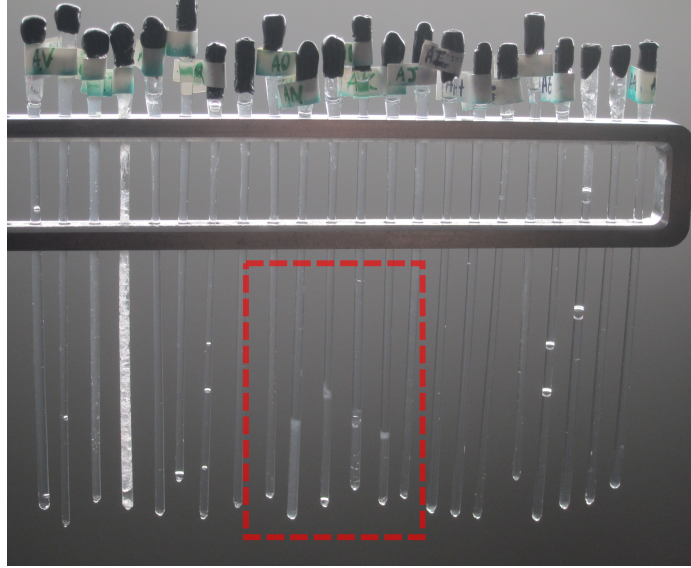
Figure 3.52: Dialyzed samples of HS40 at 5mM. The phase separations were seen in samples ($\phi = 0.21$ to 0.23) as different in colour (translucent on the top part and milky-like at the bottom of samples) in the red dash square.

of the bcc structure with strong growth. This also confirm the existence of fractional crystallization of polydisperse particles. Meanwhile, the secondary crystallization was seen only once in the crystal nucleation of TM50 at $\phi = 0.19$, a fcc structure appeared to coexistent with the bcc structure after about 11 hours of the sample preparation. For HS40 at 5mM, there was an on/off crystallizing behaviour of the bcc stracture in the HS40 phase diagram (see Fig.3.22). These suggested to be an result of a phase separation which occurred after the sample were kept vertically for a long time. This phase separation was also observed to exist in real samples (see Fig. 3.52).
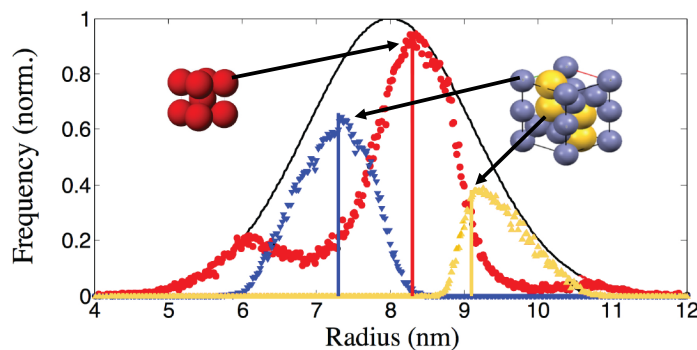
Figure 3.53: A schematic shows a radius distribution of particle of HS40: the initial distribution (black line) with the $\langle a \rangle = 8$ nm. The bcc phase is formed by the particles with radii close to $\langle a \rangle$ (red). The residual particle on the left (blue) and the right (yellow) hand side of distribution form the AB_2 Laves (adapted graphic from [15, 16]).

At the liquid to crystalline transition in charged colloids, the effective structure factor $S(q)$ is comprised from the liquid scattering pattern and sharp diffraction peaks of crystals. For TM50 and HS40, we have observed abundance of crystallines in every salt concentrations. The results showed that a crystal structure will form when the maximum intensity of structure factor $S_{max}(q)$ exceeds a value 2.85. This intriguing results agreed well with the Hansen-Verlet criterion [56] for freezing of liquid to crystalline transition in a dilute monodisperse population. Although the dispersions in this work were polydisperse, the Hansen-Verlet criterion is still valid (see Fig.3.54 and Fig. 3.55).
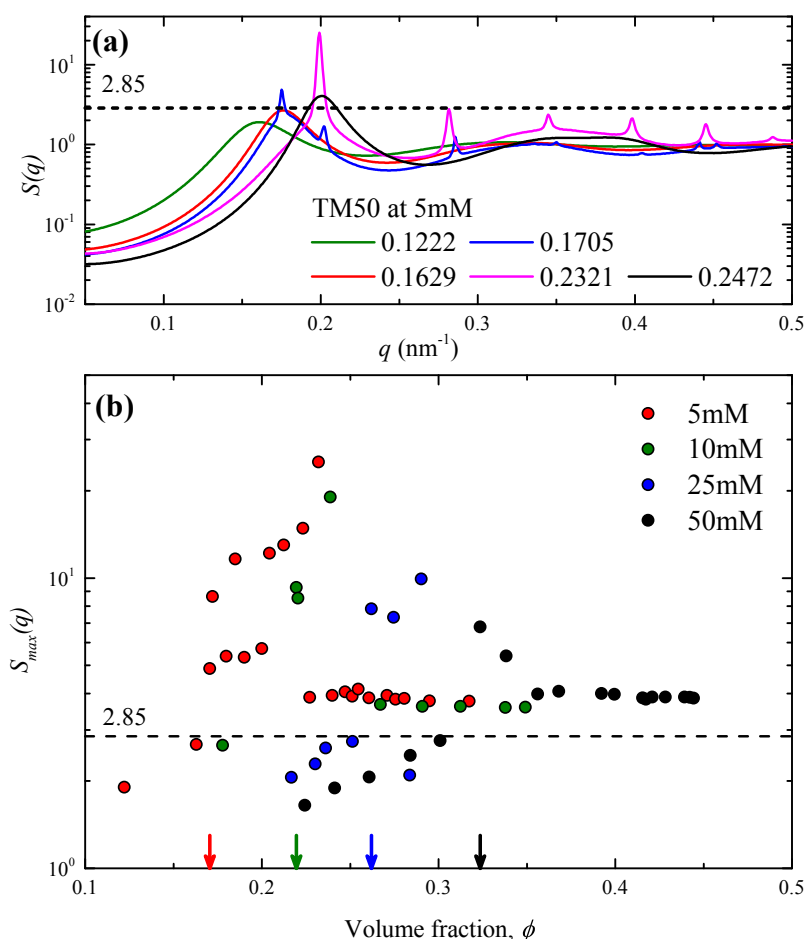
Figure 3.54: (a) Effective structure factor $S(q)$of TM50 at 5mM. At low volume fraction, the dispersions has a liquid structure. When the intensity $S(q)$ of the liquid peak exceeds a value 2.85, the dispersions has liquid and crystal structures. (b) The maximum effective structure factors $S_{max}(q)$ of TM50 at 5mM to 50mM. The points below the vertical dashed-line show the dispersions being in the liquid structure, while the points above the line being in the crystal or quench (glass) structure. The arrows show the critical volume fraction where the first crystal structure appears.
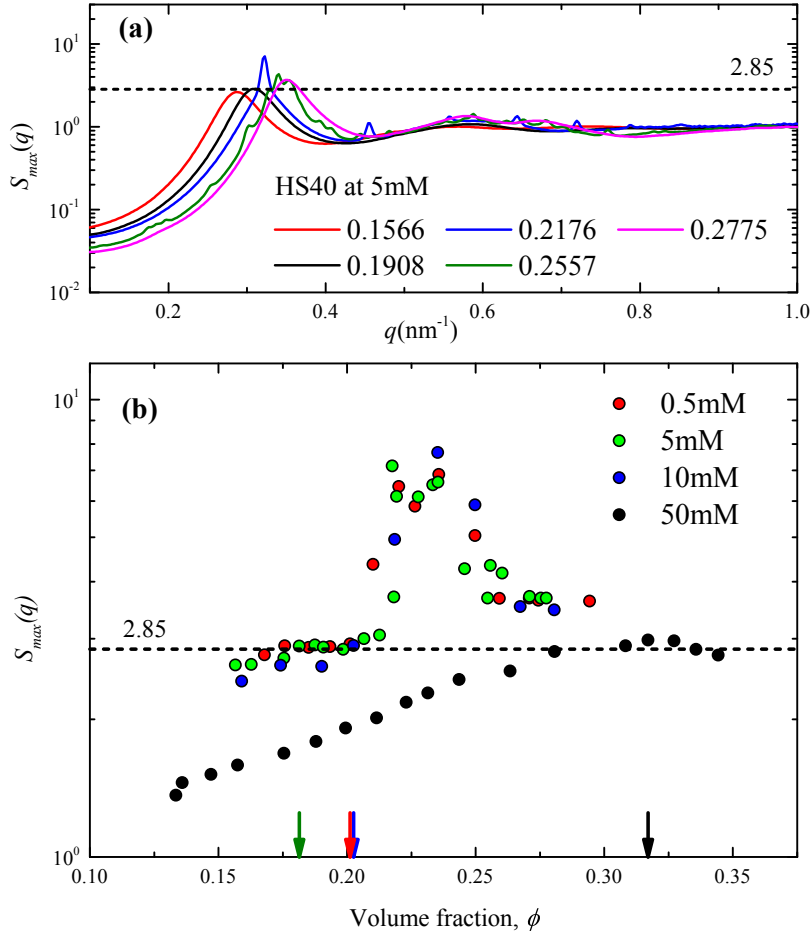
Figure 3.55: (a) Effective structure factor $S(q)$ of HS40 at 5mM. At low volume fraction, the dispersions has a liquid structure. When the intensity $S(q)$ of the liquid peak exceeds a value 2.85, the dispersions has liquid and crystal structures. (b) The maximum effective structure factors $S_{max}(q)$ of HS40 at 0.5mM to 50mM. The points below the vertical dashed-line show the dispersions being in the liquid structure, while the points above the line being in the crystal or quench (glass) structure. The arrows show the critical volume fraction where the first crystal structure appears.

In 2017, we published the early results of osmotic compression experiments on colloidal SM30, HS40 and TM50 together with the equation of state(EOS) calcuted by the PBC model[22] without a free parameter. However, the predicted osmotic pressure and the experimental results were in good agreement at the lower salt concentration, but failed at higher salt concentrations. Recently, Y. Hallez and M. Meireles have published an improved model for an EOS of charged-colloidal dispersions[71]. They introduced our experimental results on the osmotic pressure of HS40 [22] to show that their new EOS agreed very well with the experimental results (Fig. 3.56).
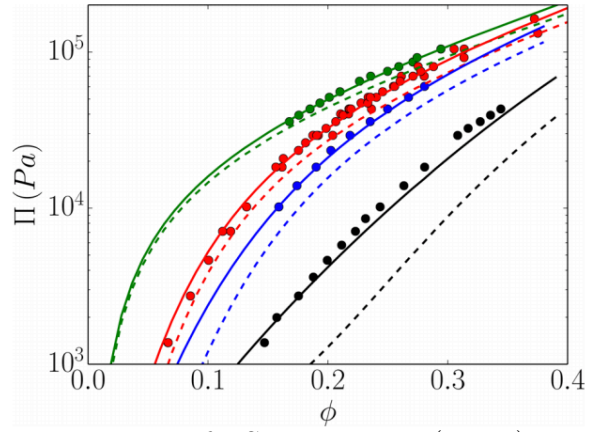
Figure 3.56: The osmotic pressure of HS40 at 0.5mM(green), 5mM(red), 10mM(blue), and 50mM(black). The dashed lines are the prediction from our PBC model. The solid lines are the prediction generated by the improved theory of Y. Hallez and M. Meireles. (Reproduced from the reference [71])

Chapter 4

Directional drying of colloids

During drying, colloidal dispersions can show a variety of transformations such as buckling[25, 72], wrinkling[72], cracking [72, 73], delamination [73, 74], shear banding [20, 21], structural anisotropy [40], etc. These phenomena are responses of microscopic interactions, between particles and between the fluid medium. If we understand how these interactions scale up to the macroscopic effect, we then are able to control or prevent these instabilities to occur during the drying of dispersions.

Here we present experimental results of responses of a drying colloidal dispersion to explained:

(1) A structural anisotropy of drying colloidal dispersions by using an advection-diffusion model of a drying-colloidal dispersion with a Poisson-Boltzmann cell model of inter-particle interactions.

(2) The formation of shear banding and guiding crack during the drying of colloidal dispersions.

I will briefly introduce some necessary theories and setups of experiments that were being used in these part. Theories are developed to support my experiments by colleague.

4.1   Collective diffusion

Consider a single spherical particle dispersed in unflowing water, one can describe its movement by a random Brownian motion. A droplet of colloidal dispersions,about 1μl radius of 10 nm and volume fraction of 0.01, contains about $\sim 10^{16}$ particles. As

these particles move they may move past to the surrounding particles, consequently generating an anisotropic distribution of neighbouring particles, also thermodynamic forces which slow its movement [6]. These movement of a large number of particles can be describes by the concentration (collective) diffusion.

Here, we consider a colloidal dispersion that is drying in a Hele-Shaw cell as in figure 4.1. A colloidal dispersion is injected in a cavity of the cell with the initial volume fraction $\phi = \phi_0$. At one end of the cell, the evaporation occurs at a rate $\dot{E}$ leaving the deposit of colloidal particle behind with volume fraction $\phi = \phi_f$, that is growing back to the cell at speed of w. This evaporation causing a flow of liquid from the other end to compensate the loss of evaporating liquid. The velocity within the cell can be distinguished into the velocity of colloidal particles v_s, the velocity of the dispersant liquid v_l, and a bulk velocity $\bar{v} = \phi v_s + (1 - \phi)v_l$. Since all velocities are averaged over the cross section of the cell and the height of a cell is considered too small that any effects of gravity can be neglected. We assume that there is no material losses in the cell, thus the flux at any point in the cell must balance the drying rate $\bar{v} = \dot{E}$ at the edge. At the other end, far from the solidification front, the particle and liquid will travel with the speed of $\bar{v} = \dot{E}$. However, the mean velocity v_s and volume fraction ϕ are able to evolve. Remarkably, at the solidification front the velocity of particles will be forced to slow down to zero and the volume fraction will increase to ϕ_f. This precess is sketched in fig. 4.1.

Since the total mass of colloidal particles is conserved, one can derive an advection equation of particles:

$$\frac{\partial \phi}{\partial t} + \frac{\partial}{\partial x}(\phi v_s) = 0, \tag{4.1}$$

where ϕv_s is solid volume flux. In the transition region, from liquid to solid, particles will slow down and dispersant liquid must speed up due to conservation of the total flux. When the liquid current flows and hits particles, it cause a flow resistance (drag) and the momentum transfer (liquid phase to dispersed phase). Forces act on the dispersions can be described as the total pressure, or thermodynamic pressure, P which comprising of both solid and liquid.

$$P = p + \Pi, \tag{4.2}$$

where Π is the osmotic pressure of charged particles which can be derived by colloid-
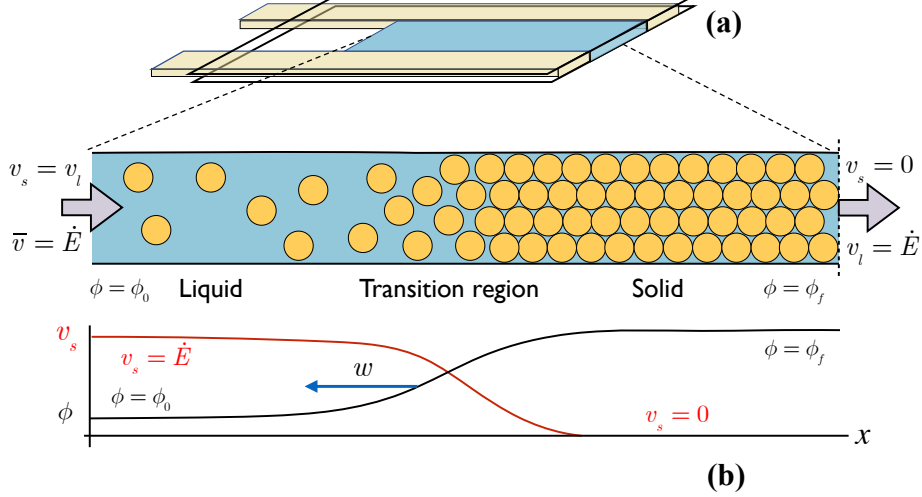
Figure 4.1: A sketch of a Hele-Shaw cell (a) and a directional drying colloidal dispersion in one dimension (b). The evaporation starts on the right of the cell at a rate $\dot{E}$, while the colloidal dispersions flow from the left with a volume fraction $\phi = \phi_0$ (Reproduced with modifications from [22]).

colloid interaction, and p is the pressure of fluid phase alone which can be measured as in references [36, 75]. Since there is no external force acting on dispersion, the momentum balance can be expressed as $\nabla P = 0$. We now apply this in a one dimension problem, the equation 4.2 is rewritten to

$$\frac{\partial \Pi}{\partial x} = -\frac{\partial p}{\partial x} = nF_d, \tag{4.3}$$

where n is the number density of particle (number of particle per volume; i.e. particle radius of a, $n = 3\phi/4\pi a^3$), and F_d is the average drag force per particle.

Consider a single particle of radius a moves at a relative speed $v_s - \bar{v}$ in a dispersant fluid of viscosity mu_0, and the average velocity $\bar{v}$, the drag force can be determined by the Stokes drag $-6\pi\mu_0 a(v_s - \bar{v})$. In a dense dispersion, the hydrodynamic interaction will enhance the drag by the factor $r(\phi)$, here we use the semi-empirical expression $r = (1 - \phi)^{-6.55}$ [37, 76]. The osmotic pressure term can be evaluated by an equation of state $\Pi = nkTZ$, where $Z(\phi)$ is the compressibility factor depending on the the colloid-colloid interaction and the clouds of ions around a particle, kT is the Boltzmann energy. Substituting these two expressions in the equation 4.3 gives

$$kT\frac{\partial}{\partial x}(nZ) = -6\pi\mu_0 a(v_s - \bar{v})rn. \tag{4.4}$$

We rewrite the equation 4.4 by the Stokes-Einstein diffusivity, $D_0 = kT/6\pi\mu_0 a$ which

74

is a diffusion constant of a single spherical particle and introducing the chain rule:

$$\phi v_s = \phi \bar{v} - D_0 \tilde{D} \frac{\partial \phi}{\partial x}, \tag{4.5}$$

while

$$\tilde{D}(\phi) = \frac{1}{r(\phi)} \frac{\partial \phi Z}{\partial \phi} = \frac{D}{D_0}, \tag{4.6}$$

where $\tilde{D}$ is the dimensionless diffusivity, and D is the collective diffusivity. Substitute the equation 4.5 into the equation 4.1, we contain the advection-diffusion model of colloidal transport [22, 36, 37, 40, 77],

$$\frac{\partial \phi}{\partial t} + \frac{\partial}{\partial x} \left(\phi \bar{v} - D_0 \tilde{D} \frac{\partial \phi}{\partial x} \right) = 0. \tag{4.7}$$

We want to describe a changing in concentration in the liquid-solid transition region, in this case a reference frame that co-moving with the drying front is considered by the transformation $x' = x - wt$, where w is the velocity of the drying front that growing backwards into the cell. We are interested in a steady-state solution with a boundary condition $\phi = \phi_0$ far from the transition front $(x \to -\infty)$. Therefore, inside the spatial derivative term in equation 4.7 is constant, and the evolution of the volume fraction in the liquid-solid transition region is rewritten,

$$\frac{\partial \phi}{\partial x} = \frac{(\bar{v} - w)(\phi - \phi_0)}{D_0 \tilde{D}} = \frac{(\phi - \phi_0)}{L \tilde{D}}, \tag{4.8}$$

where $L = D_0/(\bar{v} - w)$ is the natural length-scale of the drying front.

(a)   **(b)**
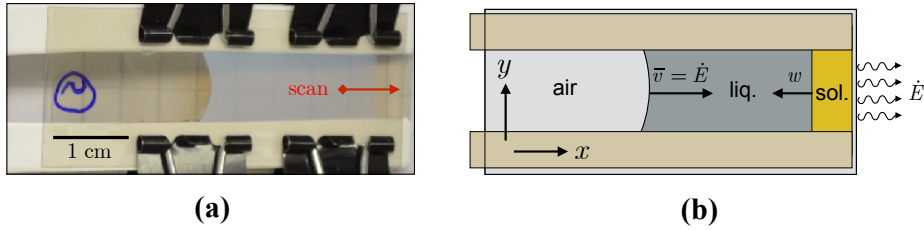
Figure 4.2: (a) Dispersions were allowed to dry in a Hele-Shaw cell. (b) the sample geometry is described by the moving solidification front with velocity w, and a receding liquid meniscus with velocity $\bar{v} = \dot{E}$, and one end where the evaporation occur and the deposit of dispersions are formed (Reproduced with modifications from [22]).

We prepared thirteen samples of Hele-Shaw cell which were made from two glass slides with mica sheets (35 - 50 μm thick) inserted along the rims of slides. All layers were attached together by clips (as in fig. 4.2). We filled different colloidal dispersions, which were dialyzed against a solution of PEG same as described in chapter 3, into

cells and let them dry for approximately 8 hours. During the drying, we captured images of cells every 10 minutes, and measured the evaporation rate $\dot{E} = \bar{v}$ by tracking the retreating liquid meniscus in the cell as the average velocity $\bar{v}$. Meanwhile, the velocity of the front w was measured by the solid phase which growing into the cell. After 8 hours of drying, all cells were examined by SAXS in order to observe how volume fractions were changed along the drying direction in the cell.

4.1.1 Scattering of a drying colloidal dispersions by SAXS

The small angle x-ray scattering technique (SAXS) was used in this experiment to observe changes in the liquid-solid transition region during the drying of colloidal materials. To do this, we hung a cell in the vertical position and scanned a sample along the drying direction ($x-$axis), and extracted scattering intensities throughout the Hele-Shaw cell. Spectrum were azimuthally averaged over $\pm$ 5° to the $x-$ and $y-$ directions (see fig.4.3) and we measured the main scattering peak of the structure factors of both components: q_x is parallel to the flow and q_y is perpendicular to the flow. Since dispersions are being compressed in $x-$direction, we assume for the $z-$direction as $q_z = q_y$. The volume fraction in the cell then can be calculated as in the reference [22] by

$$\phi = \alpha(q_x q_y q_z) = \alpha(q_x q_y^2), \tag{4.9}$$

where α is a constant of a calibration curve that depends on the colloidal type as in chapter 3. We also measured deviatoric strain γ, expressing any volume-pressing due to the shear, as defined by [22, 40] :

$$\gamma = \frac{2}{3}\left(\frac{q_x}{q_y} - 1\right). \tag{4.10}$$

In figure 4.4 is presented the results of SAXS experiments, together with numerical predictions from [22]. For the experimental data, the origin of x axis was arbitrarily set at the volume fraction $\phi = 0.3$ which also corresponding to the origin of the volume fraction for proceeding the numerical prediction. For the model, we used the initial volume fraction ϕ from the smallest recorded experimental data and integrated equation 4.8 from the origin. Both in the experiment and model were using data of the particle size, salt concentration, and surface charge density $\sigma = 0.5e$ nm^2, as

76
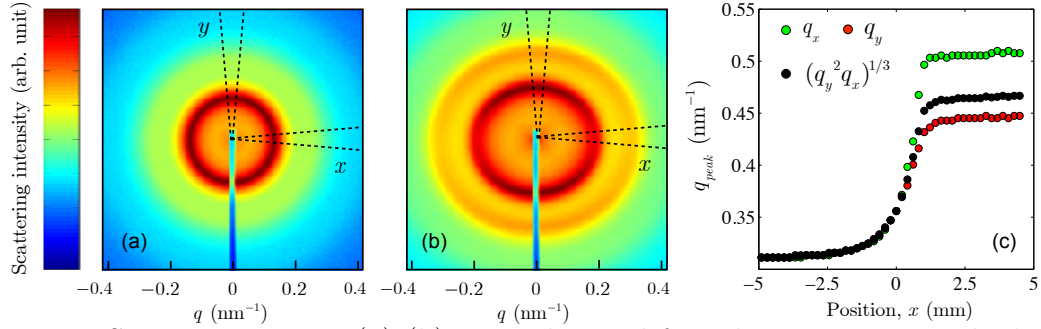
Figure 4.3: Scattering spectra(a)-(b) were obtained from locations across the liquid-solid transition region of drying dispersions in Hele-Shaw cells. (a) At low volume fraction, the dispersions behave as liquids without anisotropy between x and y directions. (b) At higher volume fraction, dispersions are packing closer together along the drying direction (x-axis) which cause a anisotropy on scattering spectra in x and y directions. (c) An evolution of q−values from liquid to solid: q_x value is higher than q_y, imply that dispersions are packed denser in x than y-axis. The averaged q−value $(q_x q_y^2)$ is used to calculate for a volume fraction ϕ and deviatoric strain γ (Reproduced from [22]).
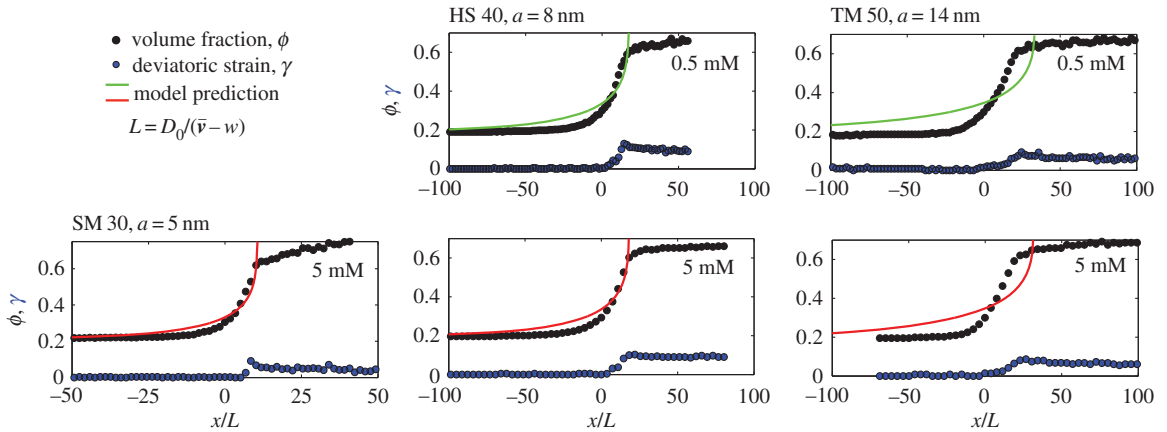
Figure 4.4: Observations of the liquid-solid transition region in the drying of five different dispersions, with various particle sizes and salt concentrations. The volume fraction ϕ (black points) and the derivative strain γ (blue points) are increasing from the left to the right as particles are packed close to each other. Distances are rescaled by the advection-diffusion length $L = D_0/(\bar{v} - w)$. Solid lines show the model prediction with a assumed surface charge density $\sigma = 0.5 \; e \; \mathrm{nm}^{-2}$ (Reproduced from [22]).

measured in the chapter 3. No other free parameters were used in the model.

The volume fraction is increasing as material is crossing the liquid-solid transition region, both in the experiment and numerical model. In the experimental compression curve the volume fraction ϕ is then bent nearly flat, after the aggregation of particles [40, 48]. Here, particles in the solid phase are gradually compressed due to the large capillary pressure. This elastic feature of compression cures haven seen in other report of drying droplets of complex fluids [15, 40, 46, 77–80]. At a critical volume fraction,

anisotropy is sets in. This is at $\phi = 0.33$ for the TM50 at0.5 mM and $\phi = 0.47$ for the SM30. The anisotropy between q_x and q_y occurs in drying dispersions. After this point, the deviatoric strain is rapidly increasing and reaches a maximum value by the end of the liquid-solid transition. As cracks form in the dried solid to relax the total strain, the deviatoric strain curve is gradually decreasing into the solid phase.

In real space, the observed liquid-solid transition has a width about 1 to 2 mm which is rescaled by the advection-diffusion length ($L = D_0/(\bar{v} - w)$) so that we are able to observe the effect of inter-particle interactions on the compression of the dispersion during drying. In the model, particle behaviour is compared to that of point-like masses, like an ideal gas, which would cause a sharp drying front where $(\phi - \phi_0) \sim e^{x/L}$. The high charge of silica particle can effect on the electrostatic interaction which leads to enhance of the width of the liquid-solid transition. The drying fronts remain well fit by a exponential in increase concentration. However, exponential behaviour give length scales which range from 6.6L, for the smaller SM30 to 15.6L for the larger TM50. Thus, although the advection-diffusion model of non-interacting particle, can provide a concept of the effect, it underestimate the width of the drying front in all cases. This is due to the enhanced interparticle interaction of charged colloids.

As was described in equation 4.6, we can summarise interparticle interactions in an effective collective diffusion coefficient, $\tilde{D}$. We can now estimate this dimensionless diffusivity $\tilde{D}$ (the effective diffusivity) by applying a numerical derivative of data in figure 4.4 in to equation 4.8. The results are shown in figure 4.5: both model and experiment show that the larger particle size, the more the effective diffusivity $\tilde{D}$ is enhanced by the inter-particle interactions. The effective diffusivity $\tilde{D}$ from our model predictions do not agree with experiments which suggested as a result of non-DLVO interactions [22]. However, the effective diffusivity $\tilde{D}$ from experiments show similar feature with the contemporaneous observation of $\tilde{D}$ in Ludox AS40[80] which was measured by different method, using Raman micro-spectroscopy (see fig.4.5(d)).

we also used a different modified Carnahan-Starling equation ($Z_P(\phi)$) from Pepin, Elliot and Worster[36] to estimate the effective diffusivity instead of equation 2.11, we notice no difference at below $\phi = 0.60$ until at $\phi = 0.64$ (near random close packing) its turns upwards at large volume fraction. And if this compressibility factor $Z_P(\phi)$
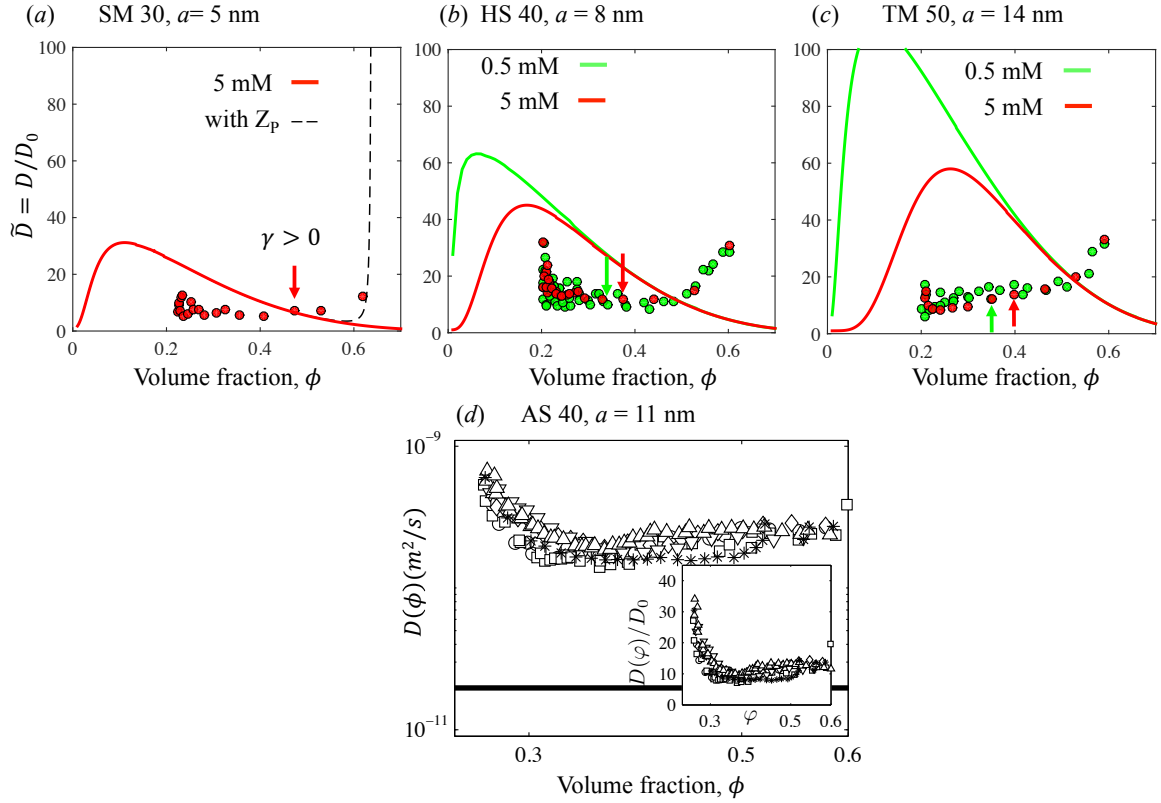
Figure 4.5: Measured and predicted dimensionless diffusivities for colloidal silica of Ludox (a) SM30, (b) HS40 and (c) TM50, equilibrated at 0.5mM (green) and 5mM (red). Arrows show the volume fraction where the the deviatoric strain γ is non-zero. In (a), the modified hard-sphere compressibility factor Z_P from Peppin *et al.* (dashed line) is also used in order to compare with our model. In (d), results of measured dimensionless (collective) diffusivity of silica colloidal for AS40 by Loussert *et al.* (Reproduced from [22, 80] with modifications).

was used replacing the equation 2.11, we see no difference in response at $\phi < 0.60$ (see fig.4.5(a)). It also cannot explain the increasing in the effective diffusivity.

As the first structural anisotropy appears in dispersions, at this point, the deviatoric strain $\gamma \neq 0$ and dispersions takes a yield stress and a finite shear modulus. At this volume fraction, the individual particles will start being captured by strong interactions with their surrounding neighbours. (marked in fig.4.5 with arrows). The $\tilde{D}$ is suddenly increasing at, or shortly after, the particles start to behave as a weak, soft solid.

4.2 Pattern and instabilities driven by drying fronts

In the previous section, we have demonstrated both with theory and experiment of the structural anisotropy in the liquid-solid transition during drying of colloidal dispersions. The mass and force balance are able to predict how a colloidal dispersion is compressed during directional drying, and how the compression affects the state of the dispersion (e.g. enhancing of the collective diffusivity, anisotropy). In this section, we focus on macroscopic mechanical instabilities which relate to compression during the drying of a colloidal dispersion. First, we show that shear bands are formed and scale with the film thickness. Furthermore, we show how to control shear bands by changing the concentration of salinity which affects to the electrostatic interaction in colloidal dispersions. Then last, we show that paths of the later cracks, appear after the drying of the colloidal film, are influenced by an anisotropic pre-stress or strain, leftover from the liquid to solid transformation.

4.2.1 Shear bands

During the drying of colloidal dispersions, striped structures of bands frequently have been observed (see fig.4.6): They are the first reported in sol-gels by Hull and Caddock [74]. They found that bands were oriented at $\pm 45°$ to the cracks which appeared later. Similar band features also were observed and displayed in many figures of studies of drying colloidal dispersions [30, 40, 81, 82]. However, there was no discussion on the bands until Berteloot and his co-worker [83] report their appearance after the drying front line. They suggest that the band could be either shear bands base on its visual similarity to these feature in the stress loaded metal [84]. Yang *et al.* [20] also reported that shear bands were controlled by the yield stress and strain rate (drying rate) of dried standing films [20].

Here, we show by direct measurement that the bands are form as results of shear deformations, how their pattern scale, how they can be restrained, and discuss about the compressive forces that played an important roll during the drying of colloidal dispersions. To dispose of any influence of a free surface or skin, we performed all experiments of a directional drying of colloidal dispersions in the Hele-Shaw cell similar to this shown in figure 4.1 or 4.2.
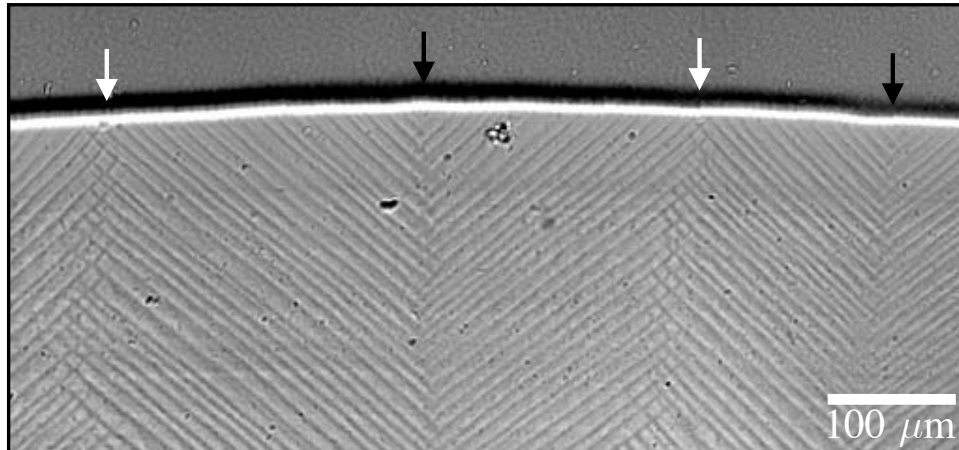
Figure 4.6: A micrograph of drying colloidal polystyrene in a free-standing film. The drying front is the bright horizontal line between the liquid film (above, on textured) and solid film (below, stripes). The shear bands in the solid film are tilted to the left and the right away from the front. The chevrons, stripes in V-shapes, that open towards to the front (black arrows) are sources of new bands, while the chevron that open away from the front (white arrows) are where growing bands end (Reproduced from [21]).

Colloidal material

For the study of shear banding in colloidal dispersions, we prepared banded films with various of charge-stabilized dispersions. Polystyrene dispersions with particle diameters d of 98, 100, 105, 115, 144, 198, and 283 nm were synthesized elsewhere. Additional colloidal silica Ludox HS40 ($d = 16$ nm) was dialysis against NaCl aqueous solution 5 mM, pH 9-10 as in section 2.2. Meanwhile, Levasil30 ($d = 92$ nm) was used as received. All dispersions were then diluted by NaCl aqueous solutions to prepare dispersions with concentrations of 0 to 60mM, and volume fractions $\phi \sim 5\%$. Deionized water (Millipore) was used for all steps.

We prepared colloidal films by pipetting 180μl of dispersions on a glass slide for freestanding films, or in the cavity of Hele-Shaw cell. For Hele-Shaw geometries, cells were made as shown in figure 4.1(a). The thickness of the cells was selected by using various plastic spacers of 150, 230, 250, 300, 400, or 500 μm. After films dried, their actual thickness h were confirmed by microscopy. For thinner films, the spacers were built with heat-curable polymer sheets or double-sided tape which provided measured thicknesses h of a cell between 36 to 72 μm.

Observation

We observed the growth of shear bands in dried colloidal films, both in freestanding

81
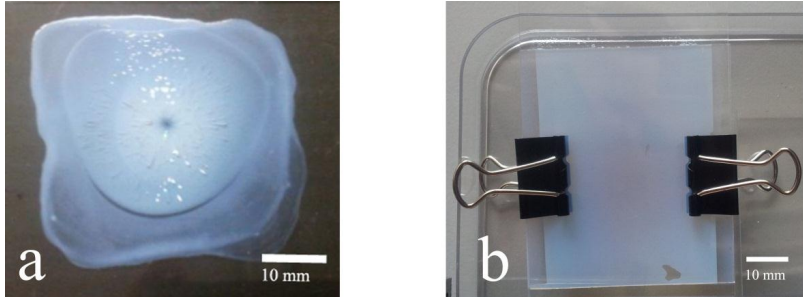
Figure 4.7: (a) A dry thin film of dispersions on glass slide substrate. (b) Drying dispersion in a Hele-Shaw cell, with a spacer's thickness of 150 μm.

films and in Hele-Shaw cells. The real-time observation shown that series of shear bands appeared behind the drying front and propagated in the same direction of the drying front at a comparable speed. One clear feature of shear bands that can be seen as that they are tilted strips to either the left or the right of the drying front. When the left and the right strips meet, they form boundaries that look-like chevrons [20, 21] opening to the front, or away from it (see fig. 4.6). The chevrons that opened towards the front repeatedly generated new bands on both sites of the chevron. However, time the chevrons that opened away from the front were sinks for growing bands. Some new shear bands, however, can propagate in the opposite direction of the drying front. These backwards propagating shear bands can propagate for short length and are forced to stop by the solidification of the (solid) film or can halt when they intersect another bands. Surprisingly, we found that a new shear band can form in between two existing shear bands and propagates in both direction forwards and backwards respective to the drying direction (see fig.4.8).

At first, the shear bands penetrated into the liquid-solid region at an angle of 45° and were then compressed along the direction of drying overtime. This caused the structure of the bands which can be seen in figure 4.6. During this compression period the volume fraction of the liquid-solid film was increased since the evaporation still draining water out of the film as described earlier in the anisotropy of a drying film. Later, if the invasion of cracks occurred, the bands also were compressed by the cracking opening (see figure 4.8(c)).

The independence of relative band spacing on thickness and particle size

We collected microscope images from 21 different fully dried films of different in thicknesses and sizes, including both freestanding films and Hele-Shaw geometries.

82
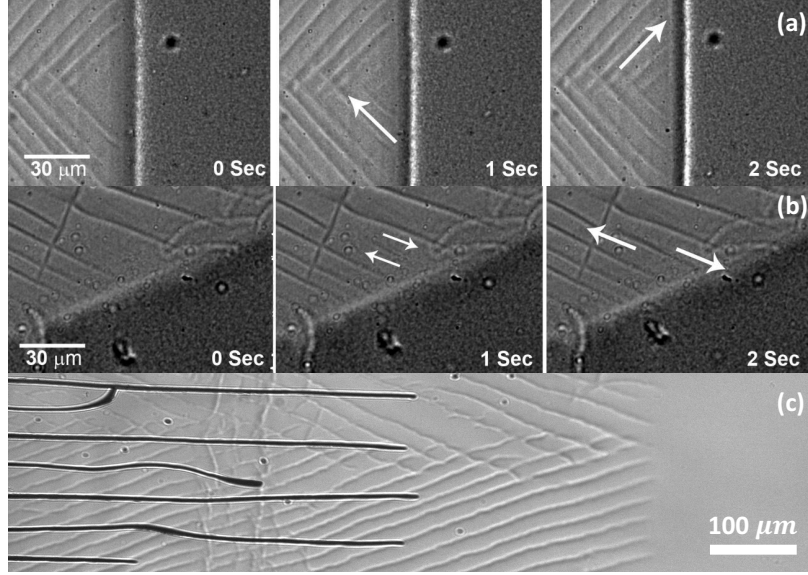
Figure 4.8: Panels (a) and (b) show time-lapse series of images of the appearance of new shear bands in a drying colloidal film of Ludox HS40. The first row (a) shows two propagating shear bands, the backwards propagating shear band appears at $t = 1$ s and the forwards propagating one appears at $t = 2$ s. The direction of travel is indicated by white arrows. The second row (b) shows a new shear band that develops between existing bands and then propagates backwards and forwards. (c) The invasion of cracks in a drying film of Ludox HS40 occurs behind the drying front, and the shear band front.

The final opening of chevron was $99° \pm 7°$, as a result of further compression after bands formed, (see fig.4.9(a)) after the samples were fully dry. We observed the spacing λ between two stripes of bands was various in length. Therefore, the eight different particle sizes of colloidal dispersions were prepared in 150-μm-thick Hele-Shaw cells and pipetted with 180 μl of dispersions. After all films dried, each film was scanned by digital microscopy under the transmitted light in order to capture images in ten different locations. We measured about 20 band spacings and calculated their average spacing, together with the standard deviations. We report the standard deviation rather than the standard error, because the bands could have wide variations in the spacing within a single cell, as shown in figure 4.6. Since the bands formed with a range of band spacing from 0.2 to 0.5 times of the films thickness, we report the relative band spacing $\bar{\lambda} = \lambda/h$.

In figure 4.9(a) we show that the relative band spacing $\bar{\lambda}$ did not depend on the particle size or particle type, for the particle size from 16 to 283 nm. The spacing λ, on average, was 0.36 times the film thickness h. After shear bands occurred, they was still a weak or soft solid, they were then compressed further by the compression

83
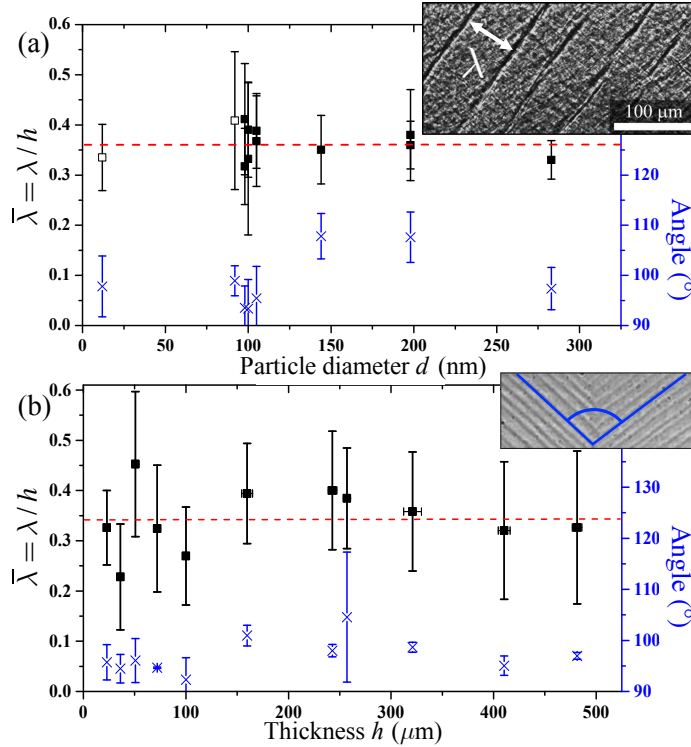
Figure 4.9: The relative band spacing (squares, the left axis) and the average opening angle (blue, the right axis) were measured in Hele-Shaw cells. Bars are standard deviation of each measurement. The inset panels shows how the measurements are conducted. Figure (a) shows results in 150-μm-thick cells, for colloidal polystyrene (filled squares) and silica (open squares) at low ionic strength (1-5 μM), while figure (b) shows results for fixed particles $d \approx 100$nm, in cells of different thickness (Reproduced from [21]).

due to the drag. These caused the opening of chevron larger than 90°, which was the angle of between two bands when they intersected. We also dried an equal mixture of two particles sizes, 98 and 198 nm, which was also consistent with this result ($\lambda/h = 0.29 \pm 0.13$) (see fig.4.9(b)).

In another set of experiment, we fixed the particle size by using the dispersions with diameter $d \approx 100$ nm (each experiment was repeated with 92 nm silica and 105 and 115 nm polystyrene particles) and then dried them in different thicknesses from 36 to 500 μm. The results show in figure 4.9(b). We found that the relative band spacing $\bar{\lambda}$ did not depend on the film thickness. Explaining more clearly, the band spacing λ scales linearly with the film thickness h. We measured the averaged $\bar{\lambda} = 0.34$ which also agrees with the results for the changing particle size experiment.

The electrostatic effect on the shear bands

84
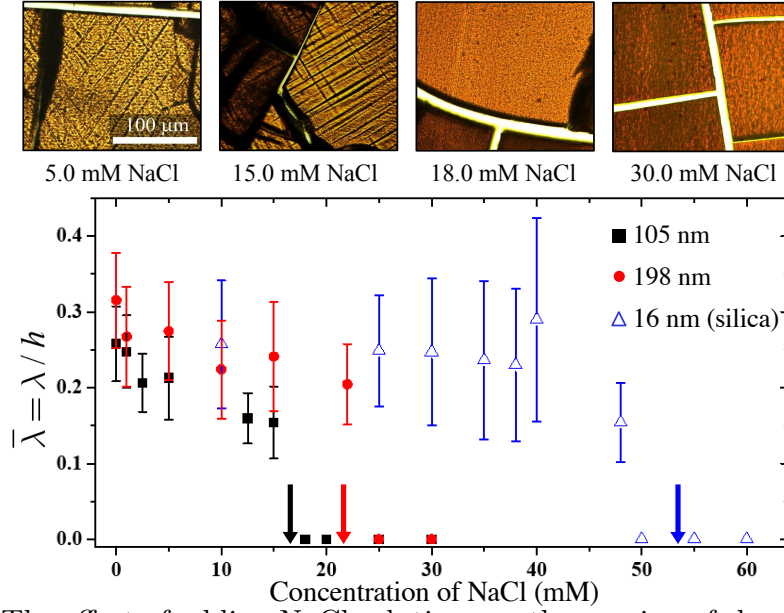
Figure 4.10: The effect of adding NaCl solutions on the spacing of shear bands. Shear bands can be eliminated ($\bar{\lambda} = 0$) by addition of salt, with a critical level depending on particle size and composition. Arrows point where the strongest interactions between nearby particles [eq. 2.1] drop below 5 kT. Panels above show how dried films change with the salt concentration, for 105 nm polystyrene, and vanish above 15 mM concentration. (Reproduced from [21])

Since all colloidal dispersions are charged-stabilized to proven them for the aggregation, the balance between the repulsive electrostatic force and the attractive van der Waals force in a colloidal system is controlled by the electrostatic screening effect and the salt concentration. This effect can be described by the DLVO potential theory. In this part, we study how the shear band was affected when the strength of electrolytes was changed by manipulating the salinity of the dispersions. We used the DLVO potential theory and PB-cell model (as described in chapter 2) to explain the end results. We used the three different particle sizes, 105 and 198 nm colloidal polystyrene and 16 nm colloidal silica in NaCl solution of up to 60 mM, dried in 150-μm-thick cells. Images of the band spacing were captured by microscopy and were used to measure the band's width.

Figure 4.10 shows that the increasing of salt concentrations has a direct effect on the spacing of shear bands. When salt concentrations are increased, more concentration of electrolyte, the average spacing of shear bands decrease slightly, but not vanish. However, when the salt concentration exceeds some critical salt concentration, bands did not form. This concentration depends on particle size and type and can be estimated from the DLVO potential theory in equation 2.1. Below the critical

concentration, band spacings appear to be a weak negative dependence on the salt concentration. For our study, we found that shear bands disappeared at salt concentrations where the maximum value of the DLVO potential was lower than $5kT$, calculated from equation 2.2. At the point, the repulsive forces between particles can build the effective cages, according to the PB cell model (see fig. 2.2), and freezing particles into a semirigid arrangement. In other words, shear bands disappear when the electrostatic interaction is weakened to the point that a soft repulsive solid do not form during the transition of liquid to a solid film.

The birefringence of the shear bands

The directional dried colloidal films are birefringent, since they were compressed along the direction of drying [40, 41]. The birefringence around shear bands is a tool here to measure how the bands strain the film around themselves. We put fully dried films under a microscope equipped with crossed polarizing filters and a half-wavelength filter (first-order retardation plate). Sample were placed on a tunable table in between two filters (see figure 4.11 (a)). We rotated the dried films and collected images of each film at 10° intervals. The microscope was working in transmission mode for all observations.

First, the observation was performed under white light, which showed the birefringence in a film by shining in various colours (figure 4.11 (b) - (c)). As we turned a film (through $0° - 180°$) and captured thier images, colors around bands also changed suggested that there was a changing (twisting) in the optic axis around shear bands. These images were then digitally counter-rotated, by this means we were able to measure the intensity I of the transmitted light through any particular point in the film, as it was turned about an angle θ.

Later, we put a 533 nm filter (green) in front of the first polarizer so that we can observe the birefringence of bands from a monochromatic light. The intensity $I(\theta)$ of the light will be minimized when the optic axis is oriented along one of the crossed polarizers. We could measure the orientation ψ of the optic axis across the film, by fitting a sinusoidal variations in light intensity, $I(\theta) = I_0 \sin^2(2(\theta + \psi)) + I_{bkg}$ [22], at each at pixel on images as shown in figure 4.12 (a). The root-mean-squared average of the reorientation of the optic axis, or $\langle|\psi|^2\rangle^{1/2}$ that can be related to the average shear
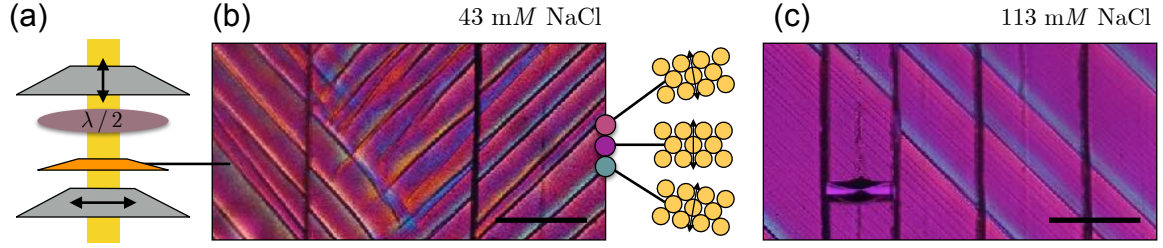
Figure 4.11: (a) A setup for polarized microscopy: the film is placed between crossed polarizers and a half-wavelength filter. (b) Using white light, the film appears purple when the optic axis is aligned with the initial polarizer. Birefringence appears by colour changes in the film: clockwise rotation of optic axis shifts the colour to blue, while counterclockwise to the red. (c) The addition of salt in the drying film reduces the intensity of these colour variations. At high salt, the lighter shear bands can be seen in between main bands. Scale bars are 200 μm (Reproduced from [22]).

which is taken up by shear bands [22]. Figure 4.12 (b) shows that the (root-mean-squared) average in the film slowly decreases from 6° for the dried film of dispersions at initial salt concentration, to 2° at about 100mM of salt concentration, just before the shear bands disappear. If the shear bands form at the liquid-solid transition, we can predict the strength of shear which is release by the bands and compare it to what is observed. As described in the opening chevron, the drag forces cause the uniaxial compression across the liquid-solid region, which results in increasing the volume fraction. If particles have formed a soft repulsive solid, they can carry a shear stress or anisotropic strain. To calculate the amount of shear strain available for the shear bands, one assume the particle is compressed at the critical volume fraction ϕ_c, where the first soft repulsive solid appears (or where $\gamma > 0$ as shown in figure 4.4) to the final volume fraction ϕ_f. Since the force is a uniaxial compression and materials are not expanded in any other direction, the compressive strain that occurs by this compression is relate to the volumetric strain, $\epsilon_x = (\phi_f - \phi_c)/\phi_c$. This is equivalent to the shear strain of $\gamma = \epsilon_x/2$ at $\pm$ 45° to the direction of compression [21]. To estimate the critical volume fraction ϕ_c, we defined ϕ_c as the volume fraction at the minimum of DLVO potential reached $5kT$, and assumed $\phi_f = 0.64$ for random close-packed particles.

In figure 4.12(b), we compared the accumulated shear strain γ calculated from above approximation and express as an engineering strain, with the average reorientation, $\langle|\psi|^2\rangle^{1/2}$, observed in dried Levasil films, for different salt concentrations. Then, γ were fitted to the data by a single scaling factor in the magnitude of γ, of
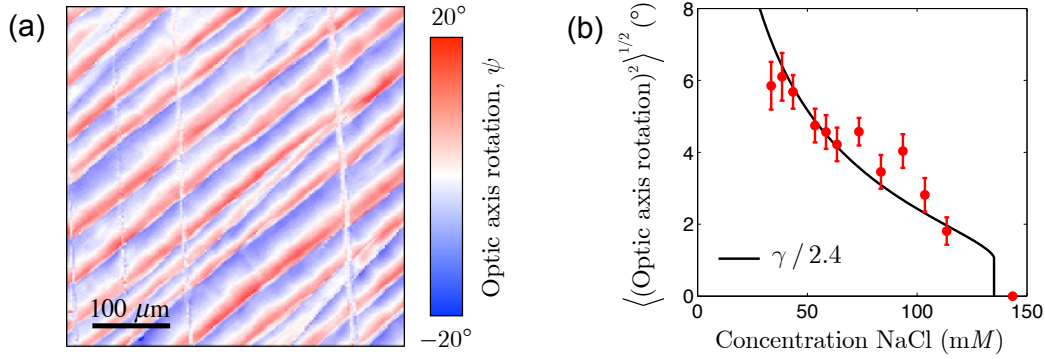
Figure 4.12: Shear bands can reorient the anisotropy in a colloidal film and can be eliminated by addition of salt. (a) A sample with 43.5 mM NaCl was observed here. The pattern of film distortion can be mapped by polarization microscopy, showing that the bands localized the shear strains. (b) The (root-mean-squared) average changes induced by the bands were measured for dispersions of colloidal silica with various initial concentrations of NaCl. The average reorientations of the film (filled points) are proportional to the total amount of uniaxial compression applied to the film, between the gelation and aggregation fronts, as predicted by a DLVO calculation (black line). (Reproduced from [21]).

order one, and we find that there is good agreement between the strain that is generated across the liquid-solid transition and the strain released by the formation of shear bands.

Here we have shown how shear bands, which regularly appear in drying colloidal films, form and scale. The shear bands relieve the compressive strain by slipping at $\pm 45°$ to the drying front. This compressive strain was proportional to the deviatoric strain of the liquid-solid transition which not been released by the shear band. Adding some salt concentration reduced the electrostatic effect and lead to the decreasing in the band spacing. At the critical salt concentration, where the DLVO potential about $5kT$, shear bands disappeared.

4.2.2 Guiding cracks

In this part, we study the cracks that appear in solid film, due to capillary forces [6]. Here we show that cracks in dried colloidal films can be guided by the structural anisotropy of the dried film, and hence the memory of the drying direction. Similar memory of drying has been seen in reference [85].

We performed the experiment by drying Levasil 30 in Hele-Shaw cells in which we modified the pattern of evaporation by adding or covering up more opening channels around the edge of each cell so that we can guide the drying fronts in relatively

Figure 4.13: Guiding cracks in drying colloidal dispersions. (a) Colloidal silica (Levasil 30) is dried in a Hele-Shaw cell with a set of opening gaps around the edge to allow evaporation. The series tim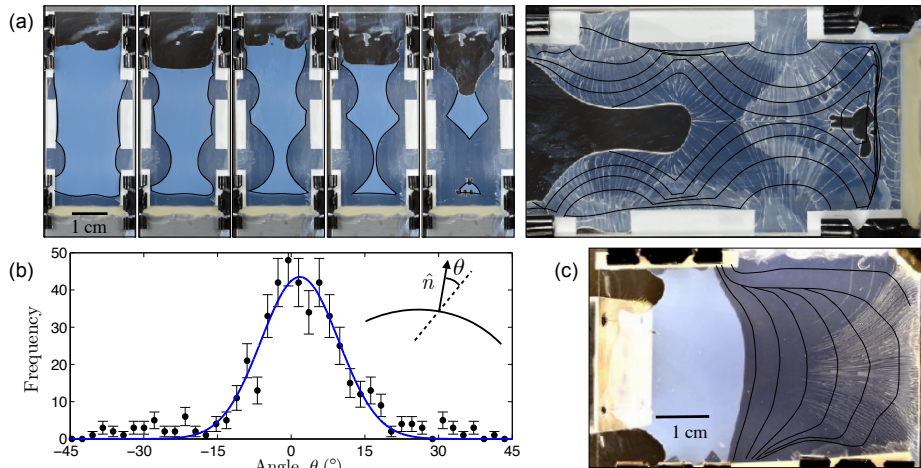e-lapse images showing the film in steps of one hour. The liquid dispersions (milky white) dries into dark solid deposit. The completely dried cell with cracks and previous drying front profiles is show in the larger right-hand panel. (b) The angle between a crack and the outward-pointing normal of the drying front profile is measured. At $0°$ these are aligned in the same direction (mean of 463 measurements is $1 \pm 1°$ and standard deviation $13 \pm 1°$). (c) Another experiment of a drying cell, where one side was sealed after five hours and was taken in steps of four hours. In this case, one can see how cracks bend to follow the memory of the drying front. (Reproduced from [22]).

arbitrary ways. For example, the drying cell in figure 4.13 (a) had four small gaps of 5-10 mm along the sides of the cell. At beginning of any experiments, aqueous dispersions of Levasil 30 was pipetted into the cells, which were initially inclined slightly to allow the dispersion to settle to one side. Until the solid layer appeared on the edges, we hung the cells vertically and took images of their drying pattern. During this, the cells can be refilled by pipetting additional dispersion into the top edge.

In each film, we found that when cracks form, they preferentially align along the direction which the dispersions had solidified. This is true for every points throughout the film, even if cracks appeared hours after solidification (figure 4.13 (a)) or if the drying front has move well on and had subsequently changed shape (figure 4.13 (c)). Figure 4.13 (a) shows a drying cell at the one-hour intervals, with lines of the liquid-solid front drawn in black. The final pattern of cracks, after the entire film has solidified, clearly expresses the pattern of drying, in such a way that the cracks are parallel to the direction of compression of the material everywhere in the dry deposit. We also measured 463 intersections between the cracks and the drying front profiles in

89

figure 4.13 (a), measured the misalignment between the outward-pointing normal to the liquid solid transition at those points and the direction that a crack subsequently followed. The result is presented in figure 4.13 (b) that the cracks are very well aligned with a mean misdirection of $1 \pm 1°$ and a standard deviation of $13 \pm 1°$ (fitting by the simple Gaussian distribution).

Here we showed the crack propagation was guided by the memory of drying front. This memory was the structural anisotropy which arose in the liquid-solid transition during the drying of a colloidal film.

4.3   Summary and discussion

Here we conclude the results of studies on the directional drying of colloidal dispersions and their instabilities. During drying, colloidal dispersions undergo complex transformations such as solidification, bucking, cracking, shear band and the draining of liquid from pores. These responses are controlled by forces that occur from microscopic interactions between nearby particles and between particles and fluid around them. If we aim to control these instabilities, we must first understand these microscopic interactions and how they scale up to the macroscopic effect.

We showed that an advection-diffusion model of drying colloidal in a Hele-Shaw cell and explain much of the mechanical instabilities occured in drying. The model is constructed by Poisson-Boltzmann cell model of the electrostatic interactions between particles and aims to predict the osmotic pressure, the collective diffusivity of a charged colloidal dispersion. This model had no free parameters.

We performed drying experiment in Hele-Shaw cell. The SAXS technique was used to measure the changing of volume fraction across the liquid solid transitions of a drying colloidal dispersion. We found that the model can predict the changing in volume fraction of drying front, especially well for smaller particles. In fact, the concentration profiles across the liquid solid transition were stretched wider than would be expected for only hard-sphere interactions and this stretching of front was stronger for the large particles [22]. When the drying profiles were used to infer the effective diffusivity of various colloidal dispersions, we found that the collective diffusivity was increased at intermediate-to-high volume fractions, where particles were behaving as

a yield-stress material, like a paste or gel, not a simple fluid. The increase in volume fraction was not captured by the model, and suggested that particles may present non-DLVO interactions. We also explored the effect of microscopic interaction through shear bands and cracks. The shear bands release the uniaxial compression, which was fed by drag force, of the film by slipping at $\pm 45°$ to the direction of compression. Furthermore we show that the amount of slip (average reorientations of the film) was proportional to the amount of deviatoric strain of the liquid-solid transition which not been released by the shear band. Shear bands can be eliminated by adding on salts, in order to decrease the repulsive force between particles. Meanwhile, cracks released strain energy to allow soft-solid dispersion to shrink more as it dried. We showed that the structural anisotropy which the liquid-solid drying front left behind could be the pathways of cracks.

Chapter 5

Conclusion and Outlook

I have investigated instabilities in colloidal dispersions which can be considered in two parts, the first part is a study of crystallizations of polydisperse colloids. The aim of this part is to look for possible crystal structures that can occur under different conditions (e.g. size, polydispersity, thermodynamically equilibrium) in order to construct phase diagrams. I had presented a model to predict the osmotic pressure at the equilibrium. I also observed the nucleation of a colloidal crystal and the diffusion of two colloidal mixtures. The second part is a study of instabilities of a drying colloidal dispersion. The same model in the first part was used here to predict volume fractions of the liquid-solid transition during the colloidal dispersion dried. I also observed and explained how shear bands were formed and how to eliminate them by changing the microscopic interaction of colloidal particles. Furthermore, I reported how cracks in a directional drying colloidal film were guided by the drying front.

crystallizations of polydisperse colloids

I prepared about hundreds of colloidal systems, all samples were dialyzed against a variety of salt solutions (0-50mM) and PEG concentration in order to reach volume fractions ϕ 0.10 to 0.40 at the equilibrium. A model was developed by Poisson-Boltzmann cell (PBC) model of the electrostatic interactions between particles to image the microscopic interaction between inter-particle interactions and predict the concentration gradient of a drying colloidal dispersion. The model can predict the osmotic pressure of a colloidal system at the equilibrium of charged colloidal dispersions, but appears to be unsuccessful for a system that has at a high salt concentration

and large particle size. However, Y. Hallez and M. Meireles [71] have reported on an improved model of the electrostatic interactions between colloidal particles and have tested the model with our experimental data. The results showed that our osmotic compression experiments and their predictions were in a very good agreement.

Dialyzed samples (liquid) were explored through the SAXS and were analyzed their crystal structures by extracted structure factors $S(q)$. The $q-$value of peak intensities were collected to create a calibration curve of $q^3 - \phi$. From the structure-factor analysis, I found plentiful crystal structures (from simple structures - bcc, fcc, laves to large and complex structures- Ab_{13}) coexisting with the liquid phase in Ludox TM50, HS30 and Levasil 30. A phase diagram of TM50, collecting from the experimental results, agreed well with a numerical prediction calculated by our collaborators (Guillaume Bareigts and Christophe Labbez) in France. Despite our colloidal dispersions are charged and quite polydisperse, we found that a crystal structure always appears at $S(q)_{max} > 2.85$ which is in agreement with the the empirical Hansen-Verlet rule of crystallization [56], which strictly for the monodisperse hard sphere. This will be seen more clearly, when we look at the nucleation of these colloidal dispersion. I prepared fresh colloidal dispersions at volume fractions where the first crystal appears in the phase diagram in order to look their nucleation in real times. The nucleation experiment showed that the first appearing crystal phase is a simple structure (either bcc-structure or fcc-structure) which appears alone among the colloidal populations without coexisting of any other larger structure. This behaviors could be a selective crystallization (fractionation) in the polydisperse colloidal populations that the majority population (their size are close to the mean) involve in the first crystal nucleation and let the rest of population, which are now different in sizes, cooperate to build other complex structure [15, 16].

Furthermore, I studied the interdiffusion of two different concentrated colloidal system and showed that the diffusivity was enhanced 15 times by the internal interactions.

instabilities of a drying colloidal dispersion

In this part, I explored the structural anisotropy in the dried film. The films were dried in Hele-Shaw cells and placed in the an X-ray beam. I performed SAXS

experiments to measure the scattering vectors in two orientation at the liquid-solid transition: q_x parallel to the flow and q_y perpendicular to the flow. I used in same PBC model to predict the volume fraction and the diffusivity at the liquid-solid transition and compare them with the experimental results. At the liquid-solid transition, I found that the drying colloidal dispersions become anisotropic $(q_x \neq q_y)$, the strain in drying film is rapidly increased. The model catch with the experiment at a small particle, but again failed for the larger particle-size. I also estimated the effective diffusivity in the liquid-solid transition and found that the larger the charged particle, the more the effective diffusivity is enhanced by the inter-particle interactions. Here, the experiment and the model tangibly disagree, although the observed diffusivity shows the same trends as the other experiments. The developing of a new model is needed to match with the experiment.

Furthermore, I observed shear banding and guiding cracks in a drying film. I showed that the shear bands are the mechanical response to the uniaxial compression in film which is released by allowing for slip at $\pm 45°$ to the direction of compression. In particular, I show that the amount of slips created by shear bands was proportional to the total amount of deviatoric strain that would have accumulated across the liquid-solid transition [22]. I also show that shear bands can be optimized or eliminated by adjusting the chemistry of the starting dispersion (by adding salt) before it dries. The cracks appear after in order to release strain energy by allowing the dispersion to shrink more as it dries. We showed that the pathway of cracks is guided by the anisotropy that was left behind the liquid-solid transition.

Acknowledgements

Many people were involved in this thesis both direct and indirect supports. I would like to use this chance to thank them.

First of all, I would like to express my deep gratitude to my supervisor, Lucas Goehring, for stimulating and guiding me in my work at the Max Planck Institute. His intensive comments when asked for an advice always wake me up to eager to overcome the problem. I would like to thank the people in our group: (Jan) Sudaporn Vesaratchanon, Antoine Fourriere, Pawan Nandakishore, (Shaka) Shaghayegh Javadi, Arnaud Hemmerle, Paolo Fantinel, Octavio Albarrán, Soumyajyoti Biswas, Jana Lasser, and especially Joaquim Li whom I was working closely in the early year of my Ph.D. and his great advice for bringing my good hands in the chemistry lab.

I would like to thank my family and Nan for their love and great support throughout the years of my Ph.D. and for their patiently waiting until it comes to an end.

I would like to thank Stephan Herminghaus for the opportunity to work at the fascinating department. I am grateful to Marcus Müller for being referees of my thesis.

Many Thanks go to the people from the Department of Complex Fluids at the Max Planck Institute for Dynamics and Self-Organization: To both Barbara Kutz and Monika Teueteberg for helping me with regulations and papers which I never ever familiar with. Anupam Sengupta and Carsten Krüger helped me with the birefringence microscopy. Kris Hantke helped me to struggle with the optics, while Markus Benderoth supported me concerning chemicals. Thomas Eggers who always supported me with IT and big data transferring.

I would like to thank the following people for their collaborations and supports, without whose help this work would never have been possible: Bernard Cabane for very impressive discussions, Robert Botet supported for the size polydispersity measurement, Franck Artzner helped me concerning crystallography, and Michael Sztucki

Bibliography

[1]P. N. Pusey and W. van Megen, "Phase behaviour of concentrated suspensions of nearly hard colloidal spheres", Nature **320**, 340–342 (1986).

[2]S. Hachisu, Y. Kobayashi, and A. Kose, "Phase separation in monodisperse latexes", Journal of Colloid and Interface Science **42**, 342–348 (1973).

[3]A. Kose, M. Ozaki, K. Takano, Y. Kobayashi, and S. Hachisu, "Direct observation of ordered latex suspension by metallurgical microscope", Journal of Colloid and Interface Science **44**, 330–338 (1973).

[4]P. N. Pusey, E. Zaccarelli, C. Valeriani, E. Sanz, W. C. K. Poon, and M. E. Cates, "Hard spheres: crystallization and glass formation", Philosophical Transactions of the Royal Society A: Mathematical, Physical and Engineering Sciences **367**, 4993–5011 (2009).

[5]Y. Monovoukas and A. P. Gast, "The experimental phase diagram of charged colloidal suspensions", Journal of Colloid and Interface Science **128**, 533–548 (1989).

[6]W. B. Russel, D. A. Saville, and W. R. Schowalter, *Colloidal dispersions* (Cambridge University Press, 1989).

[7]A. Yethiraj and A. van Blaaderen, "A colloidal model system with an interaction tunable from hard sphere to soft and dipolar", Nature **421**, 513–517 (2003).

[8]P. Pusey, "The effect of polydispersity on the crystallization of hard spherical colloids", Journal de Physique **48**, 709–712 (1987).

[9]S. R. Williams, I. K. Snook, and W. van Megen, "Molecular dynamics study of the stability of the hard sphere glass", Physical Review E **64** (2001) `10.1103/physreve.64.021506`.

[10]H. J. Schöpe, G. Bryant, and W. van Megen, "Small changes in particle-size distribution dramatically delay and enhance nucleation in hard sphere colloidal suspensions", Physical Review E **74** (2006) `10.1103/physreve.74.060401`.

[11]P. Sollich and N. B. Wilding, "Crystalline phases of polydisperse spheres", Physical Review Letters **104** (2010) `10.1103/physrevlett.104.118302`.

[12]M. Fasolo and P. Sollich, "Equilibrium phase behavior of polydisperse hard spheres", Physical Review Letters **91** (2003) `10.1103/physrevlett.91.068301`.

[13]A. B. Schofield, P. N. Pusey, and P. Radcliffe, "Stability of the binary colloidal crystalsAB2andab13", Physical Review E **72** (2005) `10.1103/physreve.72.031407`.

[14]N. J. Lorenz, H. J. Schöpe, H. Reiber, T. Palberg, P. Wette, I. Klassen, D. Holland-Moritz, D. Herlach, and T. Okubo, "Phase behaviour of deionized binary mixtures of charged colloidal spheres", Journal of Physics: Condensed Matter **21**, 464116 (2009).

[15]B. Cabane, J. Li, F. Artzner, R. Botet, C. Labbez, G. Bareigts, M. Sztucki, and L. Goehring, "Hiding in plain view: colloidal self-assembly from polydisperse populations", Phys. Rev. Lett. **116** (2016) `10.1103/physrevlett.116.208001`.

[16]R. Botet, B. Cabane, L. Goehring, J. Li, and F. Artzner, "How do polydisperse repulsive colloids crystallize?", Faraday Discussions **186**, 229–240 (2016).

[17]U. Thiele, "Patterned deposition at moving contact lines", Advances in Colloid and Interface Science **206**, 399–413 (2014).

[18]A. F. Routh, "Drying of thin colloidal films", Reports on Progress in Physics **76**, 046603 (2013).

[19]H. E. Bergna and W. O. Roberts, *Colloidal silica fundamentals and applications* (Boca Raton, FL : CRC Taylor & Francis, 2006, 2005).

[20]B. Yang, J. S. Sharp, and M. I. Smith, "Shear banding in drying films of colloidal nanoparticles", ACS Nano **9**, 4077–4084 (2015).

[21]P.-C. Kiatkirakajorn and L. Goehring, "Formation of shear bands in drying colloidal dispersions", Physical Review Letters **115** (2015) `10.1103/physrevlett.115.088302`.

[22] L. Goehring, J. Li, and P.-C. Kiatkirakajorn, "Drying paint: from micro-scale dynamics to mechanical instabilities", Philosophical Transactions of the Royal Society A: Mathematical, Physical and Engineering Sciences **375**, 20160161 (2017).

[23] H. Bodiguel, F. Doumenc, and B. Guerrier, "Pattern formation during the drying of a colloidal suspension", The European Physical Journal Special Topics **166**, 29–32 (2009).

[24] W. B. Russel, "Mechanics of drying colloidal dispersions: fluid/solid transitions, skinning, crystallization, cracking, and peeling", AIChE Journal **57**, 1378–1385 (2011).

[25] N. Tsapis, E. R. Dufresne, S. S. Sinha, C. S. Riera, J. W. Hutchinson, L. Mahadevan, and D. A. Weitz, "Onset of buckling in drying droplets of colloidal suspensions", Physical Review Letters **94** (2005) `10.1103/physrevlett.94.018302`.

[26] V. Lazarus and L. Pauchard, "From craquelures to spiral crack patterns: influence of layer thickness on the crack patterns induced by desiccation", Soft Matter **7**, 2552 (2011).

[27] P. Nandakishore and L. Goehring, "Crack patterns over uneven substrates", Soft Matter **12**, 2253–2263 (2016).

[28] L. Goehring, W. J. Clegg, and A. F. Routh, "Wavy cracks in drying colloidal films", Soft Matter **7**, 7984 (2011).

[29] C. Allain and L. Limat, "Regular patterns of cracks formed by directional drying of a collodial suspension", Physical Review Letters **74**, 2981–2984 (1995).

[30] E. R. Dufresne, D. J. Stark, N. A. Greenblatt, J. X. Cheng, J. W. Hutchinson, L. Mahadevan, and D. A. Weitz, "Dynamics of fracture in drying suspensions", Langmuir **22**, PMID: 16893207, 7144–7147 (2006).

[31] R. D. Deegan, O. Bakajin, T. F. Dupont, G. Huber, S. R. Nagel, and T. A. Witten, Nature **389**, 827–829 (1997).

[32] D. J. Harris, H. Hu, J. C. Conrad, and J. A. Lewis, "Patterning colloidal films via evaporative lithography", Physical Review Letters **98** (2007) `10.1103/physrevlett.98.148301`.

[33]C. Parneix, P. Vandoolaeghe, V. S. Nikolayev, D. Quéré, J. Li, and B. Cabane, "Dips and rims in dried colloidal films", Physical Review Letters **105** (2010) `10.1103/physrevlett.105.266103`.

[34]G. J. Kynch, "A theory of sedimentation", Transactions of the Faraday Society **48**, 166 (1952).

[35]M. A. Biot, "General theory of three-dimensional consolidation", Journal of Applied Physics **12**, 155–164 (1941).

[36]S. S. L. Peppin, J. A. W. Elliott, and M. G. Worster, "Pressure and relative motion in colloidal suspensions", Physics of Fluids **17**, 053301 (2005).

[37]S. S. L. Peppin, J. A. W. Elliott, and M. G. Worster, "Solidification of colloidal suspensions", Journal of Fluid Mechanics **554**, 147 (2006).

[38]P. B. P. Aimar, *Concentrated phases of colloids or nanoparticles: solid pressure and dynamics of concentration processes, in nano-science:colloidal and interfacial aspect*, edited by T. V. Starov CRC Press and F. Group (CRC Press, United States, 2010).

[39]N. Ziane and J.-B. Salmon, "Solidification of a charged colloidal dispersion investigated using microfluidic pervaporation", Langmuir **31**, 7943–7952 (2015).

[40]F. Boulogne, L. Pauchard, F. Giorgiutti-Dauphiné, R. Botet, R. Schweins, M. Sztucki, J. Li, B. Cabane, and L. Goehring, "Structural anisotropy of directionally dried colloids", EPL (Europhysics Letters) **105**, 38005 (2014).

[41]K. Yamaguchi, S. Inasawa, and Y. Yamaguchi, "Optical anisotropy in packed isotropic spherical particles: indication of nanometer scale anisotropy in packing structure", Physical Chemistry Chemical Physics **15**, 2897 (2013).

[42]J. A. Cohen, R. Podgornik, P. L. Hansen, and V. A. Parsegian, "A phenomenological one-parameter equation of state for osmotic pressures of peg and other neutral flexible polymers in good solvents", The Journal of Physical Chemistry B **113**, 3709–3714 (2009).

[43]T. Cosgrove, ed., *Colloid science: principles, methods and applications* (John Wiley & Sons Ltd, West Sussex, United Kingdom, 2010).

[44]R. P. Christian Holm Patrick Kékicheff, ed., *Electrostatic effects in soft matter and biophysics* (Springer, Germany, 2012).

[45] A. Robbes, F. Cousin, and G. Mériguet, "Osmotic stress on concentrated colloidal suspensions: a path towards equilibrium?", Brazilian Journal of Physics **39** (2009) `10.1590/s0103-97332009000200006`.

[46] J. Li, M. Turesson, C. A. Haglund, B. Cabane, and M. Skepö, "Equation of state of PEG/PEO in good solvent. comparison between a one-parameter EOS and experiments", Polymer **80**, 205–213 (2015).

[47] B. Jönsson, J. Persello, J. Li, and B. Cabane, "Equation of state of colloidal dispersions", Langmuir **27**, 6606–6614 (2011).

[48] J. Li, B. Cabane, M. Sztucki, J. Gummel, and L. Goehring, "Drying dip-coated colloidal films", Langmuir **28**, 200–208 (2011).

[49] W. C. K. Poon, E. R. Weeks, and C. P. Royall, "On measuring colloidal volume fractions", Soft Matter **8**, 21–30 (2012).

[50] R. K. I. (ed.), *The chemistry of silica: solubility, polymerization, colloid and surface properties and biochemistry of silica* (John Wiley & Sons, New York, 1979).

[51] J. H. van 't Hoff, "The function of osmotic pressure in the analogy between solutions and gases", Proc. Phys. Soc. London **9**, 307–334 (1887).

[52] J. des Cloizeaux, "The lagrangian theory of polymer solutions at intermediate concentrations", Journal de Physique **36**, 281–291 (1975).

[53] N. F. Carnahan and K. E. Starling, "Equation of state for nonattracting rigid spheres", The Journal of Chemical Physics **51**, 635–636 (1969).

[54] E. Trizac, L. Bocquet, M. Aubouy, and H. H. von Grünberg, "Alexander's prescription for colloidal charge renormalization", Langmuir **19**, 4027–4033 (2003).

[55] C. Bonnet-Gonnet, L. Belloni, and B. Cabane, "Osmotic pressure of latex dispersions", Langmuir **10**, 4012–4021 (1994).

[56] J.-P. Hansen and L. Verlet, "Phase transitions of the lennard-jones system", Physical Review **184**, 151–161 (1969).

[57] ESRF-ID02, *Id02 - time-resolved ultra small-angle x-ray scattering*, `http://www.esrf.eu/home/UsersAndScience/Experiments/CBS/ID02.html`, Jan. 2018.

[58] Sasview, *Sasview for small angle scattering analysis*, `https://www.sasview.org/`, Jan. 2018.

[59] D. Sivia, *Elementary scattering theory: for x-ray and neutron users* (Oxford University Press, 2011).

[60] M. N. van der Linden, A. van Blaaderen, and M. Dijkstra, "Effect of size polydispersity on the crystal-fluid and crystal-glass transition in hard-core repulsive yukawa systems", The Journal of Chemical Physics **138**, 114903 (2013).

[61] L. A. Fernández, V. Martín-Mayor, and P. Verrocchio, "Phase diagram of a polydisperse soft-spheres model for liquids and colloids", Physical Review Letters **98** (2007) `10.1103/physrevlett.98.085702`.

[62] R. Botet and B. Cabane, "Simple inversion formula for the small-angle x-ray scattering intensity from polydisperse systems of spheres", Journal of Applied Crystallography **45**, 406–416 (2012).

[63] V. Goertz, N. Dingenouts, and H. Nirschl, "Comparison of nanometric particle size distributions as determined by SAXS, TEM and analytical ultracentrifuge", Particle & Particle Systems Characterization **26**, 17–24 (2009).

[64] A. Torres, G. Téllez, and R. van Roij, "The polydisperse cell model: nonlinear screening and charge renormalization in colloidal mixtures", The Journal of Chemical Physics **128**, 154906 (2008).

[65] P. M. Dove and C. M. Craven, "Surface charge density on silica in alkali and alkaline earth chloride electrolyte solutions", Geochimica et Cosmochimica Acta **69**, 4963–4970 (2005).

[66] F. Artzner, S. Geiger, A. Olivier, C. Allais, S. Finet, and F. Agnely, "Interactions between poloxamers in aqueous solutions: micellization and gelation studied by differential scanning calorimetry, small angle x-ray scattering, and rheology", Langmuir **23**, 5085–5092 (2007).

[67] W. Bowen and A. Mongruel, "Calculation of the collective diffusion coefficient of electrostatically stabilised colloidal particles", Colloids and Surfaces A: Physicochemical and Engineering Aspects **138**, 161–172 (1998).

[68] G. K. Batchelor, "Brownian diffusion of particles with hydrodynamic interaction", Journal of Fluid Mechanics **74**, 1 (1976).

[69] B. U. Felderhof, "Diffusion of interacting brownian particles", Journal of Physics A: Mathematical and General **11**, 929–937 (1978).

[70] D. N. Petsev and N. D. Denkov, "Diffusion of charged colloidal particles at low volume fraction: theoretical model and light scattering experiments", Journal of Colloid and Interface Science **149**, 329–344 (1992).

[71] Y. Hallez and M. Meireles, "Fast, robust evaluation of the equation of state of suspensions of charge-stabilized colloidal spheres", Langmuir **33**, 10051–10060 (2017).

[72] Y. Zhang, Y. Qian, Z. Liu, Z. Li, and D. Zang, "Surface wrinkling and cracking dynamics in the drying of colloidal droplets", The European Physical Journal E **37** (2014) `10.1140/epje/i2014-14084-3`.

[73] L. Goehring, W. J. Clegg, and A. F. Routh, "Plasticity and fracture in drying colloidal films", Physical Review Letters **110** (2013) `10.1103/physrevlett.110.024301`.

[74] D. Hull and B. D. Caddock, Journal of Materials Science **34**, 5707–5720 (1999).

[75] L. Goehring, A. Nakahara, T. Dutta, S. Kitsunezaki, and S. Tarafdar, *Desiccation cracks and their patterns* (Wiley-VCH Verlag GmbH & Co. KGaA, May 2015).

[76] K. R. Hall, "Another hard-sphere equation of state", The Journal of Chemical Physics **57**, 2252–2254 (1972).

[77] L. Daubersies and J.-B. Salmon, "Evaporation of solutions and colloidal dispersions in confined droplets", Physical Review E **84** (2011) `10.1103/physreve.84.031406`.

[78] L. Daubersies, J. Leng, and J.-B. Salmon, "Confined drying of a complex fluid drop: phase diagram, activity, and mutual diffusion coefficient", Soft Matter **8**, 5923 (2012).

[79] F. Giorgiutti-Dauphiné and L. Pauchard, "Direct observation of concentration profiles induced by drying of a 2d colloidal dispersion drop", Journal of Colloid and Interface Science **395**, 263–268 (2013).

[80] C. Loussert, A. Bouchaudy, and J.-B. Salmon, "Drying dynamics of a charged colloidal dispersion in a confined drop", Physical Review Fluids **1** (2016) `10.1103/physrevfluids.1.084201`.

[81]L. Goehring, W. J. Clegg, and A. F. Routh, "Solidification and ordering during directional drying of a colloidal dispersion", Langmuir **26**, 9269–9275 (2010).

[82]M. I. Smith and J. S. Sharp, "Effects of substrate constraint on crack pattern formation in thin films of colloidal polystyrene particles", Langmuir **27**, 8009–8017 (2011).

[83]G. Berteloot, A. Hoang, A. Daerr, H. P. Kavehpour, F. Lequeux, and L. Limat, "Evaporation of a sessile droplet: inside the coffee stain", Journal of Colloid and Interface Science **370**, 155–161 (2012).

[84]J. Schroers and W. L. Johnson, "Ductile bulk metallic glass", Physical Review Letters **93** (2004) `10.1103/physrevlett.93.255506`.

[85]A. Nakahara and Y. Matsuo, "Imprinting memory into paste to control crack formation in drying process", Journal of Statistical Mechanics: Theory and Experiment **2006**, P07016–P07016 (2006).

Curriculum vitae

Pree-cha Kiatkirakajorn

Yala, Thailand

Nationality: Thai

Education

2014-present	Reseach fellow, **Max Planck Institute for Dynamics and Self-Organization**, Göttingen, Germany
2010-2013	**Georg-August-Universität Göttingen**, Göttingen, Germany M.Sc. Physics Dissertation Title: shear banding in colloidal dispersions
2004-2007	**Prince of Songklah university**, Songkhla, Thailand BSc. Physics Dissertation Title: Physical structure of a contact binary star system YY Eridani

Publication

Drying paint: from micro-scale dynamics to mechanical instabilities, L. Goehring, J. Li and P. Kiatkirakajorn, Phil.Trans.R.Soc.A375: 20160161 - Published 4 April 2017

Formation of shear-bands in drying colloidal dispersions, P. Kiatkirakajorn and L. Goehring, Phys. Rev. Lett. 115, 088302 - Published 21 August 2015